Imaging and counting of targets with a high resolution multibeam sonar

Kushwant Mussai

A dissertation submitted to the Department of Electrical Engineering,
University of Cape Town, in fulfilment of the requirements
for the degree of Master of Science in Engineering.

Cape Town, February 2010

Acknowledgements

The past three years of my life have been oriented towards working on this project. I would like to thank the persons who have helped and contributed in completing it. Foremost, I would like to thank Associate Professor Andrew Wilkinson for his guidance in the technical aspects of the project and moral and financial support.

I was also financially supported by the following institutions: UCT's University Research Committee, The South African Squid Management Industry Association (SASMIA), Marine and Coastal Management (MCM) and South African National Research Foundation (NRF).

I would also like to mention Dr Marek Lipinski of Marine and Coastal Management, and Mike Soule and Ian Hampton of Fisheries Resource Surveys for having initiated the project, providing technical advice and help along its development. Further, the MCM, who owns the ABACUS hardware, is to be thanked for providing logistics for pelagic surveys.

Thanks to Dr Yoann Paichard for the advice, suggestions and encouragement. I would also like to thank Peter McMahon for the advice, help and support to keep me going. I also extend my gratitude to my colleagues in the Sig Lab, Andrew and Rachel, and friends, Graham and Kayshinee who have helped in one way or another to get this project to completion.

Thanks mum.

Abstract

This dissertation pertains to the development of an imaging and counting system for a high resolution multibeam sonar. A mathematical model for the operation of the multibeam sonar is derived. The computational model is developed into a simulator for the multibeam sonar in MATLAB. It is noted that the simulator is capable of producing synthetic data for various scenarios. The signal processing needed to extract information from the data is then studied and implemented. Pulse compression and beamforming are applied to the data to form (2D) sonar images of the azimuth-range plane of the submarine environment. A threshold is determined to discriminate between peaks that arise as a result of targets and those that arise as a result of relatively bright secondary maxima and noise. The threshold is derived by means of statistical hypothesis testing in the resolution cells of the image. A false alarm probability not to be exceeded is set and a threshold is calculated based on the noise statistics in the sonar images. A peak detection algorithm is then used to estimate the number of peaks -that arise as a result of targets- in the sonar images. Phase interferometry -subtraction of complex sonar images formed from two receiver subarrays- is then performed to determine the angle of arrival of the targets in elevation. Further, the parameters estimated and the geometry of the ABACUS system are used to solve a system of equations to determine the location of the targets in the 3D coordinate system. We then evaluated the simulator, imaging and counting system with respect to the variables such as noise, sonar target strength and target position in the submarine environment. It is concluded that the ABACUS is capable of high resolution imaging of targets. Moreover, we also conclude that the system performed reasonably well in the high resolution counting of targets at moderate to high densities. Lastly, preliminary processing of real data showed that the simulator and counting system developed can potentially be used to obtain estimates of counts of fish from pelagic surveys.

Contents

List of Figures

List of Tables

Chapter 1

General Introduction

1.1 Sonar Summary

SONAR (Sound Navigation and Ranging) is a means to detect targets and estimate parameters of these targets such as range and bearing [18, 4]. The active sonar operates by transmitting a wave of known shape and then intercepting echo signals from the targets and obstacles in the scene. The transmitted wave can be a pure tone signal or have its frequency, phase or amplitude modulated.

A simple model of the operation is now described. The received echo signal is modified by propagation and reflection from the targets and obstacles (assumed to be point scatterers) in the scene. Further, the echo signals are contaminated by noise (often modeled as white Gaussian noise in the frequency band used), which include thermal noise from the receiver and ambient noise from the medium. Therefore, if the target is stationary, the intercepted echo signal is a noisy replica of the transmitted signal, shifted in time, with a delay corresponding to the two-way sonar path and modified by a complex coefficient due to attenuation from the propagation and reflection from the target, and from the corresponding phase shift. In the case of a target moving at constant velocity, the signal would also be frequency shifted.

As mentioned earlier, the aim is to detect targets and/or to estimate their parameters. Hence, the echo signal which is impaired needs to be processed to extract useful information about the scene or form images of the scene. The processing of the signals is an inverse problem to estimate parameters of the scene.

1.2 Multibeam sonars

Multibeam sonars are instruments that can map several locations of the submarine environment with one ping. They are extensively used in ocean mapping for bathymetry, hydrographic, and sub-bottom applications.

1.2.1 Operation of multibeam sonars

A multibeam sonar generally consists of a transmitter and receiver array arranged perpendicular to each other [2]. The transmitter sends an acoustic pulse in -all directions perpendicular to the axis of the array- the submarine environment. As the sound waves from the array propagate and spread, the amplitude of pressure field produced, varies as a function of angle. A simplified geometry of the beam pattern (amplitude variation as a function of space) generated by the transmitter array is depicted in Figure 1.1. It is noted that the beam can be steered to insonify other regions of the underwater environment. Echo signals reflected from the targets in the insonified volume, or from the sea floor are recorded by each element of the receiver array. The data at the array are then combined -summed in phase- in software (or in hardware[1]) to form a narrow beam (beamforming) pointing in a specific direction (as shown in Figure 1.1), such that sound is received preferentially in that direction. Further, the beam can be steered to scan several directions and thus, receive echos from several locations. In this way, the multibeam sonar is capable of resolving the angle of arrivals from several directions simultaneously, in one ping.

[1] radar systems

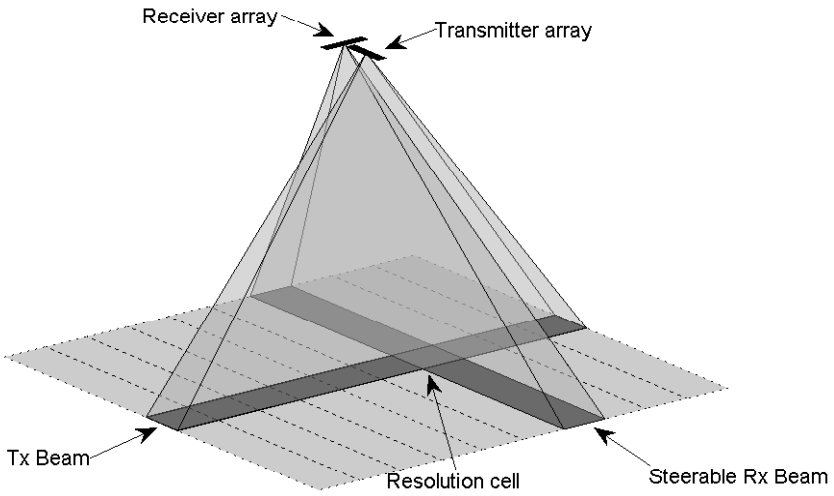

Figure 1.1: Multibeam sonar operation

1.2.2 Mills Cross Technique

It is to be noted that the transmitter and receiver arrays are arranged perpendicular to each other, in an L or T configuration. If the transmitter and receiver arrays were arranged parallel to each other, the transmitter array would ensonify a volume of the ocean and the receiver array would receive echo signals from the same volume, therefore, there would be no way of telling where, in that volume, the echo signals were coming from.

When the transmitter and receiver arrays are arranged perpendicular to each other, the volume ensonified by the transmitter intersects the volume observed by the receiver array. The dimensions of the intersection volume are defined by the beamwidths of the transmitter beam (in elevation) and receiver beam (in azimuth). Hence, even though echo signals can occur from anywhere in the volume insonified by the transmitter and signals received from anywhere in the volume observed by receiver, the signals recorded at the receiver will only be echos of the transmitted signal from the intersection volume (or resolution cell) as depicted in Figure 1.1. This arrangement of the receiver and transmitter is called the *Mills Cross* [2].

The multibeam sonar is generally mounted on the hull of a ship, so that contiguous volumes (as the one indicated in Figure 1.1) can be mapped as the ship moves along its

path. In this way, large areas of the sea can be mapped for various applications.

1.2.3 Visualisation of multibeam sonar data

In this section, the imaging capabilities of a stationary multibeam sonar are briefly discussed. In multibeam sonar systems, the receiver can be linear, planar, or annular. In general, a linear receiver array produces a 2-D image (range and one angle) depicting a plane of the landscape. Planar arrays are capable of resolving the two orthogonal angles of arrival of echo signals, thus producing 3-D volumetric images. It is noted that we have assumed a single element transmitter.

It is mentioned that one can also produce a 3-D image with a linear transmitter array and linear receiver array, by steering the transmitter beam in multiple pings to scan several directions. Other antenna configurations to produce 3-D volumetric images of the underwater environment are discussed in [39].

1.3 Applications of Multibeam Sonars as fisheries tools

As mentioned previously, multibeam sonars are extensively used in ocean mapping for several applications. Multibeam sonars have recently been recognised as a tool for fisheries applications as well. Multibeam sonars offer several comparative advantages over the other survey equipments such as conventional echo sounders. Indeed, the multibeam sonars are capable of covering larger volumes of the ocean in relatively shorter times, and offer higher resolution (imaging) of the submarine environment. Those capabilities make multibeam sonars the equipment of choice to -survey widely dispersed and fast moving schools of fish- to obtain biomass and density estimates for stock assessment and to study fish behaviour and their distribution.

The research done on the application of multibeam sonars as a fisheries tool is briefly reviewed. The department of Zoology, at the University of New Hampshire has worked on the development of a multibeam sonar as a fisheries tool to study the behaviour and estimate the abundance of fish. The high resolution multibeam sonar (EM 3002), operating at 300 kHz is used in conjunction with two split-beam[2] echosounders (EK 60) operating at 38 and 120 kHz. Fish were placed in a confined and controlled environment.

[2]A split beam sonar has its receiving transducer divided into four quadrants. The signal received from a single target is measured separately at each quadrant. The phase differences between two pairs of quadrants are used to determine the two orthogonal angles of arrival of the target. The sonar target strength of the target is subsequently determined by compensating for the beam pattern in the angular directions of arrival. Note that it is assumed that the sonar has been calibrated.

Estimates for the number of fish targets and density are to be derived from the sonar target strengths and the echo signal amplitudes by several methods. For the split-beam sonars, echo counting and echo integration are to be used. For the multibeam sonar, the echo signals are first to be compensated for the beam patterns. The experiments were ground truthed by underwater cameras. It is mentioned that the sonars were calibrated with metallic spheres. The report indicated that the detection of fish targets is possible using the multibeam sonar. The sonar data can be used to derive reliable estimates of the number of fish, once the sonar target strength is derived [14].

Further Gerlotto et al., in their study, demonstrate the multibeam sonar (RESON SEABAT 6012) as an advanced tool, which is capable of identifying and counting individual fish targets. The paper also points out the capabilities and advantages -over the other survey methods used- of the multibeam sonar to obtain quantitative estimates of fish: coverage of large volumes; capability of spatial description of fish targets (high resolution); and the fact that multibeam sonars don't influence fish behaviour as much as the classical methods such as trawl surveys and the use of single beam echo sounders in which case the movement and engines of ship scare the fish away [12].

It was also shown by Misund et al. that a multibeam sonar operating at 95 kHz (SIMRAD SA950) validates the abundance estimates of fish, while enabling better mapping of the targets, obtained from conventional echo-integration methods [25].

This was further enforced by Melvin et al who compared data from a high frequency (200 kHz) multibeam sonar (SM 2000) sonar to that of a conventional echo sounder. It was concluded that the multibeam sonar can replace a single-beam or split beam sonar for acoustic surveys of fish [13].

The literature review indicates the multibeam sonar is a well suited equipment for fisheries surveys as it enhances the capacity to visualise and quantify fish targets.

1.4 Objectives of project

The estimation of sonar target strength is only effective at low target densities using conventional split-beam sonars, those instruments are limited as they have low resolution at frequencies (20-100 kHz) for which estimates are needed. The proposed solution (by Mike Soule and Ian Hampton) to that limitation is to use a high frequency multibeam sonar to obtain fish counts/ density estimates at high densities. The density estimated is then to be used in conjunction with data output from an echo integrator/split-beam sonar, gated at the same depth as the multibeam sonar, to derive the sonar target strength of squid targets indirectly [34].

1.5 The ABACUS System

The multibeam sonar (ABACUS -Advanced Beamformer for Acoustic Counting of Underwater Scatterers) was developed by the Marine and Coastal Management (MCM), Cape Town, South Africa in the early 1990's. The aim was to obtain high resolution images of fish targets for biomass estimation and specifies identification. The project was then brought to Associate Professor Andrew Wilkinson at the University of Cape Town. The latter supervised two projects which aimed to develop the ABACUS into a counting system. In the first project, by Ferdinand Ng, the ABACUS hardware was revived and a data capture system for the sonar was developed [22]. The second project, by Etienne Eccles, pertained to some aspects of signal processing as he demonstrated the use of superresolution algorithms to obtain high resolution sonar images from ABACUS-like data [10].

1.6 Scope of project

This dissertation pertains to the high resolution imaging and counting of targets (squids). The thesis involves the development of a mathematical model of the sonar system and the submarine environment so that we are able to simulate scenarios that would be otherwise be impossible to capture in real life, and to make up for the absence of the ground truthing of data. Further, surveys -ship and manpower- are expensive. Simplifying assumptions, for environmental data unavailable and the modeling of some aspects of the system (analytic target strength model)[3] is outside the scope of this thesis. A simulator, based on the model developed, has been created in the MATLAB package to test and benchmark the signal processing steps that are applied. The aim is to estimate the squid density in dense aggregations, with the existing limitations.

1.7 Structure of thesis

This dissertation is structured in the following way:

In Chapter 2, mathematical models for the ABACUS sonar, sound propagation and the underwater environment are derived.

Chapter 3 details the operation and parameters of the ABACUS simulator.

[3] A simplistic stochastic model in incorporated in the simulator

Chapter 4 pertains to the processing of the echo signals to resolve the spatial -angular and range- locations of the possible targets to form and display images of the azimuth-range plane of the landscape (2-D complex images).

In Chapter 5, the detection theory needed to determine a threshold to discriminate between targets and noise is studied, and a peak detecting algorithm to count the number of targets in the images is implemented.

In Chapter 6, phase interferometry methods are applied to resolve the angular location of detected targets in elevation, thereby determining the 3-D location of targets. The targets outside a defined counting volume are to be subsequently subtracted from the target count estimates.

In Chapter 7, the performance of the detection and counting system using synthetic data generated from the simulator are assessed. Real sonar data obtained from pelagic surveys are then processed to obtain the required statistics of squid count and density. The model is further extended to derive sonar target strengths for squids.

In Chapter 8, some work that can be done in the future if the project is to be ameliorated is proposed.

Chapter 2

Mathematical Modeling of Multibeam Sonar System

This chapter pertains to the development of a mathematical model that simulates the working of a multibeam sonar system, in particular the ABACUS. The model includes the sonar transmitter and receiver, the acoustics (sound transmission and propagation), and the environment. We want to be able to simulate various scenarios and create synthetic sonar data that are to be used to develop and evaluate signal processing techniques. Evidently, the aim is to derive and validate the appropriate signal processing needed to process data obtained from a pelagic survey to achieve an optimum counting system. It is to be noted that the model is developed with several simplifying assumptions. The modeling of a comprehensive and complete model is beyond the scope of this project.

2.1 Multibeam Sonar Model

The general operation of a multibeam sonar has been detailed in sections 1.2.1 and 1.2.2. The multibeam sonar model treated in this thesis is based on the ABACUS. The ABACUS operates mounted on the hull of a stationary ship. The ABACUS transmitter is made up of 16 elements ganged together, acting like a single element transmitter. The receiver has two subarrays, each of which consists of 16 elements. It is mentioned that the elements of the transmitter and receiver are not arranged in linear fashion, but are staggered. The effects of that arrangement are studied during the course of this thesis. The simplified geometry of the volume ensonified and the beam steering operation are depicted in Figure 2.1.

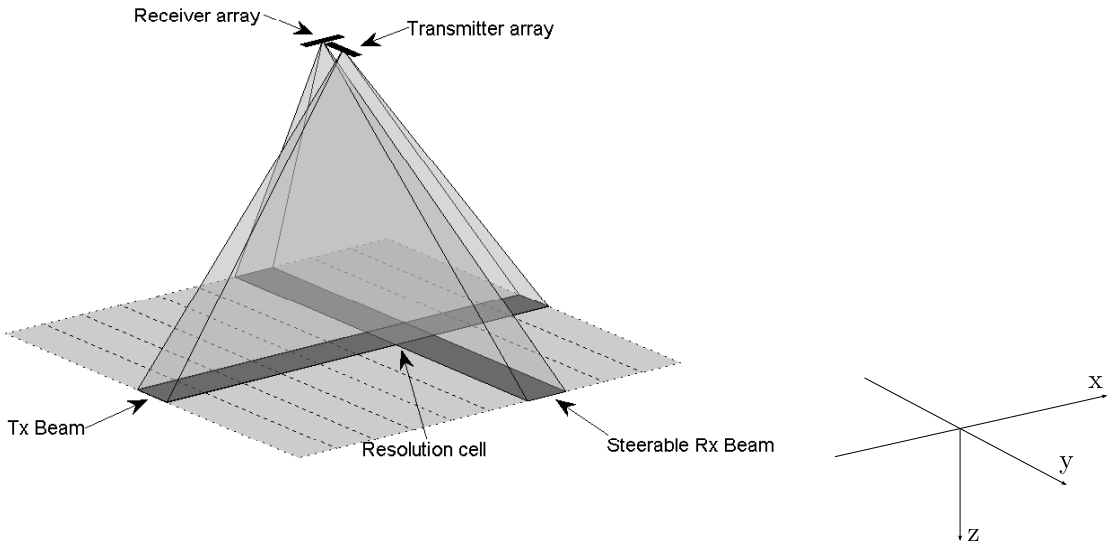

(a) Resolution cells formed by the intersection of orthogonal transmit and receive beams (b) axis

Figure 2.1: Multibeam sonar operation

2.1.1 Geometry of the system

The scene is associated to a fixed reference (O,x,y,z) of a three dimensional coordinate system. The transmitter and emitter arrays are also referred to the origin O, as indicated in Figure 2.2.

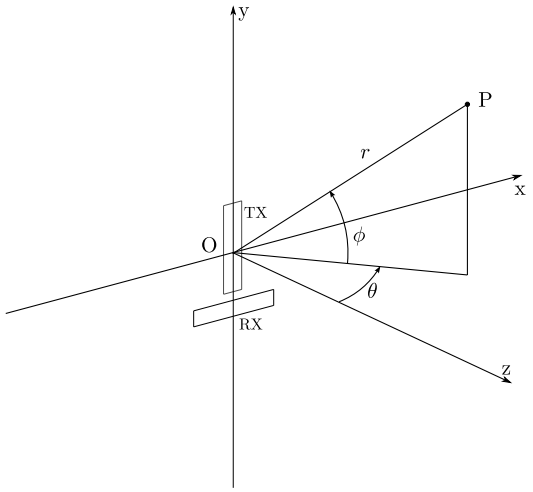

Figure 2.2: Coordinate system associated to the scene

The symbols used are thus defined:

P : arbitrary point target scatterer

r : radial distance from the reference point (origin)

θ: horizontal or azimuth angle: θ is measured anticlockwise from the z axis

ϕ : vertical or elevation angle: ϕ is measured upwards from the x-z plane

The positive z direction is defined as the look direction (boresight)

2.2 Sound Propagation model

We now develop a model to compute the acoustic pressure field distribution generated from a linear array [32, 42, 43]. We aim to study the beam directivity of the array. The beam directivity functions is generally a measure of the direction of beam propagation. In particular, we investigate the effects on the beam directivity -how the main lobes to side lobes ratio are affected- by the staggering and offset in the positions of the elements of the ABACUS's transmitter and receiver arrays. It has been postulated that the ABACUS's receiver and transmitter design improves the directivity patterns as the side lobes are suppressed.

The model developed is based on Huygen's principle, which states that each point on an advancing wave can be considered as a source of secondary waves, which spread spherically in an isotropic medium [32]. Hence, the pressure field at a point P can be modeled as the

superposition of the pressure field from several sources, with properly selected phase and amplitude to represent the physical situation of the system.

The model starts by deriving the pressure field at a point generated by the single element of an array. A brief mathematical development is treated in the following sections.

2.2.1 Point source

A quantitative measure of the acoustic pressure from a point source (spherical) is obtained as a solution of the wave equation, which can be expressed as [32]:

$$\frac{1}{r^2}\frac{\partial}{\partial r}\left[r^2\frac{\partial}{\partial r}p(r,t)\right] = \frac{1}{c^2}\frac{\partial^2}{\partial t^2}p(r,t) \tag{2.1}$$

with r defining the radial distance from the source, p is the acoustic pressure at the point P, c is the speed of sound in water[1]. The geometry is shown in Figure 2.3.

The solution to the wave equation gives the pressure at the point P as:

$$p(r,t) = P_0\frac{r_0}{r}exp\left[j\left(\omega t - kr\right)\right] \tag{2.2}$$

where ω is the angular frequency, k is the wave number[2], P_0 is the rms pressure at the reference distance r_0 (given as 1m).

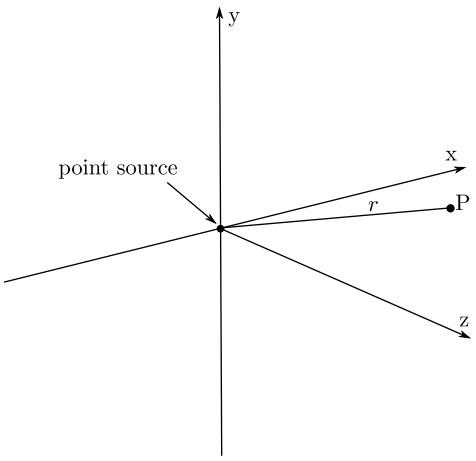

Figure 2.3: Geometry to show acoustic pressure at a point P due to point source

[1] We note that Equation 2.1 assumes constant c and spherical spreading

[2] ωt is the angular phase and kr is the spatial phase

2.2.2 Single rectangular element

Now, to derive the pressure field at a point due to a single rectangular element, we start by determining the pressure field generated by a line of (spherical) point sources. The geometry displayed in Figure 2.4 shows N point sources covering a width w along the x axis.

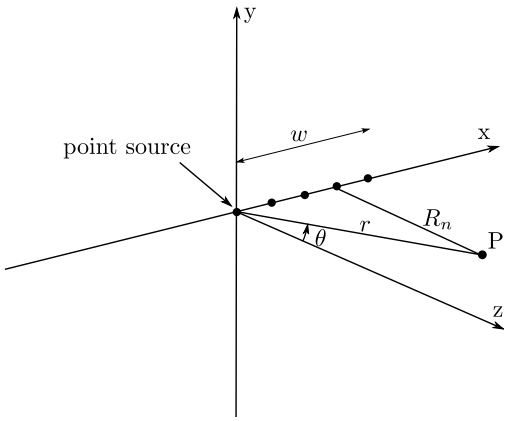

Figure 2.4: Geometry to show the pressure field at point P due to a line of point sources.

Referring to section 2.2.1 and the geometry in Figure 2.4, the pressure generated by the nth point source is given by:

$$p_n = P_{0_n} \frac{r_0}{R_n} exp\left[j\left(\omega t - kR_n\right)\right] \tag{2.3}$$

From the geometry in Figure 2.4, the x-axis position of the nth point source is:

$$x_n = \frac{nw}{N-1} \tag{2.4}$$

Hence the range R_n can be approximated[3] to be:

$$R_n \simeq r - \frac{nw(sin\theta)}{N-1} \tag{2.5}$$

where θ is the horizontal angle.

[3]The approximation mathematically implies that we are considering plane waves, as the higher power terms in the binomial expansion to compute R_n are dropped. In literature, this approximation is also referred to as the Fraunhofer or far field approximation.

Therefore, the superposition of the pressure from the N point sources at point P gives:

$$\begin{aligned} p &= \sum p_n \\ &= \frac{P_{0_n} r_0}{r} exp\left[j\left(\omega t - kr\right)\right] \sum_{n=0}^{N-1} exp\left[\frac{jknwsin\theta}{N-1}\right] \end{aligned} \tag{2.6}$$

where $1/R_n \backsimeq 1/r$ is factored out of the summation.

Evaluation of the above summation and simplification gives the pressure at point P due to a line of point sources as:

$$p = \frac{sin(k\frac{w}{2}sin\theta)}{k\frac{w}{2}sin\theta} \frac{P_0 r_0}{r} exp\left[j\left(\omega t - kr\right)\right] \tag{2.7}$$

where $P_0 = NP_{0_n}$ is the rms pressure of the line source at r_0.

Now for a rectangular element, shown in Figure 2.5 in which all the point sources are in phase and have the same amplitude, the pressure field at point P can be extended to:

$$p = \frac{sin(k\frac{w}{2}sin\theta)}{k\frac{w}{2}sin\theta} \frac{sin(k\frac{l}{2}sin\phi)}{k\frac{l}{2}sin\phi} \frac{P_0 r_0}{r} exp\left[j\left(\omega t - kr\right)\right] \tag{2.8}$$

where l and w are the length and width of the rectangular element.

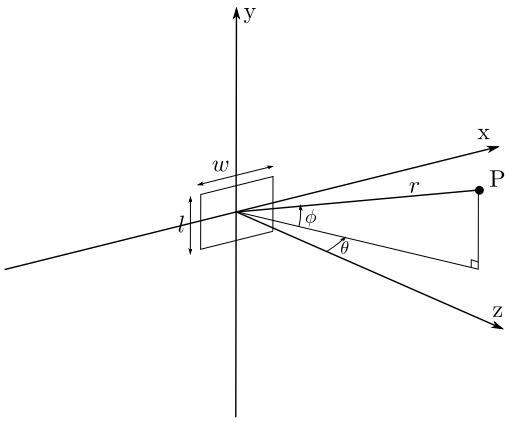

Figure 2.5: Geometry to show the pressure field due to a single rectangular element

The above generalisation can be justified mathematically, since the treatment is the same for the pressure contribution for point sources along the y axis as for the x axis, and the two angles θ and ϕ are orthogonal.

2.2.3 Linear Phased Arrays

We now compute the acoustic pressure field at a point, from an array of rectangular elements by using a similar approach that was used to derive the pressure field from one rectangular element. Therefore, using Huygen's principle to sum the contribution of the pressure field from each element and referring the geometry depicted in Figure 2.6, the pressure as a function of horizontal and vertical angles can be expressed as[4]:

$$p(r,\theta,\phi) = \sum_{n=1}^{N} \frac{sin(k\frac{w}{2}sin\theta_n')}{k\frac{w}{2}sin\theta_n'} \frac{sin(k\frac{l}{2}sin\phi_n')}{k\frac{l}{2}sin\phi_n'} \frac{p_{0_n}r_0}{r} exp\left[j\left(\omega t - kR_n\right)\right] \tag{2.9}$$

The time dependence is common for all the sources, hence, the temporal phase ωt can be dropped from the above equation, which simplifies to:

$$p(r,\theta,\phi) = \sum_{n=1}^{N} \frac{sin(k\frac{w}{2}sin\theta_n')}{k\frac{w}{2}sin\theta_n'} \frac{sin(k\frac{l}{2}sin\phi_n')}{k\frac{l}{2}sin\phi_n'} \frac{p_{0_n}r_0}{r} exp\left[j\left(-kR_n\right)\right] \tag{2.10}$$

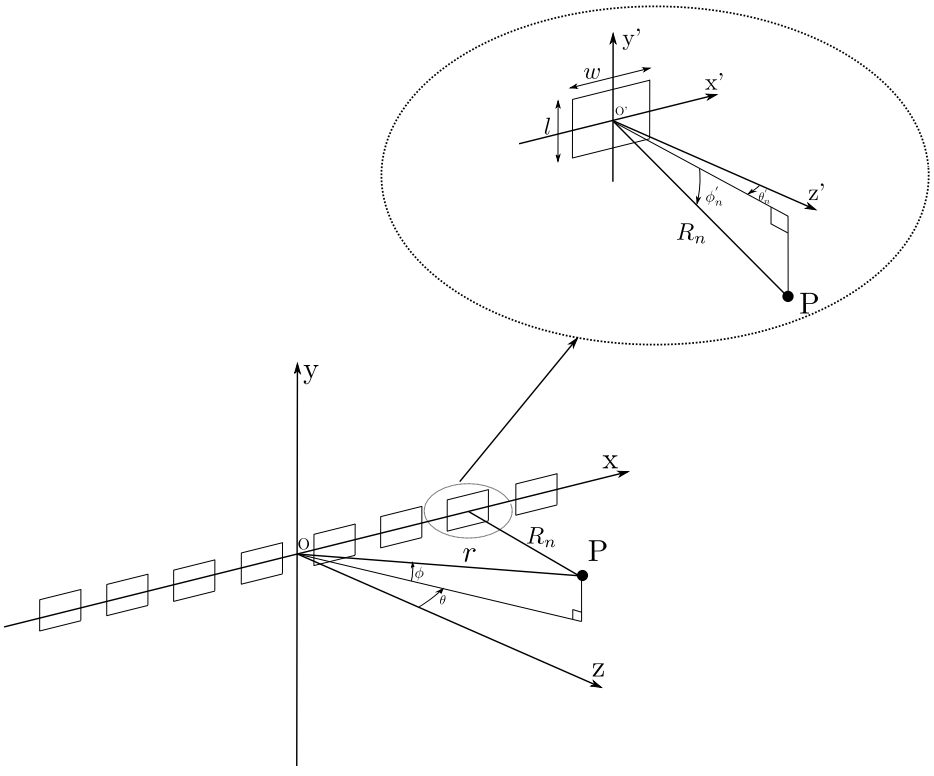

Figure 2.6: Geometry to show the pressure field due to an array of rectangular elements

Figure 2.6 shows the schematic to compute the acoustic pressure field at point $P(r,\theta,\phi)$

[4]The expression is not further simplified, since the staggering and offset in the ABACUS's transducer configuration makes the maths rather complicated.

from a linear array. θ and ϕ are the horizontal and vertical angles with respect to the origin O of the global coordinate system. r denotes the radial distance of the point P from the origin. Further, $\theta_n^{'}$ and $\phi_n^{'}$ denote the horizontal and vertical angles with respect to O', the origin of the local coordinate system of an element.

This simple result is used to simulate the beam patterns of the transmitter and receiver arrays.

2.2.4 Directivity function (Beam Pattern)

The directivity function is defined as the as the normalised pressure amplitude as a function of the horizontal and vertical angles. The directivity function provides an indication of the beam propagation characteristics of the ABACUS system. The simple result derived in section 2.2.3 is used to simulate the beam patterns of the transmitter and receiver arrays of the ABACUS. We also study the beam pattern to understand the relative merits of the ABACUS's transducer arrangement. The directivity function is given by[5] [43]:

$$E(\theta,\phi) = \left| \sum_{n=1}^{N} \frac{sin(k\frac{w}{2}sin\theta_n^{'})}{k\frac{w}{2}sin\theta_n^{'}} \frac{sin(k\frac{l}{2}sin\phi_n^{'})}{k\frac{l}{2}sin\phi_n^{'}} exp\left[j\left(-kR_n\right)\right] \right| \tag{2.11}$$

2.3 Sound Attenuation in Water

Attenuation loss in water consists of absorption and geometrical spreading losses.

2.3.1 Absorption loss

The absorption loss is a consequence of the fact that sound energy is converted to heat as the sound waves propagate. The absorption loss is a function of frequency and obeys the law in Figure 2.7. It is measured in decibels per metres. Therefore the loss in dB is given as αr where α is the absorption coefficient and r is the distance. From the loss in dB, we deduce that the sound pressure decreases exponentially at a rate of [18, 37, 32]:

$$\begin{aligned} dB\,loss &= -20\,log_{10}\frac{p}{p_i} \\ p &= p_i\,10^{(-\frac{\alpha r}{20})} \end{aligned}$$

where p_i is the rms pressure at $r_i = 0\,\mathrm{m}$.

[5] $/\max(\mathrm{E}(\theta,\phi))$

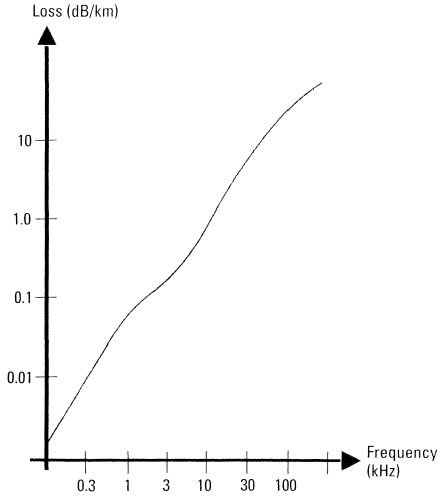

Figure 2.7: Losses by absorption in the ocean[18]

2.3.2 Geometrical spreading (divergence loss)

The signal is also attenuated due to divergence losses. The wave equation solution defined by Equation 2.2 indicates that the pressure field is inversely proportional to r.

2.3.3 Assumptions and Simplifications

In the development of our mathematical model, we have assumed spherical spreading, which further implies that we have assumed an isotropic homogeneous medium. We note that wave equation can only be solved if the sound speed is assumed to be constant [18, 32]

However, it is to be noted that in real situations in submarine acoustics, the speed of sound varies as a function of depth. The sea is a multilayered medium with a variable refractive index. The sound ray path technique is generally used to calculate accurately the divergence loss [18]. The typical profiles of temperature and velocity are shown in Figure 2.8.

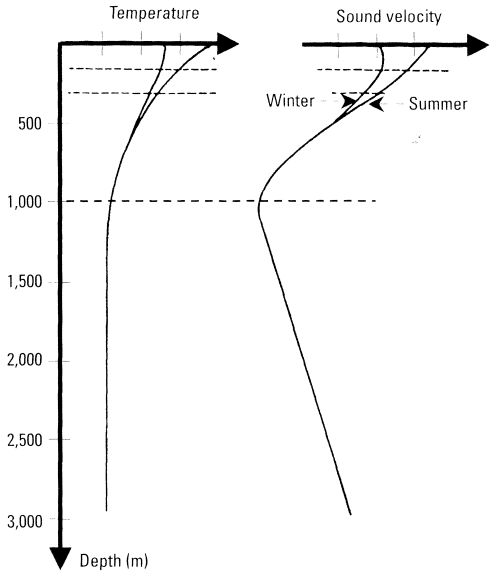

Figure 2.8: Typical sea water temperature and sound speed profiles [18]

2.4 Underwater Environment model

2.4.1 Sonar target strength model

The received signal is a modification of the transmitted wave, as the latter is reflected from targets in the scene. This implies that the nature of the received signal is determined by the interaction between the transmitted signal and the targets. This in turn suggests that the properties of the received signal depend on the physical characteristics (shape, material, size) of the target. Therefore, we generally need a physical model for the wave-target interaction to derive a (received) signal model. In sonar systems, this model is often extremely complex.

The backscattering coefficient is generally termed as the sonar target strength (TS) in sonar systems. It is the equivalent of the Radar Cross Section (RCS) in radar systems. The sonar target strength is defined as ratio of the sound intensity reflected from the target, in the direction of the receiver, measured at 1m from the target, to the sound intensity incident on the target. In mathematical terms, the sonar target strength is given as [18]:

$$\sigma = \frac{I_{r,1m}}{I_i} = \frac{P_{r,1m}^2}{P_i^2} \tag{2.12}$$

where I_i and I_r denote the incident and reflected sound intensities respectively. P_i and P_r denote the incident and reflected pressure amplitudes.

The backscattering coefficient is defined in terms of pressure:

$$\rho = \sqrt{\sigma} = \frac{P_{r,1m}}{P_i} \tag{2.13}$$

There are several analytical methods to model the wave-target interaction, and subsequently, the sonar target strength, discussed in literature. These models are based on geometrical and physical acoustics and ray theory. The development of those models are rather complex and outside the scope of this project. However, there are also some simpler, albeit less accurate, empirical modeling methods in literature. The models are namely: the multiple-scatterers model and the stochastic model. The development of those models are detailed in [18].

In this project, we use a stochastic model for the sonar target strength. The backscattering coefficient of the targets is modeled by a Rayleigh stochastic process. This is justified as we assume a target to have a large number of point like scatterers each characterised by an amplitude and phase as backscattering coefficient. Hence, the central limit theorem suggests that the backscattering coefficient is a Gaussian random process. Further, the ABACUS system being coherent, implies that the resultant of the normal random processes on the quadrature and in-phase channels produces a Rayleigh process at the output. The model is further endorsed by [8]. Moreover, we refine the model as we set lower and upper bounds to the backscattering coefficient. The setting of the lower bound factors in the fact that it is very unlikely for the pressure backscattered from a target[6] to be zero. A upper bound on the stochastic process excludes the possibility of an unrealistically high backscattering coefficient.

Literature also suggests that extensive research has been carried out to model the backscattering coefficient of squid targets. The studies have shown that sonar target strength depends on various physical properties of squids: body length and shape; ensonifying frequency; structural components of the body and their physical parameters (density and sound speed); orientation and behaviour; swimming movement [3]. The analytic models developed by [Arnaya et al.] are situation specific and extending the model to determine accurate values for the sonar target strength of squids for the ABACUS system would be very complex.

Hence, we use the aforementioned stochastic model to derive our signal model.

[6]The targets being referred to, are assumed to be squids.

2.4.2 Noise

Noise can be defined as unwanted signals. It is a major limiting factor in sonar systems as it hampers the detection of targets, or the estimation of their parameters. Noise present at the receiver has different origins. Indeed, noise from the submarine environment is caused by the wind, waves, turbulence, and animals communicating. Further, there are artificial noise sources such as fishing vessels, seismic surveys, and military sonars. There has been several comprehensive studies on noise in the submarine environment. The graph in Figure 2.9 from Wenz, indicates that at around 400 kHz (the operating frequency of the ABACUS), the ambient sea noise is predominantly due to thermal noise (due to motion of water molecules), and less of sea state, ship and turbulent noise [9]. Yet, it is to be pointed out that there can be various spurious signals such as reverberation (reflection of sound signals from other objects) or other sonars operating at around the same frequency of the ABACUS. Reverberation modeling is a complex process, and is outside the scope of this project. In addition to noise from the submarine environment, thermal noise of the receiver (generally caused by the mixer and the first amplifier) is also present. It is assumed[7] that the ambient sea noise and the thermal noise of the receivers can be modeled as white and additive Gaussian (zero mean) noise in the frequency band, uncorrelated to the signal being considered. It is noted that the spurious signals and reverberation can also be treated as noise, albeit, colored noise. We therefore model the complex white noise noise, limited to the bandwidth of the receivers [$-F_{max}, +F_{max}$] as [18]:

$$n(t) = b(t)e^{j\omega_0 t} \tag{2.14}$$

where the auto-correlation function is defined as:

$$B(t) = N_0 \; sinc(2F_{max}t)$$

$$\begin{cases} sinc(t) = \frac{sin(\pi t)}{\pi t} \\ N_0 = E\left\{ \mid b\left(t\right) \mid^2 \right\} \end{cases} \tag{2.15}$$

where N_0 is the power spectral density of the noise.

[7] A loose justification for this assumptions is the Central Limit Theorem which states the the sum of the pdfs of a very very large number of noise sources will add up to a Gaussian pdf.

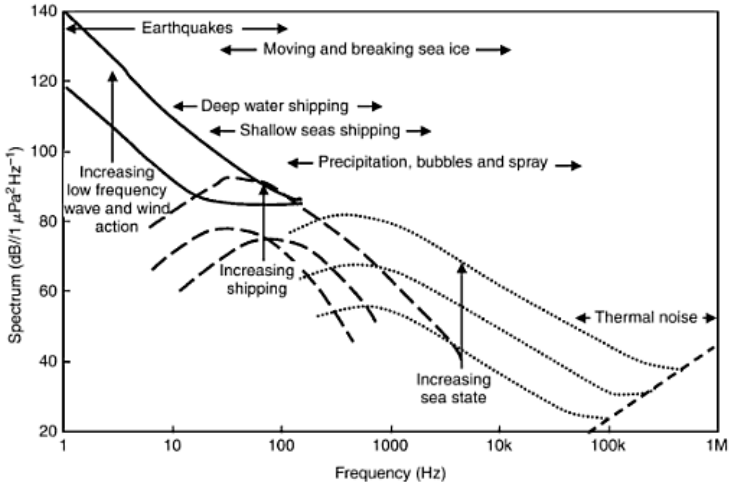

Figure 2.9: General characteristics of ambient noise in the sea. The separated curves represent the variation of ambient noise according to weather conditions and the level of shipping activity. [9]

2.5 Signal Model

We now derive a model for the received signal using the models of the components of the sonar system that we have developed thus far.

2.5.1 Linear model

We start by deriving a linear signal model for the transmitted wave and echo signal intercepted in a noisy medium. Let us assume a point target scatterer and refer to the geometry of an elementary sonar system depicted in the diagram in Figure 2.10.

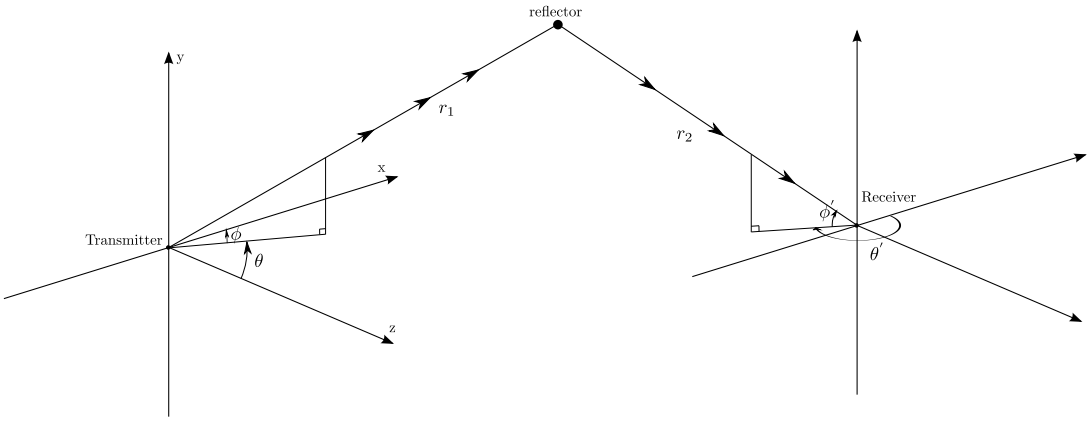

Figure 2.10: Elementary sonar geometry

The echo signal intercepted is given by:

$$r(t) = E_t(\theta,\phi)\frac{1}{r_1}10^{-\frac{\alpha r_1}{20}}\rho(r,\theta,\phi)E_r(\theta^{'},\phi^{'})\frac{1}{r_2}10^{-\frac{\alpha r_2}{20}}s(t-\tau)+n(t) \tag{2.16}$$

where

$E_t(\theta,\phi)$ and $E_r(\theta^{'},\phi^{'})$ are the directivity functions of the transmitter and receiver respectively. The angular coordinates of the receiver are denoted by primes.

τ is the two-way time delay.

$\frac{1}{r}$ and $10^{-\frac{\alpha r_1}{20}}$ are the divergence and absorptions losses.

$\rho(r,\theta,\phi)$ is the backscattering coefficient of the point target scatterer in terms of pressure, as explained in Section 2.4.1.

$n(t)$ is the noise at the receiver.

Note that the echo signal intercepted is spatially distributed across the receiver array. The signal received at an element is therefore given as an modification of 2.16 and is given as:

$$r(t,n) = E_t(\theta,\phi)\frac{1}{r_1}10^{-\frac{\alpha r_1}{20}}\rho(r,\theta,\phi)E_{r_n}(\theta^{'},\phi^{'})\frac{1}{r_{2n}}10^{-\frac{\alpha r_{2n}}{20}}s(t-\tau_n)+n_n(t) \tag{2.17}$$

where n is the nth element of the receiver.

We now extend the signal model for distributed targets to:

$$r(t,n) = \int\int\int(E_t(\theta,\phi)\frac{1}{r_1}10^{-\frac{\alpha r_1}{20}}\rho(r,\theta,\phi)E_{r_n}(\theta^{'},\phi^{'})\frac{1}{r_{2_n}}10^{-\frac{\alpha r_{2_n}}{20}}s(t-\tau_n))drd\theta d\phi+n_n(t) \tag{2.18}$$

For the purposes of digital processing, we assume that the landscape is discrete and we associate a response to each point in the landscape. Equation 2.18 is further modified to:

$$r(t,n) = \sum_r\sum_\theta\sum_\phi(E_t(\theta,\phi)\frac{1}{r_1}10^{-\frac{\alpha r_1}{20}}\rho(r,\theta,\phi)E_{r_n}(\theta^{'},\phi^{'})\frac{1}{r_{2n}}10^{-\frac{\alpha r_{2n}}{20}}s(t-\tau_n))+n_n(t) \tag{2.19}$$

From 2.19, it can be implicitly assumed that the system is linear time invariant, as it is suggested that the echo signal modeled for an extended target is the superposition of the individual discrete points that make up the target.

2.5.2 (Complex) Analytic model

We now look into the complex (analytic) model, widely cited in sonar signal processing literature [33], for it facilitates mathematical manipulations. An analytic signal is one

which has no negative frequency components. Any real signal $x(t)$ can be converted to an analytic signal, by constructing a Hilbert filter $H_t(x)$, which shifts all the sinusoids in the real signal by $\pi/2$. In fact, the positive frequency components are shifted by $-\pi/2$ and the negative components by $\pi/2$. The analytic signal of the form $z(t) = x(t) + jH_t(x)$ is formed as the negative frequency components in $x(t)$ and $jH_t(x)$ cancel out.

Let the signal transmitted be a narrowband signal (In loose terms, a signal with all energy centred about a single carrier frequency). The concept will be discussed in more depth later in this dissertation.

The analytic model of the sent signal is then:

$$s(t) = u(t)e^{j\omega_0 t} \tag{2.20}$$

where $u(t)$ is the complex envelope

ω_0 is the carrier frequency.

Referring to Equation 2.16, the received signal (at an arbitrary sensor) is then given by:

$$\begin{aligned} r(t) &= E_t(\theta,\phi)E_r(\theta',\phi')\frac{1}{r_1}10^{-\frac{\alpha r_1}{20}}\frac{1}{r_2}10^{-\frac{\alpha 2}{20}}\rho(r,\theta,\phi)u(t-\tau)u(t)e^{j\omega_0(t-\tau)} + n_n(t) && (2.21)\\ &= \zeta u(t-\tau)e^{j\omega_0 t} && (2.22)\end{aligned}$$

where ζ is the complex coefficient that accounts for the following factors: position of the target in the transmitter and receiver beams ($E_t(\theta,\phi)E_r(\theta',\phi')$), the two-way propagation attenuation ($\frac{1}{r_1}10^{-\frac{\alpha r_1}{20}}\frac{1}{r_2}10^{-\frac{\alpha 2}{20}}$), the backscattering coefficient, in terms of pressure, of the target ($\rho(r,\theta,\phi)$), and the phase shift due to the two-way propagation ($arg(e^{-j\omega_0\tau})$). We therefore define the complex attenuation coefficient as:

$$\zeta = E_t(\theta,\phi)E_r(\theta',\phi')\frac{1}{r_1}10^{-\frac{\alpha r_1}{20}}\frac{1}{r_2}10^{-\frac{\alpha 2}{20}}\rho(r,\theta,\phi)e^{-j\omega_0\tau} \tag{2.23}$$

2.5.3 Signal

The waveform transmitted is a pulse with linear frequency modulation (chirp). The aforementioned pulse is often referred to as a pulse compression waveform and is very commonly used in radar and sonar signal processing [18]. The merits and choice of this pulse will be motivated further along this dissertation.

The signal is modulated linearly in frequency over the duration T, between the frequencies

$f_0 - \frac{B}{2}$ and $f_0 + \frac{B}{2}$. The pulse is defined as [40]:

$$s_{chirp}(t) = rect(\frac{t}{T})cos(2\pi[f_0 t + \frac{1}{2}Kt^2]) \tag{2.24}$$

with $K = \frac{B}{T}$.

f_0 is the centre frequency and B is the bandwidth of the pulse. From the definition in Equation 2.24, we deduce that the instantaneous frequency -the derivative of the phase- is given by:

$$f(t) = f_0 + Kt \tag{2.25}$$

and is displayed in Figure 2.11.

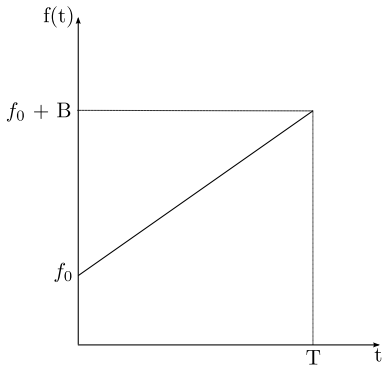

Figure 2.11: Instantaneous frequency of a linear chirp pulse

The pulse is characterised by its dispersion factor, which is also known as the *time-bandwidth* product [28]:

$$D = BT \tag{2.26}$$

The higher the product, the better is the Fourier spectrum defined. In other words, the higher the percentage of energy of the pulse in the band [28]. This will be illustrated further along this report.

Following the explanation in section 2.5.2, the analytic form of the chirp pulse is given by:

$$s_{chirp}(t) = rect\left(\frac{t}{T}\right) e^{j2\pi(f_0 t + \frac{1}{2}Kt^2)} \tag{2.27}$$

Note that the bandwidth of the transmitted pulse is given by the frequency deviation caused by the modulation.

2.5.4 Echo signal

Referring to the model for the received signal (Equation 2.22) and Equations. 2.27, the echo signal intercepted from a point target scatterer, when a LFM pulse is transmitted, is written as [17]:

$$r(t) = \zeta rect\left(\frac{t-\tau}{T}\right) e^{j2\pi(f_0(t-\tau)+\frac{1}{2}K(t-\tau)^2)} \tag{2.28}$$

where ζ is the complex attenuation coefficient and τ is the two-way propagation delay.

2.6 Limitations of the existing model

Simplifying assumptions have been made in modeling the environment. Moreover, a simplistic stochastic model has been used for the sonar target strength of targets.

Chapter 3

ABACUS Simulator

In the previous chapter, we developed a mathematical model for the operation of a multi-beam sonar. The model shows how data is determined by the transducers, antenna system, sonar target strength, and environmental parameters. This computational model is now used to develop software in the MATLAB package to simulate the physical behaviour of ABACUS. We also study the effect the configuration of ABACUS' receive and transmit arrays have on the directivity functions. We point out that the simulator is a quick and easy way to generate ABACUS-like data for various scenarios. Moreover, the simulator also offers flexibility to vary one parameter of the model and study the effects. This helps to test and benchmark signal processing techniques, asses the system's performances, and verify hypotheses.

3.1 Transmitter and Receive antennas

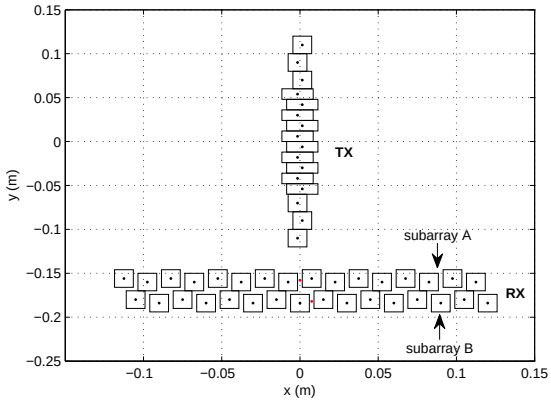

Figure 3.1: The physical layout of the ABACUS receive transmit/receive transducer arrays

In Figure 3.1, we see the perpendicular arrangement of ABACUS ' transmitter (Tx) and receiver arrays (Rx). The 16 identically-sized transmitter elements of dimension 0.012×0.020 m each, are ganged together and arranged along the y-axis. The elements at the extremities have different orientations and the elements are offset -right and left alternately- horizontally. The receiver subarrays (A and B) are arranged parallel to each other and consists of 16 elements of dimension 0.012×0.020 m each. The elements in each subarray are offset -up and down alternately- vertically. The beam pattern of the transmitter and receiver arrays are simulated and studied in section 3.3. Further information on the dimensions, calibration details and configuration can be obtained from the calibration manual for ABACUS [6].

3.2 Transmitted pulse

As mentioned in Section 2.5.3, the transmitted pulse is a linear frequency modulated pulse. The signal is apodized with a raised cosine based window (Hanning window) [34]to suppress the levels of sidelobe[1] [29]. The price of apodization is an increase in the beamwidth. ABACUS transmits at 420 kHz, which is relatively frequency for sonar systems. This offers the possibility of a wide bandwidth for the transmitted signal, and eventually higher resolution. The signal parameters are indicated in Table 3.1.

[1] A mathematical explanation of this statement will be given at a latter stage of this report.

Signal Parameters	
pulse duration, T	7 ms
pulse bandwidth, B	20 kHz
centre frequency, f_0	420.375 kHz
wavelength, λ	0.00364 m

Table 3.1: Transmitted signal parameters

The chirp pulse and its Fourier Transform are shown in Figure 3.2. And the effect of apodization is displayed in Figure 3.3.

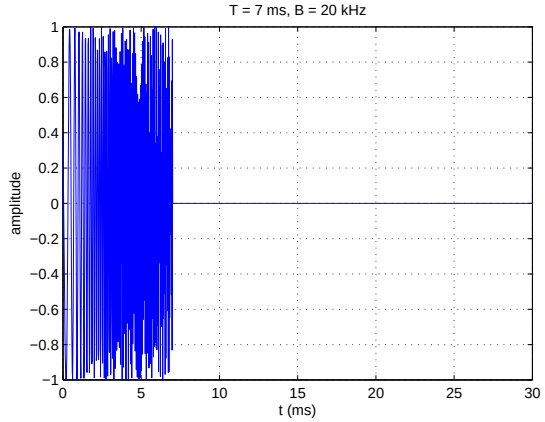

(a) Linear Frequency modulated pulse

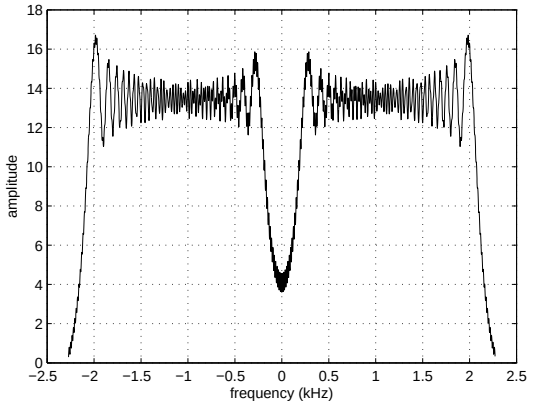

(b) Fourier Transform of linear chirp pulse

Figure 3.2: LFM pulse and its Fourier Transform

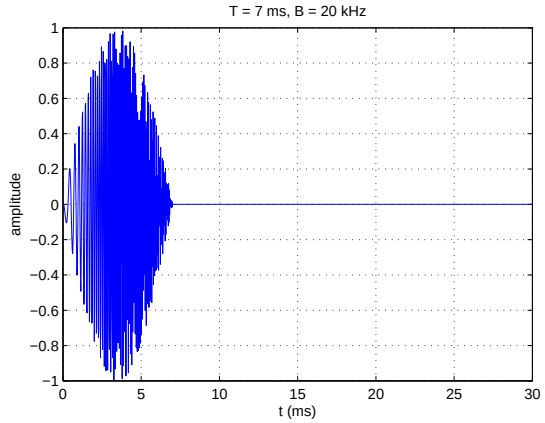

(a) Linear Frequency modulated pulse weighted by Hanning window

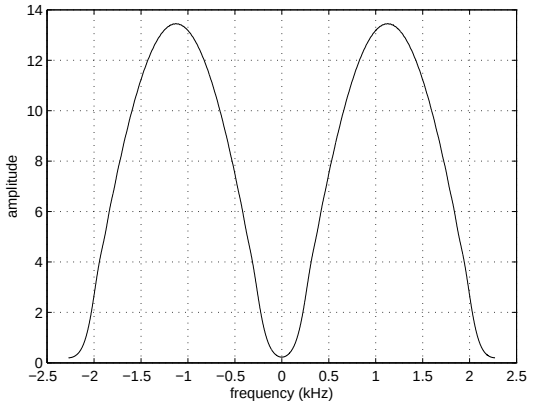

(b) Fourier Transform of apodized chirp pulse

Figure 3.3: Apodized LFM pulse and its Fourier Transform

From Figures 3.2 and 3.3, we deduce that weighting the transmitted signal by a window function reduces spectral leakage.

3.3 Beam pattern simulation

The mathematical model developed in Chapter 2 was used to simulate and investigate the directivity functions (beam patterns) of ABACUS' Tx and Rx arrays. Studied is whether the ABACUS' configuration improves the directivity by increasing the main-lobe-to-side lobe ratio[2], compared with generic linear phased arrays.

The beam patterns of a generic linear transmitter were simulated. The effect of changing the orientation -from horizontal to vertical- of the elements at the extremities are analysed. Further, we investigate the effect of offsetting the elements horizontally from the y-axis.

The simulations, based on the mathematical model developed in Section 2.2.4, are performed in the MATLAB package.

3.3.1 Beam Patterns of Generic Transmitter array

In this section, the beam directivity patterns or directivity functions of a generic linear transmitter, illustrated in Figure 3.4, are simulated.

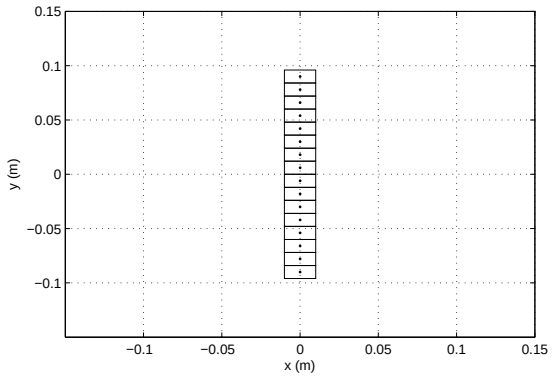

Figure 3.4: Layout of a generic transmitter

The simulated beam patterns in azimuth and elevation are depicted in Figure 3.5.

[2]It is verified whether this modification has the effect of aperture weighting to reduce sidelobes.

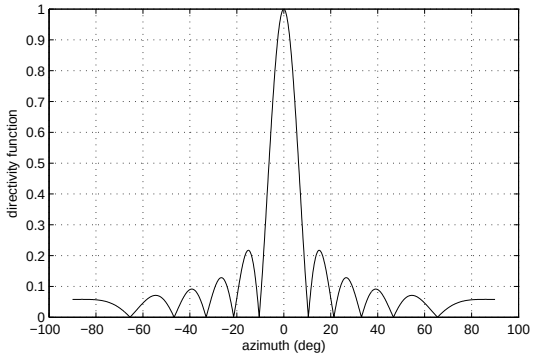

(a) Directivity function of generic Tx in azimuth

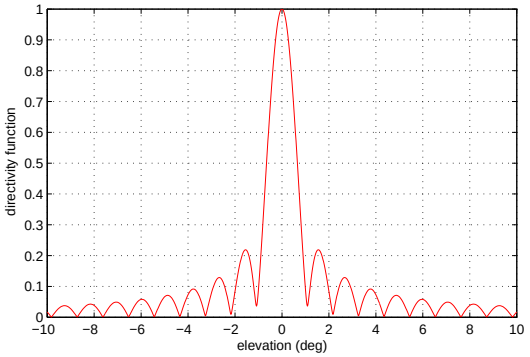

(b) Directivity function of generic Tx in elevation

Figure 3.5: Directivity functions of generic transmitter

3.3.2 Effect of changing the orientation of elements at the extremities of the transmitter

We now change the orientation of the topmost and bottommost three elements from horizontal to vertical as shown in Figure 3.7 and investigate the effects this change has on the beam patterns.

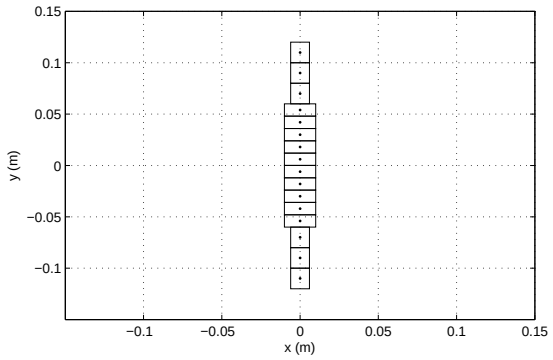

Figure 3.6: Generic transmitter layout with the orientation of elements at the extremities changed

The simulated beam patterns for the transmitter layout in Figure 3.6 are depicted in Figure 3.7 below.

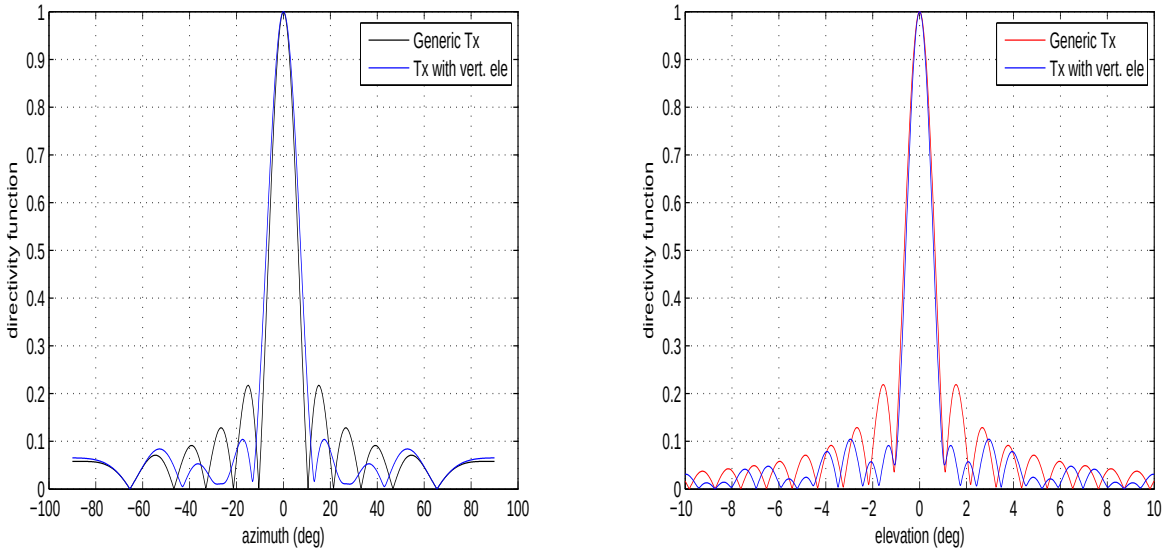

(a) Effect changing the orientation of the elements in azimuth

(b) Effect changing the orientation of the elements in elevation

Figure 3.7: Effect of changing the orientation of the elements at the extremities of the generic Tx on the directivity functions.

Observing the beam patterns in Figure 3.7, it is deduced that changing the orientation of the elements at the extremities produces a marked reduction in the sidelobe levels both in azimuth and elevation. However, we also note an increase in beamwidth in azimuth[3].

3.3.3 Effect of horizontal offsets (staggering)

We now offset the elements from the y-axis. The elements are offset alternately to the right and left by 0.015m as can be seen in the Figure 3.8 below.

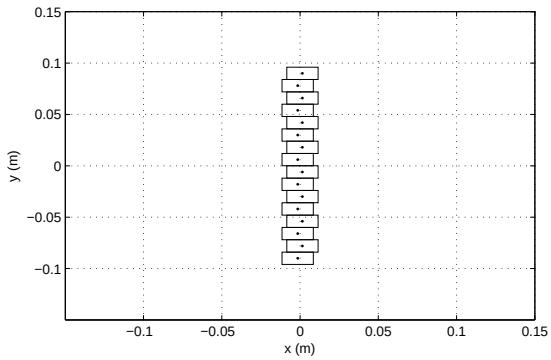

Figure 3.8: Transmitter array with its elements horizontally offset

[3]A larger beamwidth means lower angular resolution. The angular resolution is the smallest separation needed to distinguish between point targets in the angular dimension.

The simulated beam patterns of this transmitter arrangement are shown in Figure 3.9 below.

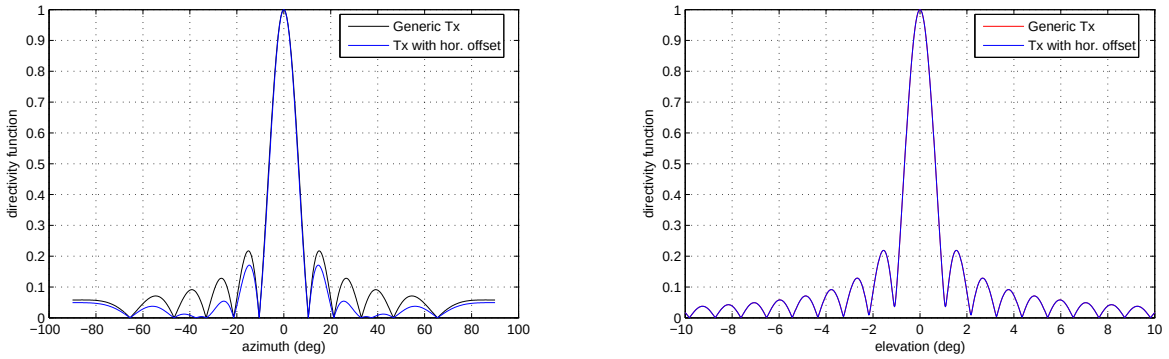

(a) Effect horizontally offsetting the elements in azimuth

(b) Effect horizontally offsetting the elements in elevation

Figure 3.9: Effect of horizontally offsetting the elements of the generic Tx on the directivity functions.

We note a decrease in the sidelobe levels in azimuth from this arrangement, relative to the generic array configuration. But there is no improvement in elevation.

3.3.4 Beam Patterns of the ABACUS Transmitter

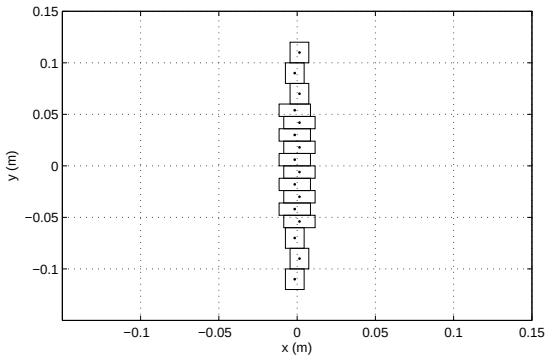

Figure 3.10: Layout of the ABACUS transmitter

We have seen that the alterations aforementioned, made from the transmitter configuration of a generic linear transmitter array, has the effect of reducing the sidelobes in both azimuth and elevation. Indeed, changing the orientation of the elements at the extremities, has the effect of decreasing the sidelobes in both azimuth and elevation. The horizontal offset of the elements reduces the sidelobes in azimuth, but has no effect on the

beam pattern in elevation. The simulation results of the combination of those two effects are displayed in Figure 3.11 below.

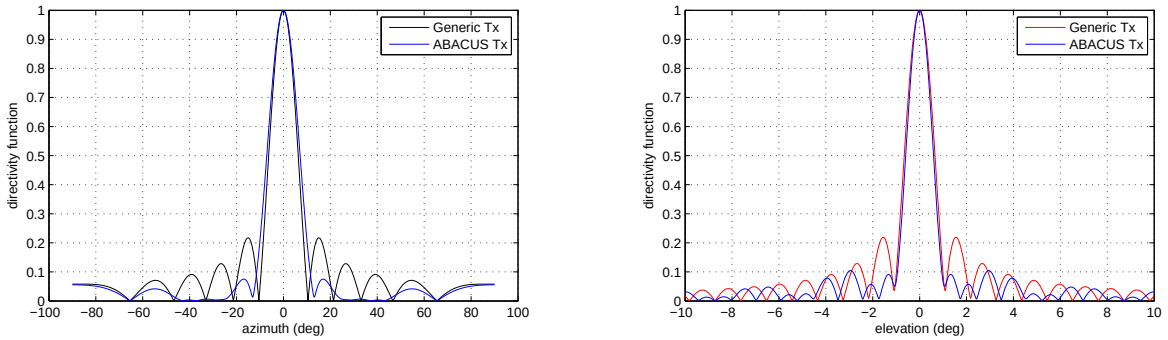

(a) Directivity functions of generic & ABACUS Tx in azimuth

(b) Directivity functions of generic & ABACUS Tx in elevation

Figure 3.11: Directivity functions of the ABACUS transmitter compared to those from the generic transmitter

3.3.5 Beam Patterns of a generic array receiver

We now simulate the beam patterns of the ABACUS receiver subarrays. As was done for the ABACUS transmitter array, we use the mathematical model developed in Section 2.2 to generate the patterns. Along the way, we also study the effects of the staggering (vertical offsets) of the receiver elements.

The beam patterns of a generic phased array shown in Figure 3.12 are displayed in Figure 3.13.

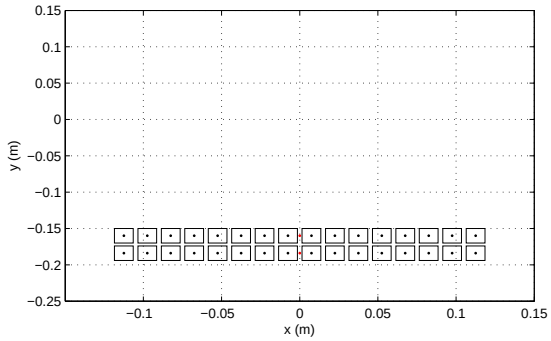

Figure 3.12: Layout of generic receiver

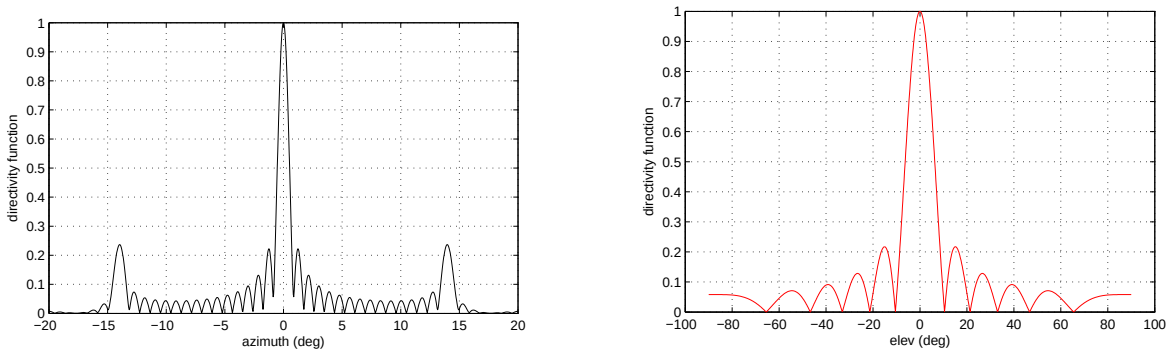

(a) Directivity function of generic receiver in azimuth (b) Directivity function of generic receiver in elevation

Figure 3.13: Directivity functions of a generic receiver

3.3.6 Beam Patterns of the ABACUS receiver subarrays

As can be seen from the layout of the ABACUS receiver arrays in Figure 3.14, the receiver elements are offset from the horizontal, alternately up and down. From the simulations results derived in the preceding sections for the ABACUS transmitter, we can postulate that the offset has no effect on the beam pattern in azimuth but reduces the sidelobes in elevation.

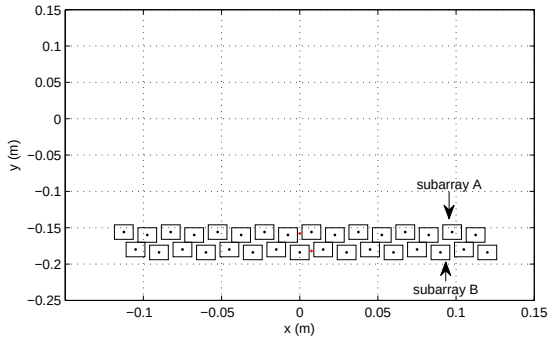

Figure 3.14: Layout of the ABACUS receiver arrays

This is verified from the simulation results in Figure 3.15.

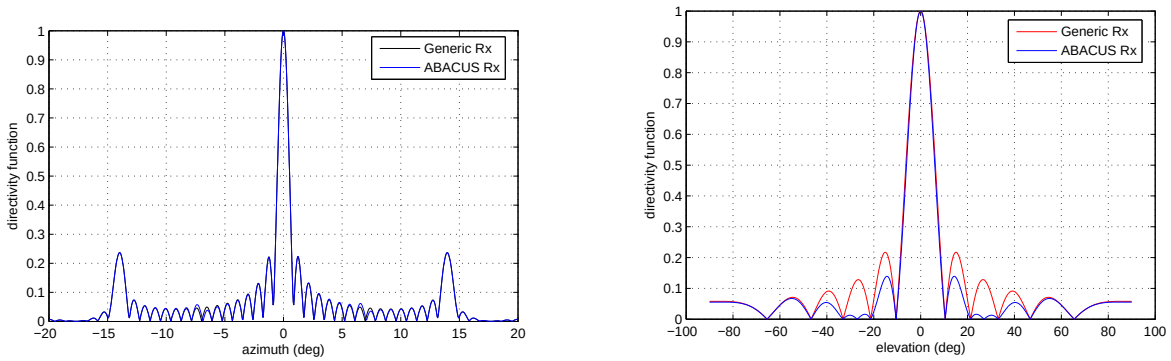

(a) Directivity functions of generic and ABACUS Rx in azimuth

(b) Directivity functions of generic and ABACUS Rx in elevation

Figure 3.15: Directivity functions of the ABACUS receiver compared to those from the generic receiver

3.3.7 Beam Patterns of receiver subarrays in interferometric mode

Although ABACUS consists of two receiver subarrays with 16 elements each, in interferometric mode[4], only eight elements from each subarray are sampled. This is due to the sampling card of the ABACUS system being presently limited to 16 channels only, instead of the possible 32.

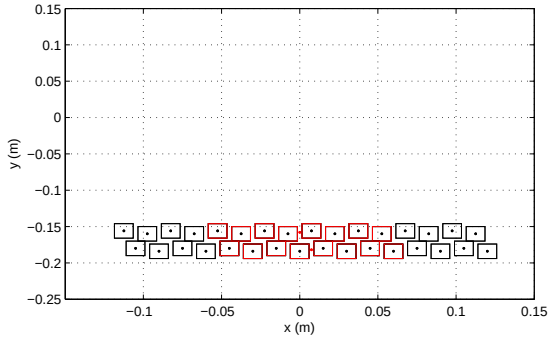

Figure 3.16: Layout of ABACUS receiver in interferometric mode

[4]The concept will be elaborated in the latter sections of this dissertation.

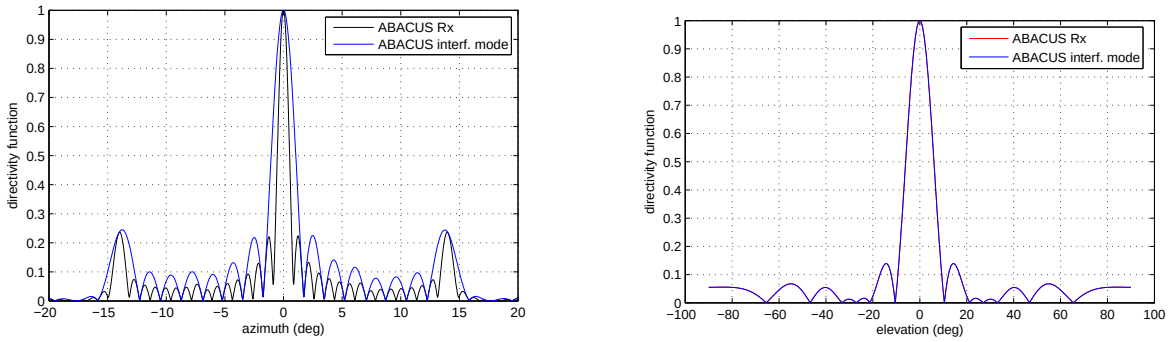

(a) Directivity functions in azimuth

(b) Directivity functions in elevation

Figure 3.17: Directivity functions of the ABACUS receiver in interferometric and normal modes

From Figure 3.17, it can be deduced that the angular resolution in azimuth deteriorates, for only eight elements are used, as opposed to 16. This reduction in receiver length decreases the angular (azimuth) resolution, which is determined by the receiver length in the horizontal dimension according to: $\theta_a = \frac{\lambda}{L}$, where λ is the wavelength, L is the receiver dimension in the horizontal dimension, and θ_a is the angular resolution in azimuth.

3.3.8 Summary of beam patterns

The beamwidths of the directivity functions of the transmitter and receiver patterns are shown in Tables 3.2 and 3.3.

	Generic	ABACUS simulated
θ_{3dB} (°)	9.14	10.28
ϕ_{3dB} (°)	0.96	0.86

Table 3.2: Beamwidths of the generic and ABACUS transmitters

The 10 dB beamwidths of the transmitted beam are 17.75°in azimuth and 1.47° in elevation.

	Generic	ABACUS normal mode	ABACUS interferometric mode
θ_{3dB} (°)	0.78	0.78	1.56
ϕ_{3dB} (°)	9.33	8.80	8.80

Table 3.3: Beamwidths of the generic and ABACUS receivers

Referring to Figure 2.1, which depicts the operation of a phased-array sonar, a resolution

cell (part of scene being observed) is defined by the steerable receiver beam[5] in azimuth and the transmitted beam in elevation. The resolution cell is defined by the 3 dB beams, thus giving the resolution cell of the ABACUS system to be $1.56^\circ \times 0.86^\circ$ in interferometric mode.

It is therefore deduced that vertical offsets (stagger) in the configuration of ABACUS' receiver offers no discernible advantage (sidelobe level reduction[6] or smaller beamwidth) to the system but, as predicted, in interferometric mode, ABACUS system' resolution in azimuth is reduced by a factor of two.

Further, the transmitted beam is improved (higher mainlobe to sidelobe ratio) in elevation by changing the orientation of the elements on the ends of the Tx. This is beneficial in that sidelobe levels are reduced, thus suppressing strong targets that are outside the ensonified resolution cell.

3.4 Receiver

The geometry of the receiver elements has been detailed in section 3.1. Echoes from targets in the scene are received by elements of the two receiver subarrays (A and B).

3.4.1 Sampling

The signals are bandpass filtered, and amplified before being digitised. The digitisation is done by 12 bit ADCs, and the sampling rate is determined by the Nyquist Theorem for bandpass signals. It states that the minimum sampling frequency, for a bandpass signal, is dependent on its bandwidth instead of its highest frequency. The theory indicates that in sampling bandpass signals, we can make efficient use of the frequency spectrum by maximising the number of replicas that are inserted between the original spectral densities. This leads to the minimum requirement for the sampling rate to being between twice and four times the bandwidth, if we are to sample at uniform time intervals. Further, it is given that the minimum sampling rate requirement tends to, twice the bandwidth as the centre frequency increases[35]. The ABACUS system's sampling rate is 45.455 kHz which is slightly higher than twice the bandwidth of 20 kHz, therefore, allowing for some spectral leakage.

[5] The beam is steered by the process of beamforming implemented in software.

[6] The low sidelobe levels reduce echoes from targets outside the resolution cell, as indicated by Equation 2.16.

The output of the 12 bit ADCs produces $2^{12} = 4096$ states or range samples. This amounts to $dt \times 4096 = \frac{1}{F_s} \times \text{No of samples} = \frac{1}{45455} \times 4096 = 90$ ms, in observation time. We note that dt is the time sampling interval. ABACUS records data for a period of 90 ms. Now, it would be ideal to send pulses at intervals of slightly more than 90 ms for an optimum observation of the undersea environment, in time. However, the ABACUS data system was set to a PRF of 1 Hz. It is noted that the system can sample at a faster rate.

The time of observation is translated to a range, r, of observation using the (two-way delay equation) $r = \frac{c\tau}{2}$, where τ is the two-way propagation time. Hence, the maximum range that the ABACUS system is capable of observing is approximately $\frac{1530 \times 90e-3}{2} = 68\,\text{m}$. In the above calculations, the transmitter and receiver are assumed to be at the same position. Further, the range range sampling intervalΔr is $\frac{c \times dt}{2} = \frac{1530 \times \frac{1}{45455}}{2} = 0.0168\,\text{m}$. The ADC is synchronized to start sampling at the same time the pulse is transmitted. The implication is that we cannot record the received data during that duration, due to the transmitted pulse being much higher in amplitude than the received echo signals, thus saturating the receiver via direct coupling or reflections. The pulse length can be shortened, to allow closer in imaging (if required).

ABACUS' data capture system can, presently, only sample 16 channels. This limitation denies the ABACUS its full potential in terms of angular resolution. Alternatively, we have the choice of several configurations:

1. To use the middle eight elements of each subarray to form two images. This configuration is the focus of this dissertation as we use the two complex images formed from each subarray for phase interferometry. This configuration is shown in Figure 3.16.

2. To use the 16 elements of either subarray A or B to form an image. This configuration would offer optimum angular resolution.

3. To use the middle eight elements from each subarray to form one image. In this mode, we can study whether we can extend the azimuth span (scanning dimension of landscape in azimuth), which is limited by grating lobes.

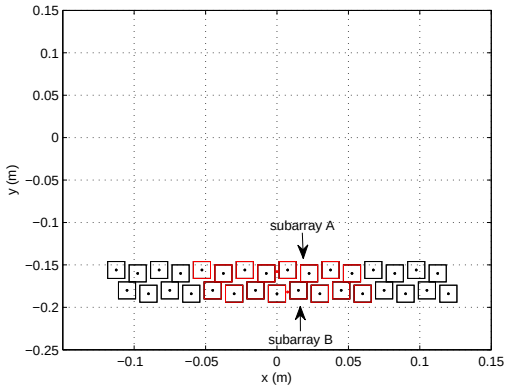

Figure 3.18: Receive elements mapped to data capture system in interferometric mode

The Table 3.4 summarises the system parameters.

System Parameters	
Number of channels, N	16
sampling rate, F_s	45.455 kHz
Number of samples	4096
PRF	1 Hz
range sampling interval, Δr (m)	0.0168
observation range (m)	10.5-68

Table 3.4: ABACUS system parameters

The system parameters of the ABACUS detailed above are to be input in our software development for the simulator.

3.5 Submarine Environment

The ABACUS simulator defines the 3-D volume of the sea being ensonified by the transmitter beam. Further, the ocean volume is represented by a cuboid, the dimensions of which can be specified in the simulator. Targets simulated are confined to this region. Figure 3.19 shows a simplified geometry of the volume being ensonified.[7]

The simulator developed offers the options of placing any number of targets in specified positions, or alternatively the random positioning of point targets in the volume depicted in Figure 3.19.

[7]In Figure 3.19, we depict the simplified geometry of the transmitter beam pattern. Boundaries are defined by the 10 dB beamwidth of the transmitter beam.

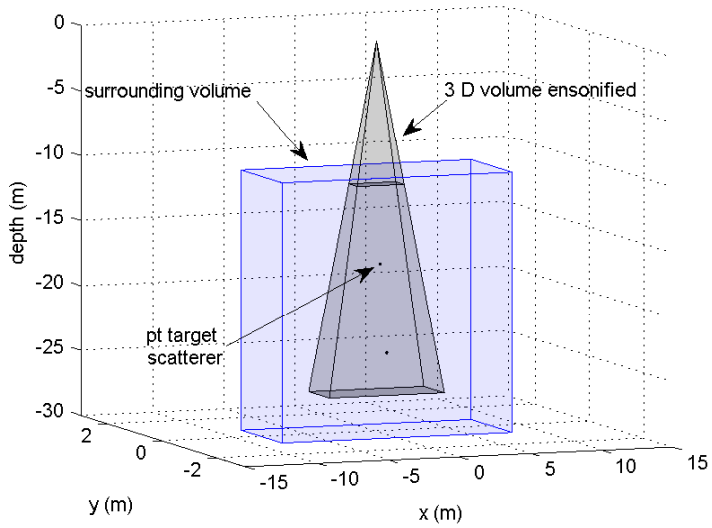

Figure 3.19: Submarine environment model

3.5.1 Noise

As explained in Section 2.4.2, the time signal for the noise model is defined by a zero mean Gaussian distribution with a standard deviation σ, which determines the noise level (ambient sea noise and receiver noise) in the simulator at each channel (output of ADC). Figure 3.20 shows the simulated noise time signal simulated and its distribution at one of the receivers[8]. Accurate noise measurements and environmental parameters are not available. Therefore, to simulate accurately realistic noise levels at the receivers, the noise levels (σ) were estimated from parts of the data obtained from pelagic surveys, where it is assumed no targets were present.

[8]The standard deviation has been set to an arbitrary value to produce the figures.

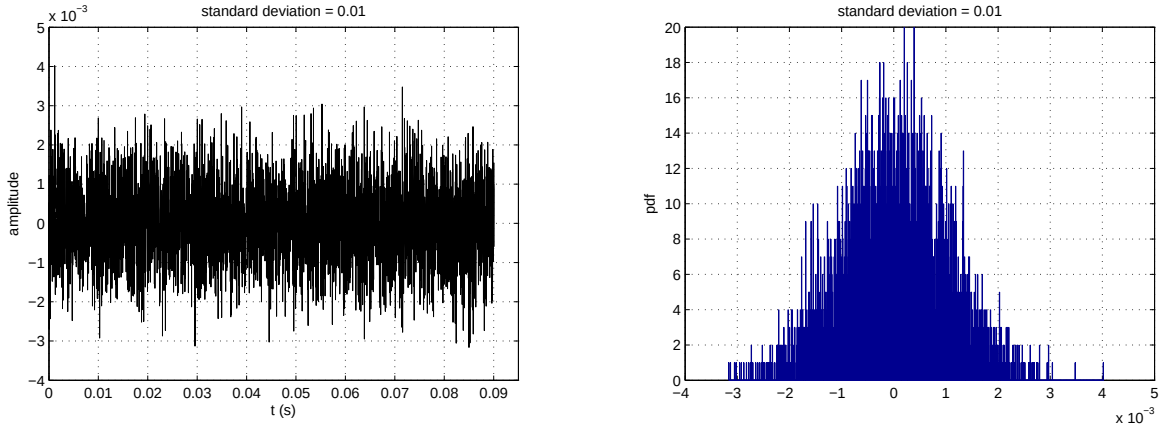

(a) Noise time signal at one receiver

(b) Gaussian random process

Figure 3.20: Noise time signal and its pdf

3.5.2 Point Target Scatterers

In the simulator, we define targets as pointlike reflectors with: either unit reflectivity (sonar target strength of one); or with a sonar target strength from the Rayleigh distribution modeled in section 2.4.1.

3.6 Synthetic data

We now simulate the received signal, for a chirp reflected from targets in the scene. Recall that the received signal is determined by the antenna system, transducers, the position of the targets relative to the receiver and transmitter, the sonar target strength and environmental parameters as modeled in Section 2.5. Figure 3.21 shows the data $|r(t, n)|$ at one of the channels, obtained from simulating the received signal from two pointlike unit reflectors in the scene. The data has been scaled by a factor k that maps the voltage across the transmitter terminals to the quantised receiver voltage (signed 12 bit number), for the synthetic data to be of the same order of magnitude as the data obtained from pelagic surveys of fish. It is deduced that the received echo signal bears information about the scene, which is not discernible until the signals are processed.

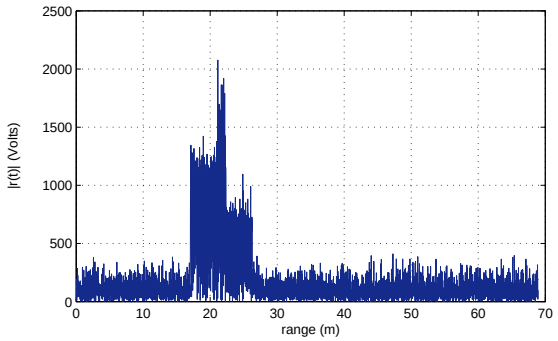

Figure 3.21: Received signal $r(t)$ at one of the output of channels

Chapter 4

Signal Processing

In the previous chapters, we developed a mathematical formulation and simulated echo signals intercepted by the ABACUS receiver from the submarine environment. It was shown how the signals are received by the transducers, sensor layout, and more importantly by the targets and other environmental parameters in the scene being ensonified. The process is generally referred to as the "forward problem" [4]. We deduce that the signals bear information about the scene, but are impaired by noise and other interfering factors. In this chapter, we review and detail the signal processing techniques that are applied to the echo signals to extract information about the scene. The process is known as the "inverse problem". We perform time processing -pulse compression- to estimate the range and space processing -digital beamforming- to find the angular location of possible targets. Those parameters are then used to form a 2-D image of the scene. It is to be noted that digital beamforming is performed only in azimuth. Therefore, the image only displays the bearing as a function of range and azimuth angle. As mentioned in Section 3.1, there are only two receiver elements in the y-axis (elevation), which implies that beamforming in elevation would result in very poor angular resolution. As a means of overcoming this limitation, we use the technique of phase interferometry to resolve the elevation angle of arrival. We perform phase subtraction on the two complex images formed from the two receive subarrays to determine the angle of arrival in elevation. We thus resolve the three dimensional bearing of the targets detected.

4.1 Pulse compression

According to the model developed in Chapter 2, the intercepted signal is a delayed replica of the transmitted signal. Moreover, the signal is multiplied by a complex attenuation coefficient and contaminated by additive white Gaussian noise. Assuming that the target and sonar are fixed relative to each other, frequency shifts can be ignored. Hence, it is deduced that the received signal contains information on the target range by its delay relative to the transmitted signal. We need to solve the basic problem of measuring the delay. Theory suggests that the accuracy of the measurement depends, amongst other parameters of the transmitted signal, on the duration T of the signal, the width of the frequency band B it uses and the modulation index m of the signal, which is zero if the signal is only modulated in amplitude. The concepts will be elaborated further along this discussion. We now delve into the theory and concepts involved in measuring the range [18].

The measurement of target range is achieved by pulse compression. In general, radars or sonars that use a modulation of the transmitted pulse are referred to as pulse compression systems. The ABACUS transmitter modulates the frequency of the pulse so that the modulation index is not zero, as detailed in Section 2.5.3. The pulse compression term originates from the fact that the receiver filter produces a compressed -shorter in duration- pulse at its output. This becomes obvious in the treatment of the receiver concept which follows. Pulse compression can be achieved using a matched filter or an ideal reconstruction filter [40].

It is important to note that in general, in sonar systems there are some performance metrics to consider:

1. the signal-to-noise ratio χ which determines detection performance[1] and location accuracy. To achieve a high signal-to-noise ratio and detection performance, for a simple pulse (of amplitude A and duration T), we ideally want to have a long duration T, since the energy of the pulse is proportional to its duration.

2. the range resolution δr, which is the closest distance between which we can distinguish between pointlike reflectors in range. For a simple pulse, δr is given as [40]:

$$\delta r = \frac{cT}{2} \tag{4.1}$$

which translates to:

$$\delta r \approx \frac{c}{2B} \tag{4.2}$$

[1] This will be elaborated in latter chapters, where the detection of targets is treated.

since the relation between the duration and the bandwidth of a signal is given as [18]:

$$BT \geq \frac{1}{4\pi} \tag{4.3}$$

which implies that the shorter a signal, the wider the bandwidth.

To summarise, we want as long a duration as possible to maximise signal-to-noise ratio, but a low duration (implying wide B) to maximise the range resolution. We see that the two metrics are linked and it is not possible to maximise both of them using a simple pulse.

The above treatment is a justification for the use of a frequency modulated pulse, as will be explained in the following section.

4.1.1 Matched filter

The matched filter at the receiver is generally implemented to estimate the parameters of a signal of known form and unknown amplitude and phase in the presence of additive white Gaussian noise. An important characteristic of the matched filter receiver is that it optimises the signal-to-noise ratio in the presence of white noise [29]. It is given that the frequency and impulse responses of the filter that maximises the signal to noise ratio are given as [29][2]:

$$\begin{aligned} H(\omega) &= X^*(\omega) \\ h(t) &= x^*(-t) \end{aligned} \tag{4.4}$$

where $X(\omega)$ is the frequency response of the input signal (which is the received signal $r(t)$ in the ABACUS system) to the filter. It is assumed that the overall frequency response of the ABACUS has a band limited spectrum with a bandwidth equal or just greater than the bandwidth of the transmitted pulse (shown in Figure 3.3). It is to be noted that the impulse response of the filter is a time-reversed and conjugated replica of the complex transmitted waveform. Hence, the name matched filter. The optimum signal-to-noise ratio is given by [29]:

$$\chi = \frac{2E}{N_0} \tag{4.5}$$

where E is the energy of the pulse and $\frac{N_0}{2}$ is the spectrum of the white noise.

[2]The derivation of the frequency response to achieve optimum signal to noise ratio is given in [29].

Referring to Equation 4.4, the output of the matched filter is then given by the convolution:

$$\begin{aligned} y(t) &= \int_{-\infty}^{\infty} x(t-\kappa)h(\kappa)d\kappa \\ &= \int_{-\infty}^{\infty} x(t-\kappa)x^*(-\kappa)d\kappa \end{aligned} \tag{4.6}$$

Now for the case where the input signal to the matched filter is the -delayed replica of the sent signal $s(t)$- $r(t) = s(t-\tau)$, the output is modified to:

$$y(t) = \int_{-\infty}^{\infty} s(t-\tau-\kappa)s^*(-\kappa)d\kappa \tag{4.7}$$

Equation 4.7 suggests that matched filtering is a cross correlation of the sent signal with the received signal. Further, we deduce that the cross correlation function in Equation 4.7 peaks when $t-\tau-\kappa = -\kappa \Rightarrow t = \tau$, which is the two-way propagation delay. Thus we have shown that matched filtering enables us to measure the range of the target.

We point out that, in the case of a simple pulse (modulation index of zero) of duration T, the output of the matched filter is of duration $2T$. In the next section, we study the use of frequency modulation of the pulse helps compress the duration of the output of the filtering process.

We further note that if the received signal contains echoes from several point like reflectors, the matched filter output, by the superposition principle, will have several responses at peaks corresponding to the respective ranges.

We now follow the implementation of the matched filter mathematically, in the ABACUS system and see how the frequency modulated pulse helps achieve pulse compression through matched filtering.

Following our signal model, the received signal $r(t)$ (input to matched filter) from a point target scatterer is given as in Eq 2.22:

$$r(t) = \zeta u(t-\tau)e^{j\omega_0 t} \tag{4.8}$$

We recall that the output of the matched filter is given as:

$$Y(\omega) = H(\omega)X(\omega) \tag{4.9}$$

For our signal model, this translates to:

$$\begin{aligned} Y(\omega) &= \left(\mathcal{F}\left\{u(t)e^{j\omega_0 t}\right\}\right)^* \mathcal{F}\left\{\zeta u(t-\tau)e^{j\omega_0 t}\right\} \\ &= \zeta U^*(\omega-\omega_0)U(\omega-\omega_0)e^{-j\omega\tau} \\ &= \zeta \left|U(\omega-\omega_0)\right|^2 e^{-j\omega\tau} \end{aligned} \tag{4.10}$$

It is noted that the Wiener-Khinchin theorem, $U^*(\omega-\omega_0)U(\omega-\omega_0) = \left|U(\omega-\omega_0)\right|^2$, is used to obtain Equation 4.10.

In the case of the ABACUS system, the envelope $u(t)$ is the linear frequency modulated pulse (chirp pulse). The magnitude of the Fourier Transform of the LFM pulse is approximated as [40]:

$$\left|\mathcal{F}\left\{s_{chirp}(t)\right\}\right| \approx rect\left(\frac{\omega-\omega_0}{\Delta\omega}\right)\frac{1}{\sqrt{|K|}} \tag{4.11}$$

Therefore, if we insert the Fourier Transform of the chirp pulse in equation 4.10, we have:

$$Y(\omega) \approx \zeta rect\left(\frac{\omega-\omega_0}{\Delta\omega}\right)\frac{1}{|K|}e^{-j\omega\tau} \tag{4.12}$$

which in time domain translates to:

$$y(t) = \zeta\frac{1}{|K|}e^{j\omega_0 t}\frac{\Delta\omega}{\pi}Sa\left(\frac{\Delta\omega(t-\tau)}{2}\right) \tag{4.13}$$

The above treatment and Equation 4.13 indicate that matched filtering -in a pulse compression system- of a frequency modulated pulse produces Sa impulse with a peak at $t=\tau$ for of a point like reflector at range r. We note that the Rayleigh resolution of the Sa function is approximately $\frac{1}{B}$, which is an improvement by a factor of BT over the resolution of the matched filtered output of a single unmodulated pulse, which is T (the duration of the signal). Therefore, it has been shown that matched filtering has enabled pulse compression. Frequency modulation effectively increases the time-bandwidth product to much greater than one.

$$\begin{cases} BT &= 1 \quad \text{for unmodulated pulse} \\ BT &\gg 1 \quad \text{for modulated pulse} \end{cases} \tag{4.14}$$

Thus, frequency modulation enables the separate control of the two performance metrics aforementioned, pulse energy or SNR (through its duration) and range resolution (through its bandwidth). In short, frequency modulation enables the optimisation of

both performance metrics.

It is noted that Figure 3.21 shows the received signal from two point target scatterers located at coordinates $\langle 17, 0.7°, 0° \rangle$ and $\langle 21, -1.4°, 0° \rangle$. For case of development the synthetic data displayed in Figure 3.21 is to be processed to illustrate the signal processing concepts along the course of this chapter.

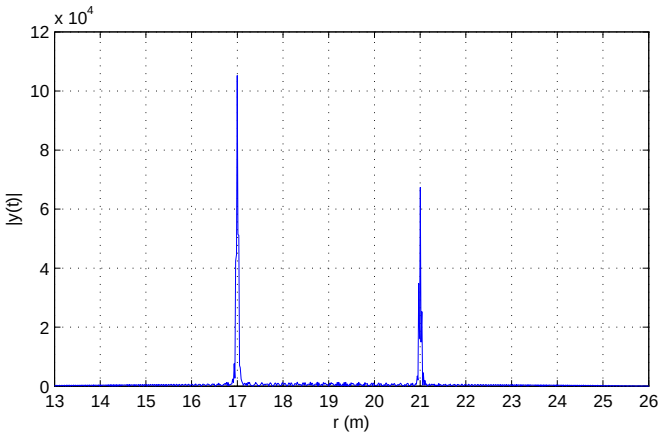

Figure 4.1: Range profile

Figure 4.1 shows that pulse compression, achieved through matched filtering enables the measurement of the range of the point targets.

4.2 Demodulation

The receiver demodulates the received signal to baseband. In terms of our analytic model, we derive the baseband signal:

$$z(t) = r(t)e^{-j2\pi f_0 t} \tag{4.15}$$

This mathematical operation is also referred to as coherent detection. In fact, in terms of hardware, which deals with real valued signals, the receiver is split into an in-phase and a quadrature channel to measure the phase unambiguously. We now study the demodulated received signal.

From Eqs 4.13 and 4.15, we derive:

$$z(t) = \zeta \frac{1}{|K|} \frac{\Delta\omega}{\pi} Sa\left(\frac{\Delta\omega(t-\tau)}{2}\right) \tag{4.16}$$

Referring to Eq 2.23, the complex attenuation coefficient ζ comprises of the phase shift

due to the two-way propagation delay. Hence, the phase shift is:

$$arg\left\{\zeta\right\} = arg\left\{e^{-j2\pi f_0 \tau}\right\} \tag{4.17}$$

Substituting $\tau = \frac{2r}{c}$ and $f_0 = \frac{c}{\lambda}$, we have:

$$arg\left\{e^{-j2\pi f_0 \tau}\right\} = -2 \times \frac{2\pi}{\lambda} r \tag{4.18}$$

Hence, it can be deduced that the phase of the demodulated response from a pointlike reflector, is constant over a range sampling interval. This can be verified in Figure 4.2 . Further, it is to be noted that a change of $\frac{\lambda}{4}$ in range causes an 180° phase shift. Figure 4.2 indicates that the phase wraps. This is due to the fact that the the phase is confined to the range $[-\pi, \pi]$, which is the principle argument of the arctan function.

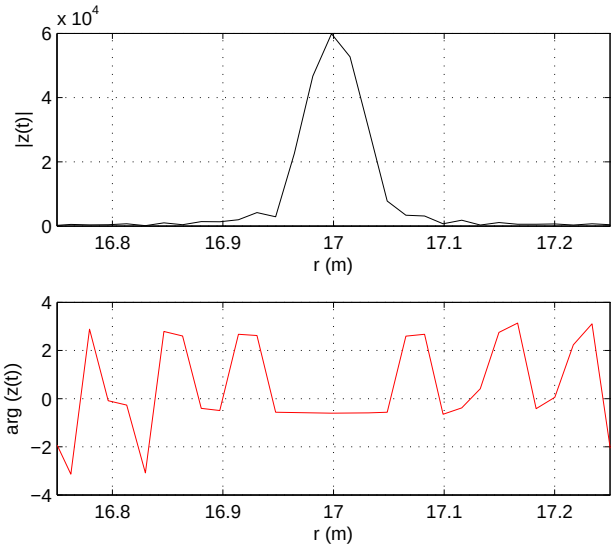

Figure 4.2: Range profile (zoomed in, at $r = 17$ m) at baseband

4.3 Range side lobe control

From Section 4.1, pulse compression systems produce Sinc like function responses with high unwanted sidelobes. This is a consequence of the rectangular nature of the Fourier Transform of linear frequency modulated signals with relatively high BT[3]. The sidelobes are a limiting factor in situations of multiple targets that are close in range. Targets which produce weaker echoes are masked by the high sidelobes of stronger targets. Hence, it is essential to minimise the sidelobes to improve the reliability of detection. We briefly

[3]The phenomenon is referred to as the *Gibbs phenomenon* in Fourier series theory.

review the methods described in literature used to reduce the sidelobe levels and detail the method used in the ABACUS system.

4.3.1 Matched filtering frequency response shaping

The frequency response of the matched filter is modified by multiplication of a window function. The matched filter response is then given by [29]:

$$H^{'}(\omega) = W(\omega)X^{*}(\omega) \tag{4.19}$$

This has the effect of tapering the ends of the rectangular spectrum of the correlation in the frequency domain, which translates to lower sidelobes in the time signal response. The extent of the sidelobes reduction will be discussed further in this section.

The filter response is not exactly matched to the transmitted pulse. The discussion in Section 4.1.1 implies that the signal-to-noise ratio is no longer optimised. Further, windowing the filter response effectively reduces the frequency band the response uses, therefore the range resolution ($\delta r \approx \frac{c}{2B}$) deteriorates. This is demonstrated as the broadening of the main lobe of the Sinc impulse.

4.3.2 Waveform Spectrum Shaping

The frequency response shaping technique is limited in that the signal-to-noise ratio is not optimised. An alternative technique is to design pulse compression waveforms that assume a tapered spectrum (window like spectrum), and hence inherently have low sidelobes [29]. This is generally achieved by either:

1. amplitude modulation, where the signal amplitude is reduced at the pulse edges, while keeping the frequency modulation linear.

2. or using non-linear frequency modulation, where the frequency is swept faster at the edges (implying shorter time spent in spectral interval at the edges), while keeping the amplitude constant.

This technique reduces the signal energy and eventually the signal-to-noise ratio, but the latter is still optimised.

4.3.3 Range sidelobe control in the ABACUS system

The ABACUS implements waveform spectrum shaping. A window function is superimposed on the linear frequency modulated chirp pulse transmitted, shown in Figure 3.3a. This function tapers the amplitude at the pulse edges. The window function is the square root of a Hanning window and is given by [26]:

$$w[n] = \begin{cases} sqrt(0.5 - 0.5cos(2\pi n/M)), & 0 \leq n \leq M \\ 0, & \text{otherwise} \end{cases} \tag{4.20}$$

where n an integer denoting the sample number of the discrete-time signal and M is the total number of samples. The choice of the Hanning window was motivated by the fact it forces the pulse edges to zero, which translates to the frequency spectrum being forced to zero. This minimises spectral leakage as can be deduced from Figures 3.2 and 3.3. This exercise is particularly important in the context of the ABACUS system which implements a sub-sampling scheme.

An alternative signal processing step can be implemented to reduce sidelobes in range. A window function can be applied to the range profile in the frequency domain to shape (taper) the spectrum at each end. The window function is chosen by the desired reduction in sidelobes level, constrained by the broadening of the mainlobe (deterioration in range resolution). A comparison of commonly used windows is indicated in Figure 4.3. For the ABACUS system, we propose a Hamming window which is defined as:

$$w_{hamming}[n] = \begin{cases} 0.54 - 0.46cos(2\pi n/M), & 0 \leq n \leq M \\ 0, & \text{otherwise} \end{cases} \tag{4.21}$$

Weighting function	Peak Sidelobe (dB)	3dB Mainlobe width (relative)	Sidelobe decay f'n.
Uniform	−13.2	1.0	$\frac{1}{i}$
$0.33 + 0.66\cos^2(\frac{\pi f}{B})$	−25.7	1.23	$\frac{1}{i^2}$
$\cos^2(\frac{\pi f}{B})$	−31.7	1.65	$\frac{1}{i^3}$
Hanning: $0.5 - 0.5\cos(\frac{\pi f}{B})$	−31	1.6	$\frac{1}{i}$
Taylor ($\overline{n} = 8$)	−40	1.41	$\frac{1}{i}$
Dolph-Chebyshev	−40	1.35	1
Hamming: $0.54 - 0.46\cos(\frac{\pi f}{B})$	−41	1.50	$\frac{1}{i}$
Blackman: $0.42 - 0.5\cos(\frac{\pi f}{B}) + 0.08\cos(\frac{2\pi f}{B})$	−57	1.9	

Figure 4.3: window functions for sidelobe suppression (Skolnik 1981, and other sources) [39]

4.4 Time-Domain Interpolation by Zero-Padding in the Frequency Domain

The ABACUS system is limited to 4096 samples per channel by the 12 bit ADCs. In the case of a range profile, with Sa pulses, a range resolution interval δr is only defined by $\frac{\delta r}{dr} \approx 2$ samples, where dr is the range sampling interval. Hence, the time signals at each channel are interpolated to increase the number of sample points so that their graphical representation is enhanced and the accuracy of the subsequent digital beamforming operation is improved[4]. The technique used to interpolate the time signals is referred to as Bandlimited Interpolation, for it corresponds to the use of an ideal low-pass filter. The technique consists of extending the spectrum of the time signal with zeros and then taking the Inverse Discrete Fourier Transform (IDFT) of the extended spectrum.

'Zero padding' in one domain corresponds to an 'increased sampling rate' in the other domain. It is common signal processing practice to append zeros to a time signal to increase the sampling rate in the frequency domain. In other words, to make the frequency sampling spacing finer and displaying more sample points [20].

To interpolate the time signals at each channel, we proceed as follows:

We take the N point FFT of the time signal $x[n]$ which is mathematically given as:

$$X[k] = \sum_{n=0}^{N-1} x[n] e^{\frac{-j2\pi kn}{N}} \tag{4.22}$$

$X[k]$ is the spectrum of the time signal. One of the properties of the DFT (Discrete Fourier Transform) is that it is periodic. Hence, it needs only be defined in the range $[0, Fs]$, where Fs is the sampling frequency. The spectrum is stored in the computer array such that the positive frequency components are in the first half and the negative frequency components in the second half of the array. Moreover, another property of the spectrum (DFT) is that of conjugate symmetry if the time signal is real. Hence, the above properties suggest that we need to "zero pad" the middle of the spectrum $X[k]$. For example, to interpolate by a factor of four, we create an array of length $4N$ with data in the first $N/2$ array elements of the $X[k]$ array, zeros in the next $3N$ elements, and insert the elements $N/2 + 1$ to N from the $X[k]$ array.

The last step is to compute the Inverse Discrete Fourier Transform ($IDFT$) of the zero-padded vector by taking a $4N$ points $IFFT$.

[4]Interpolation fills in more detail, thus more accurate sample value can be obtained. This is will be elaborated on, in the following section.

The result is a time signal with four sample points for each sample point of the original time signal. No new information has been added to the signal, but more sample points are displayed. Figure 4.4 shows the 'interpolated' range profile with finer sampling intervals than the intervals in Figure 4.2.

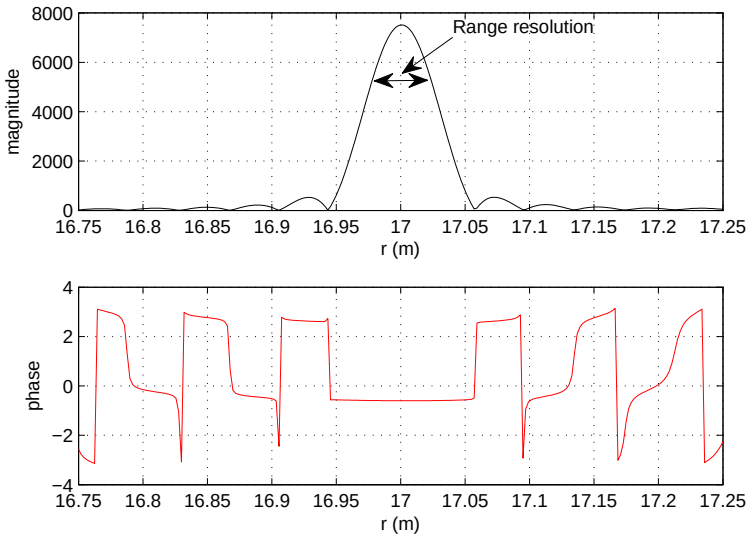

Figure 4.4: Interpolated range profile, zoomed in at $r = 17.0$ m

4.5 Angular Location

In the previous sections, we measured the range of a target by its relative delay to the transmitted signal. The signal model suggested that the received signal is also modified by the angular position of a target in the volume insonified. In practice, the angular position is unknown and needs to be measured by the sonar. This section delves into the general concept, adapted to the specifics of the ABACUS system, to resolve the angle of arrival of targets in azimuth (horizontal angle). The ABACUS receiver, consisting of two one-dimensional linear arrays, limits the system to being able to resolve only one angular dimension.

Assume a point target is located at long range r at angle θ from the receiver arrays such that $r \ggg L$. L is the dimension of the receive array in the azimuthal plane (along x - axis).

From the geometry depicted in Figure 4.5, it is deduced that all sensors receive the same signal delayed or phase shifted proportionally to -multiples of d, the horizontal separation between two array elements- position of the elements on the x-axis.

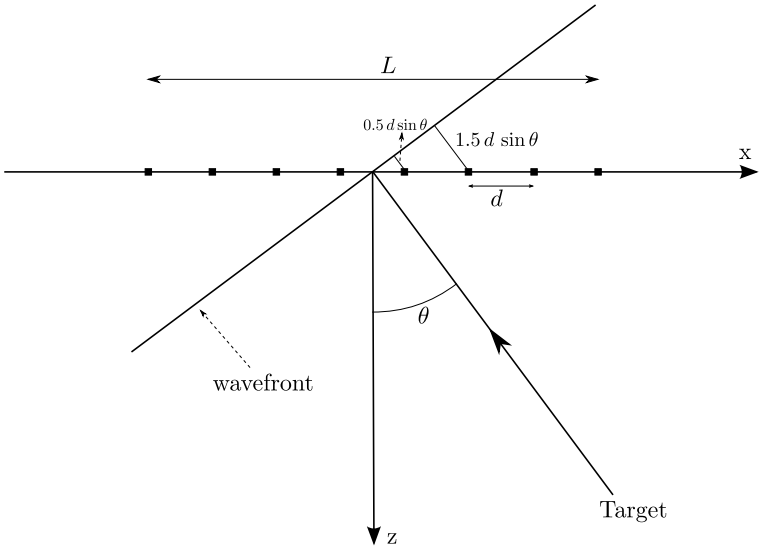

Figure 4.5: Angular reception in azimuth: Geometry

The phase shift and time equivalence only holds true strictly for the centre frequency f_0(of the carrier) or under the narrowband assumption. The narrowband condition is treated in detail in section 4.5.7, and for now it is assumed that the condition is satisfied in the ABACUS system. When the signal occupies a frequency band Δf, the phase shift varies for each frequency component [18]. Referring to our signal model, and the geometry in Figure 4.5, the received signal (after carrier demodulation and pulse compression) at each sensor is:

$$v(t,n) = \gamma_n \frac{1}{|K|}\frac{B}{\pi} Sa\left(\frac{B(t-\tau_n)}{2}\right) e^{-j2\pi f_0 \tau_n} \tag{4.23}$$

where $\gamma_n = \zeta_n e^{j2\pi f_0 \tau_n}$ and τ_n is the two-way propagation delay at each element of the array.

The delay with which the received signal reaches the nth element, relative to the first element is defined as τ_{delay_n}. Thus we have:

$$\tau_n = \tau_{ref} + \tau_{delay_n} \tag{4.24}$$

where τ_{ref} is the two-way propagation delay at the first element. Therefore, Equation 4.23 can be re-written as:

$$\begin{aligned} \nu(t,n) &= \gamma_n \frac{1}{|K|}\frac{B}{\pi} Sa\left(\frac{B(t-\tau_n)}{2}\right) e^{-j2\pi f_0\left(\tau_{ref}+\tau_{delay_n}\right)} \\ \nu(t,n) &= a(t,n) e^{-j2\pi f_0 \tau_{delay_n}} \end{aligned} \tag{4.25}$$

where $a(t,n) = \gamma_n \frac{1}{|K|}\frac{B}{\pi} Sa\left(\frac{B(t-\tau_n)}{2}\right) e^{-j2\pi f_0 \tau_{ref}}$.

As mentioned above, under the narrowband assumption, we can equate the τ_{delay_n} to a

phase shift:

$$\tau_{delay_n} = \frac{2\pi}{\lambda} ndsin\theta \tag{4.26}$$

for $n = [0, N-1]$.

Figure 4.5 depicts the geometry to calculate phase shift at each receiver relative to the first element, as in the ABACUS's system signal model. The phase shift is given relative to the first element.[5]

Thus, the signal at the *nth* sensor can be alternatively given as:

$$\nu(t,n) = a(t,n)e^{-j\frac{2\pi}{\lambda}ndsin\theta} \tag{4.27}$$

for $n = [0, N-1]$.

The term $\frac{2\pi}{\lambda} ndsin\theta$ is the spatial frequency k_θ in cycles at each element [29]. Hence, resolving the target location in azimuth involves processing the signals at each element, at time $t = \tau_n$, based on their spatial frequency content. This is referred to as spatial processing [18].

4.5.1 Digital beamforming

Section 4.1.1 presented the matched filter as a general solution to estimating the parameter (two-way propagation delay) of a signal of known shape, but unknown amplitude and phase, in the presence of white Gaussian noise. This solution can be extended to a function of two variables (time and sensor position on the $x-axis$), so we can estimate the angular location as well. Hence, referring to Equation 4.27, the matched filter (Conventional or Bartlett beamformer)[19] is given as [29] :

$$\begin{aligned} H(\theta,n) &= \left(e^{-j\frac{2\pi}{\lambda}ndsin\theta}\right)^* \\ &= e^{j\frac{2\pi}{\lambda}ndsin\theta} \end{aligned} \tag{4.28}$$

For each θ, the signals at each sensor n, are multiplied by $e^{j\frac{2\pi}{\lambda}ndsin\theta}$ or $e^{j\frac{\omega_0\tau_{delay_n}}{c}}$ and summed in phase at time $t = \tau_n$:

$$\begin{aligned} B(\theta) &= \sum_{n=0}^{N-1} \nu(\tau_n, n)e^{j\frac{2\pi}{\lambda}ndsin\theta} \\ \text{or} \quad B(\theta) &= \sum_{n=0}^{N-1} \nu(\tau_n, n)e^{j\frac{\omega_0\tau_{delay_n}}{c}} \end{aligned} \tag{4.29}$$

[5]The phase shifts are given relative to the first element. However, we use the centre of the array as the reference in the ABACUS system.

This 'beamforming' operation is accomplished in software. The combination of the signals at each sensor with correct adjustments for the phase differences at an angle θ, due to the path differences between elements, is equivalent to steering the beam in the direction of angle θ. In general, in sonar systems, the beam is steered to scan different directions in consecutive steps (angular sample spacing $\Delta\theta$).

Further, the receiver takes into consideration, for a given scanning direction, only the signals coming from this direction [18]. The summation in Equation 4.29 is equivalent to angular filtering around the θ direction.

For a target located at θ_0, the output of the beamformer is given as:

$$B(\theta) = \sum_{n=0}^{N-1} a(\tau_n, n) e^{j\frac{2\pi}{\lambda} nd(sin\theta - sin\theta_0)} \tag{4.30}$$

Setting $a(\tau_n, n) = 1$, restricting our reasoning the analysis to spatial filtering:

$$B(\theta) = \sum_{n=0}^{N-1} e^{j\frac{2\pi}{\lambda} nd(sin\theta - sin\theta_0)} \tag{4.31}$$

Further, Eq 4.31, can be evaluated [5] to :

$$B(\theta) = e^{j(N-1)\pi(\frac{d}{\lambda})(sin\theta - sin\theta_0)} \frac{sin\left[N\pi(d/\lambda)(sin\theta - sin\theta_0)\right]}{sin\left[\pi(d/\lambda)(sin\theta - sin\theta_0)\right]}, \tag{4.32}$$

where $|B(\theta)|$ is the directivity of the phased-array. The antenna pattern of the receiver array is the product of the array directivity and the directivity of a single element, both functions of θ, which from Section 2.2.2, is $\left|sinc\left(\frac{w}{\lambda} sin\theta\right)\right|$, where w is the dimension of the element along the $x - axis$, and

$$sinc\, u = \frac{sin\pi u}{\pi u} \tag{4.33}$$

Therefore, the receiver antenna pattern is given by [5]:

$$|A(\theta)| = \left|sinc\left(\frac{w}{\lambda} sin\theta\right)\right| \times \left|\frac{sin\left[N\pi(d/\lambda)(sin\theta - sin\theta_0)\right]}{sin\left[\pi(d/\lambda)(sin\theta - sin\theta_0)\right]}\right| \tag{4.34}$$

The last term of Equation 4.34 estimates the main lobe of the antenna pattern.

$|A(\theta)|$ is maximum at $\theta = \theta_0$, the target location 4.6, indicating the measurement of angular position of the target in azimuth.

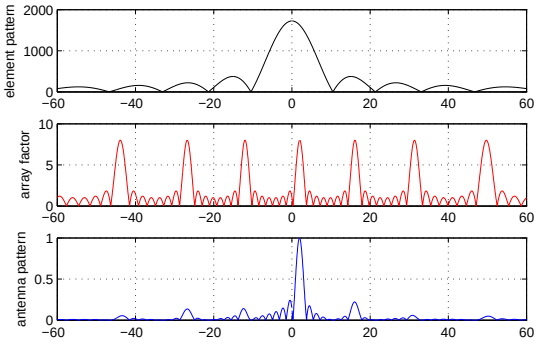

Figure 4.6: The receiver antenna pattern of the ABACUS for a target located at $\theta_0 = 2°$.

4.5.2 Formation of sonar image

To form a 2-D image of the azimuth-range plane of the scene, shown in Figure 4.8, the receive antenna beam is steered to scan several directions in azimuth in steps of $\Delta\theta$, evaluate Equation 4.29 at each range (or time) sampling interval. Mathematically, this is equivalent to evaluating:

$$B(\theta_m) = \sum_{n=0}^{N-1} v(t_i, n) e^{j\frac{2\pi}{\lambda} n sin\theta_m} \tag{4.35}$$

where $-\Theta/2 \leq \theta_m \leq \Theta/2$, Θ is the angular span; m is an integer in the range $[0, M-1]$, with M being the number of scanning directions (beams); and i is an integer in the range $[0, Ns-1]$, where Ns is the number of samples in the range (or time) vector.

The Θ is limited by grating lobes (see Section 4.5.6) and M is chosen such that the angular sample spacing $\Delta\theta = \frac{\Theta}{M-1}$ is small enough to satisfy the Nyquist criterion. Beam steering enables the simultaneous reception of signals from different directions.

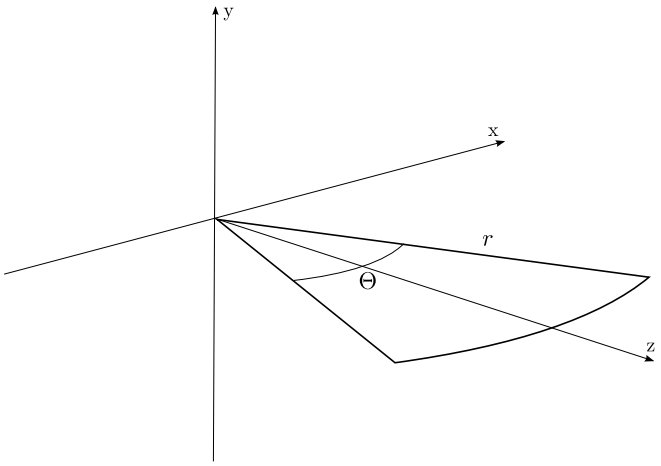

Figure 4.7: Azimuth-range plane of scene scanned

The two linear operations, time and spatial processing, are thus used to form a 2-D image of the scene. The sonar image formed from one of the subarrays, for two targets placed at (spherical) coordinates $\langle 17, 0.7°, 0° \rangle$ and $\langle 21, -1.4°, 0° \rangle$, is displayed in Figure 4.8. The image indicates the azimuth of the two targets.

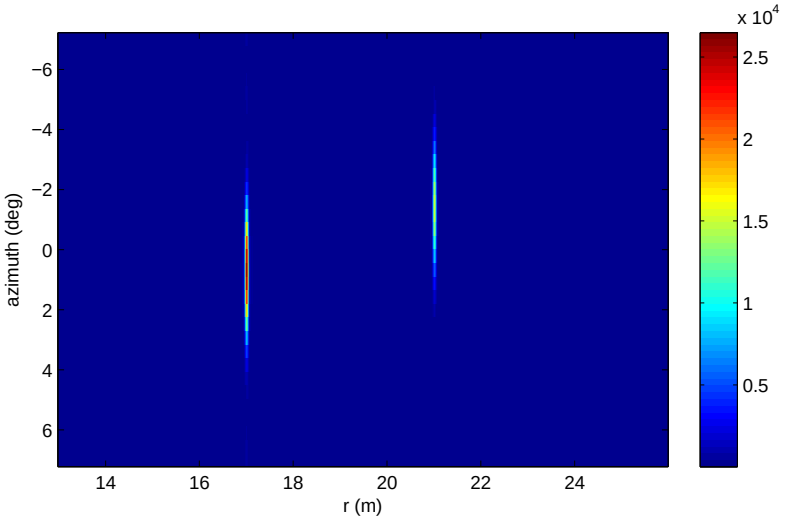

Figure 4.8: Sonar image of the azimuth-range plane of the scene formed from one subarray

4.5.3 Digital Beam Steering/Formation of sonar image implementation by Fast Fourier Transform

From Eq 4.35, scans of M azimuth directions require $M \times N$ operations for each range sampling interval. Therefore $M \times N \times$Ns operations are required for a sonar image [2]. The following describes a much faster computational alternative algorithm. The digital

beamforming operation is similar to the Discrete Fourier Transform (DFT) as can be deduced from Equation 4.37 [26]:

$$X[m] = \sum_{n=0}^{N-1} x[n] e^{-j\frac{2\pi mn}{N}} \quad m \,\epsilon\, [-N/2, N/2-1] \quad \text{DFT} \tag{4.36}$$

$$B(\theta_m) = \sum_{n=0}^{N-1} r(\tau_n, n)\, e^{j\frac{2\pi}{\lambda} nd(sin\theta_m)} \quad m \,\epsilon\, [-N/2, N/2-1] \quad \text{Digital Beamforming} \tag{4.37}$$

Therefore, digital beamforming can be achieved by a Fast Fourier Transform (FFT) across the array, making the following adjustments and substitutions:

$$\begin{aligned} X[m] &\equiv B(\theta_m) \\ \frac{2\pi mn}{N} &= \frac{2\pi}{\lambda} nd(sin\theta_m), \end{aligned} \tag{4.38}$$

such that:

$$\theta_m = sin^{-1}\left(\frac{\lambda}{Nd} m\right) \tag{4.39}$$

The FFT limits the scanning directions to discrete levels defined by Eq 4.39 which are dependent on the variables λ, d, and the number of elements in the array N. This limitation is generally overcome by zero padding the vector across each range bin, ideally by powers of 2 to make use of the radix-2 FFT). The zero padding adds virtual array elements with no data. Equation 4.39 shows that this adds flexibility in the scanning directions and also increases the beam density.

In summary, an FFT of the zero-padded array at each range bin, is equivalent to beamforming at a much faster rate than conventional digital beamforming.

The phase of the image in an angle bin must be consistent with the discussion in Section 4.5.1, which shows that the phase in an angle bin ($\arg\{e^{-j2\pi f_0 \tau_{ref}}\}$) is constant as the data is focussed with respect to the centre of the array. However, the phase at the output of the FFT varies linearly (with spatial frequency). This variation results from the data in the spatial domain being shifted by half the horizontal dimension of the array $\frac{(N-1)d}{2}$, which in the Transform domain (spatial frequency) is equivalent to the Fourier Transform being multiplied by $e^{-j2\pi f_m \frac{(N-1)d}{2}}$, where f_m is the discrete spatial frequency defined as:

$$f_m = \frac{m}{Nd} \quad \text{where } m \,\epsilon\, [-N/2, N/2-1] \tag{4.40}$$

The output of the FFT is multiplied by $e^{j2\pi f_m \frac{(N-1)d}{2}}$ to negate the phase variation in an angle bin.

4.5.4 Angular resolution

The angular resolution $\delta\theta$ of the receive antenna is usually defined, in similar fashion to range resolution, as the smallest angular spacing between two targets such that they can still be resolved. The angular resolution usually corresponds to the 3-dB width of the main lobe of the receive antenna pattern. The receiver antenna pattern of a (continuous) linear array of horizontal dimension L [18] is :

$$|A(\theta)| = \left| sinc\left(\frac{L}{\lambda} sin\theta\right)\right| \tag{4.41}$$

From Eq 4.41, the angular resolution [18] is:

$$\delta\theta = \theta_{3-dB} = sin^{-1}(\frac{\lambda}{L}) \approx \frac{\lambda}{L} \tag{4.42}$$

For ABACUS, the angular resolution[6] is estimated to be:

$$\theta_{3-dB} \approx \frac{\lambda}{L} = \frac{0.00364}{0.12} = 1.74^{\circ} \tag{4.43}$$

4.5.5 Spatial windowing

The antenna pattern is a *sinc* function, therefore has unwanted sidelobes which could potentially mask weak targets that are close to relatively stronger targets in azimuth. Moreover, high sidelobes can be mistakenly interpreted as targets (false detections). As in Section 4.3, an array shading function (Hamming window) is applied to reduce the sidelobes of the antenna pattern. This degrades the angular resolution as the mainlobe of the antenna pattern is widened. Thus, the digital beamforming operation in Eq 4.29 is modified to:

$$B(\theta) = \sum_{n=0}^{N-1} w(n)\nu(\tau_n, n)\, e^{j\frac{2\pi}{\lambda} nd(sin\theta)} \tag{4.44}$$

4.5.6 Spatial Sampling

The previous section discussed the spatial processing of the received signals by the receive antenna array. This implies that the sensors "sample" the signal received by the array. The sampling rate must exceed the spatial Nyquist rate [39]:

$$d \leq \frac{\lambda}{2} \tag{4.45}$$

[6]This is with only half the length of the array (eight elements used)

Grating lobe ambiguities

The disadvantage of a phased array antenna compared to a continuous antenna of the same dimension is the grating lobe effect. If the receiver antenna elements are not spaced at $d < \frac{\lambda}{2}$, the antenna pattern has other principal maxima (grating lobes) in addition to its main lobe. The grating lobes cause targets outside the scene to appear in the sonar image formed, as ghost images. Moreover, the grating lobes limit the angular span of the scene. In the case of ABACUS where the spatial sampling criterion is not satisfied ($d = 0.015$ m is greater than $\frac{\lambda}{2}$= 0.00182), and referring to the last term of Equation 4.32 (dirichlet function in $\sin\theta$), the grating lobes [5] occur at:

$$\left(\frac{d}{\lambda} sin\theta_{gl}\right) = p$$

$$\theta_{gl} = sin^{-1}\left(\frac{p\lambda}{d}\right), \tag{4.46}$$

where p is an integer. In ABACUS, the first grating lobe appears at $\theta_{gl} = 14°$(Figure 4.9). Additionally grating lobes occur at angles that cause the phase between two adjacent elements to be ambiguous.

$$\frac{2\pi}{\lambda} dsin\theta_{gl} = 2\pi p$$

$$\theta_{gl} = sin^{-1}\left(\frac{p\lambda}{d}\right) \tag{4.47}$$

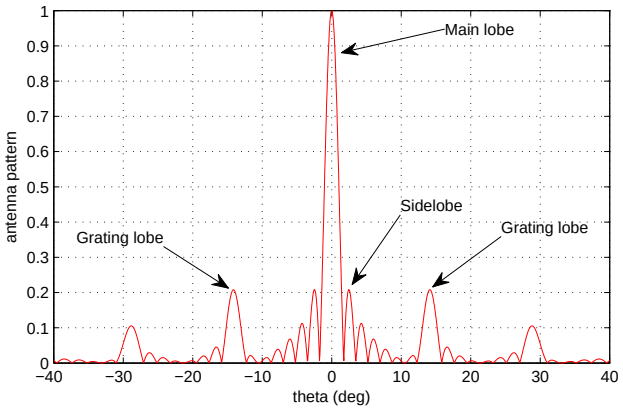

Figure 4.9: The receiver antenna pattern of ABACUS

For a forward looking array (ABACUS), the scanning span must be limited to $\Theta = \theta_{gl}$ and thus scan only between the directions $(-\Theta/2, \Theta/2)$. This is because for a target located at range r and azimuth location $\theta_0 = \frac{-\theta_{gl}}{2}$, there will be a ghost target at $\left(r, \frac{+\theta_{gl}}{2}\right)$ in the

sonar image, as the received signals at two adjacent elements will have a phase difference of π.

Figure 4.10 shows a ghost target at $\langle 17, 7° \rangle$ for a target located at $\langle 17, -7° \rangle$. For ABACUS, $\frac{\theta_{gl}}{2} = 7°$.

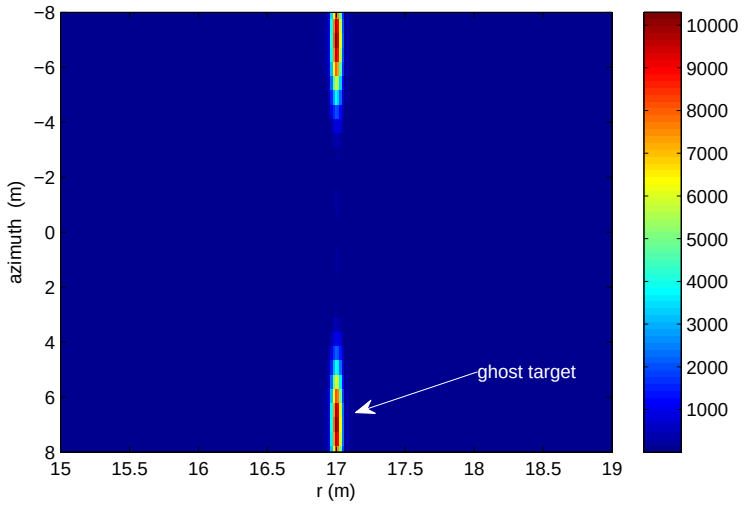

Figure 4.10: Sonar image showing ghost target

Another problem is that targets located at $\theta = \theta_0 \pm \theta_{gl}$, outside the scanning span, will appear at θ_0 in the sonar image. Assume that θ_0 lies in the range $(-\Theta/2, \Theta/2)$. If $\theta_0 = 1°$, such that a target is placed at $\theta = 1° + 14° = 15°$, $\langle 17, 15° \rangle$ a ghost target appears at $\langle 17, 1° \rangle$ as shown in Figure 4.11. The brightness of the ghost target is relatively low, since the target is outside the transmitted beam in azimuth.

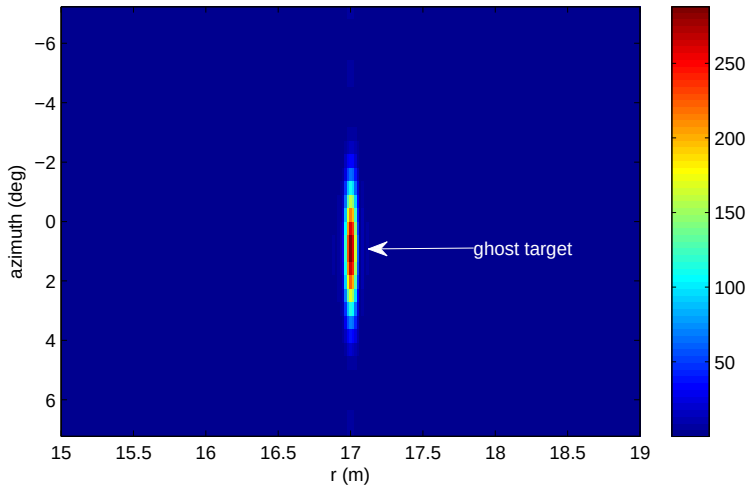

Figure 4.11: Sonar image showing ghost target at $\langle 17, 1° \rangle$, for a target placed at $\langle 17, 15° \rangle$

Therefore, it is essential for the transmitter not to insonify outside the range $(-\Theta/2, \Theta/2)$. Referring to Table 3.2, we see that the ABACUS does not insonify outside the aforementioned range.

4.5.7 Simplifying assumptions in digital beamforming for the ABACUS system

Narrowband assumption

The equivalence of time delay and phase shift is assumed at the array elements (Section 4.5). This is only true,strictly, at the centre frequency f_0 of the carrier. For a given time delay, the phase shift varies over the frequency band (bandwidth) Δf from one frequency component to the other. The phase variation is given [18] as:

$$\Delta\varphi = 2\pi\frac{\Delta f}{c}dsin\theta \tag{4.48}$$

Literature [16, 18] suggests that the narrowband criterion is satisfied if the phase variation, $\Delta\varphi \ll 2\pi$ for the extreme case $Lsin(90^0)$, that is over the antenna dimension and at the maximum possible angle of arrival. This condition is [18]:

$$\frac{\Delta f}{f} \ll \frac{\lambda}{L} \tag{4.49}$$

$\frac{\Delta f}{f}$ is referred to as the fractional bandwidth. For ABACUS, $\frac{\Delta f}{f} = \frac{20}{420.375} = 0.0475 \not\ll \frac{\lambda}{L} = 0.0307$. Yet, if the maximum scanning direction is limited to 7^0, then $\frac{\Delta f}{f} = \frac{20}{420.375} = 0.0475 \ll \frac{\lambda}{Lsin(7^0)} = 0.252$. Therefore, digital beamforming is justified under narrowband assumption for ABACUS.

Far-field assumption

Assume that the acoustic waves impinging on the receive array are planar, as displayed in Figure 4.12. In other words, the echo signal from a point target radiates spherically until the wavefronts are essentially planar, i.e array dimension $L \ll$ radius of propagation. For plane waves, the time delays or phase shifts between array elements are independent of range.

The plane wave assumption is valid at ranges larger than the Rayleigh distance [31]:

$$R_f = \frac{2L^2}{\lambda} \tag{4.50}$$

For ABACUS, $R_f = \frac{2\left(\frac{0.237}{2}\right)^2}{0.00364} = 7.72$ m. ABACUS' receiver is only valid for targets in the range exceeding 11m. Therefore, the plane wave approximation is valid for ABACUS.

Figure 4.12: Receive array in far field [31]

Propagation assumptions

Within the operating region of the sonar, the propagation medium is modeled as homogeneous and non-dispersive. Assuming acoustic waves in seawater are non dispersive, $k = 2\pi/\lambda$ for all frequencies (hence, all signal frequencies travel at the same speed). Further, the medium being homogeneous means that we are disregarding any change in the velocity of the acoustic signals with temperature, salinity and pressure (depth). Therefore, we assume a uniform propagation in all directions with constant speed $c = 1,500\text{m} \times s^{-1}$.

Noise correlation

Assumed the zero mean white noise and signals are uncorrelated at each channel [36]. Therefore, digital beamforming, effectively coherent integration, increases the signal-to-noise ratio by a factor N, the number of receive elements.

4.5.8 Wideband situations

There are two approaches to digital beamforming in situations where relatively wide bandwidths are used:

1. The angular analysis is performed by using time delays rather than phase shifts [18].
2. Transform the received time signals at each channel to the frequency domain (Fourier Transform) to generate narrowband components (subbands). Then, narrowband spatial analysis is performed on each subband. Eventually, the subbands are coherently summed (Inverse Fourier Transform) to recover the time signal for each direction [1, 18].

Detailed explanations on efficient, frequency domain algorithms to perform beamforming on digital signals from a linear array of elements are given in [21, 11]. [7] treats the implementation of a wideband beamforming technique using time delays. Further, [1] outlines the time domain beamforming implementation by a time delay network, to bring the signals in phase, between the receiver elements and the coherent summation of signals for each scan direction.

4.6 Display

The 2-dimensional images formed are a function of the range and azimuth location of the targets, and defined $I(r, \theta)$. Digital beamforming in azimuth was performed in the plane defined by $\phi = 0°$. The images are then translated to be a function of the Cartesian coordinates (x,z) of the targets, similarly defined as $I(x, y)$, where -z defines the depth. Since $\phi = 0°$:

$$\begin{cases} x = rsin\theta \\ z = rcos\theta \end{cases} \tag{4.51}$$

Hence, the resolutions in the transverse and radial directions are given as:

$$\begin{cases} \delta x = \delta rsin\delta\theta \\ \delta z = \delta rcos\delta\theta \end{cases} \tag{4.52}$$

Therefore, the sampling intervals in the transverse and radial directions of the image $I(x, y)$ need to be much smaller than the resolutions defined in Equation 4.52 to satisfy Nyquist criterion. Thus, because the sampling intervals in image $I(x, y)$ are smaller than those in the image $I(r, \theta)$, the data needs to be interpolated. A bi-linear interpolation function (MATLAB) is used. A fan beam image shows the Cartesian coordinates of the targets in the horizontal plane of the scene (Figure 4.13).

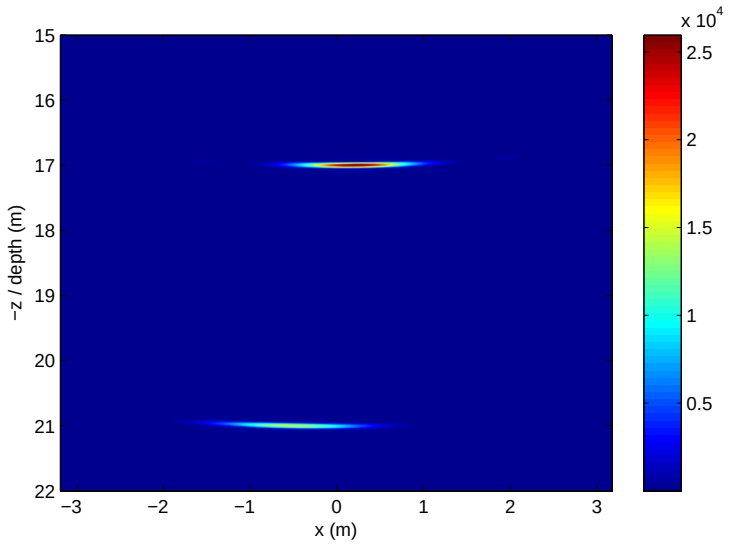

Figure 4.13: Fan beam (Cartesian) image formed from one of the subarrays

4.7 Phase Interferometry

Pulse compression and digital beamforming enables the formation of high resolution images from the two receiver subarrays. The 2-dimensional images of the scene show the horizontal angle and range of the possible targets. Digital beamforming in elevation results in very low resolution $\delta\phi = \frac{\lambda}{L_v} = \frac{0.00364}{0.0241} = 8.65°$, because the vertical dimension (L_v) of the receiver is small (only two elements). Phase interferometry methods can be used to estimate the elevation angles [30].

4.7.1 Introduction

Phase interferometry method is used in interferometric synthetic-aperture radar (IFSAR) to generate digital terrain elevation maps. A pair of high resolution images formed from two subarrays or apertures are used for that purpose.

4.7.2 Measuring Elevation angle of arrival

To relate the phase measurements to the elevation angle of arrival, equations are derived from the geometry of ABACUS (Fig 4.14).

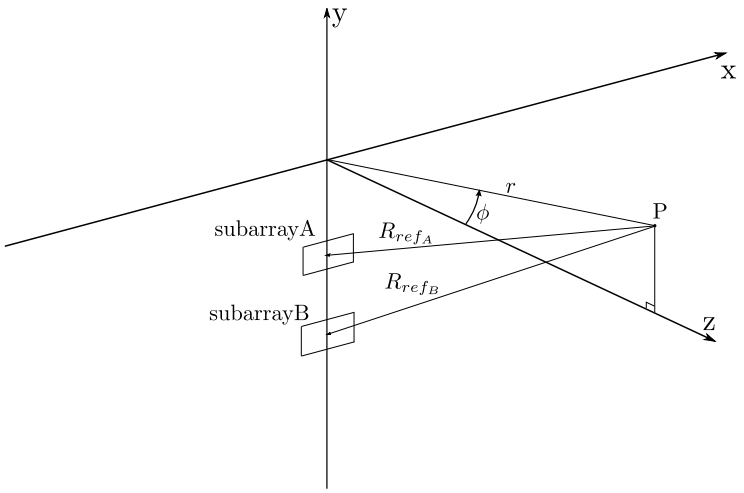

Figure 4.14: Geometry for estimating phase difference between signals at ABACUS subarrays

Basic interferometric multibeam sonar relationship

The signal processing steps so far have output two complex valued two-dimensional images (both amplitude and phase for a pixel) from the receiver subarrays. Considering the phase in an image cell with a peak that has resulted from a single point target scatterer at an arbitrary location (r, θ).

The signals at each sensor were summed in phase and focused with respect to the centre of the receiver subarray. Hence, the cell in the image formed is:

$$I(r,\theta) = \sum_{n=0}^{N-1} c(\tau_n, n) e^{-j2\pi f_0 \tau_{ref}} \tag{4.53}$$

where $C(\tau_n, n)$ is the real-valued amplitude of the data at each sensor, at $t = \tau_n$.

τ_{ref} is the two-way propagation delay (time for a signal to travel from the transmitter to the point target and the echo signal to reach the phase centre of the subarray). The phase of the pixel or cell in the image at the location of the, point target, peak will then be:

$$\begin{aligned} \psi(r,\theta) &= arg\{I(r,\theta)\} \\ &= -2\pi f_0 \tau_{ref} \end{aligned} \tag{4.54}$$

Define the cells in the two complex images where the peak is located as:

$$\begin{aligned} I_A(r,\theta) &= \sum_{n=0}^{N-1} C_A(\tau_n, n) e^{-j2\pi f_0 \tau_{ref_A}} \quad \text{image formed from subarray A} \\ I_B(r,\theta) &= \sum_{n=0}^{N-1} C_B(\tau_n, n) e^{-j2\pi f_0 \tau_{ref_B}} \quad \text{image formed from subarray B} \end{aligned}$$

The difference in phase at the centre of the two subarrays is, using Equation 4.54:

$$\psi_{AB}(r,\theta) = \psi_A(r,\theta) - \psi_B(r,\theta) = -2\pi f_0 \left(\tau_{ref_A} - \tau_{ref_B}\right) \tag{4.55}$$

where $\psi_{AB}(r,\theta)$ is referred to as the interferometric phase difference (IPD).

Equation 4.55 can be re-written as a function of path length difference from the point target to the two subarrays. Referring to Figure 4.14:

$$\begin{aligned} \psi_{AB}(r,\theta) &= -2\pi f_0 \left(\tau_{ref_A} - \tau_{ref_B}\right) \\ &= -2\pi f_0 \left(\frac{r + R_{ref_A}}{c} - \frac{r + R_{ref_B}}{c}\right) \\ &= -2\pi f_0 \left(\frac{R_{ref_A}}{c} - \frac{R_{ref_B}}{c}\right) \\ &= -2\pi f_0 \left(\frac{\delta r}{c}\right) \\ &= -\frac{2\pi}{\lambda}\delta r \end{aligned} \tag{4.56}$$

where $\delta r = R_{ref_A} - R_{ref_B}$ is the path length difference.

Effect of elevation angle of arrival on phase difference

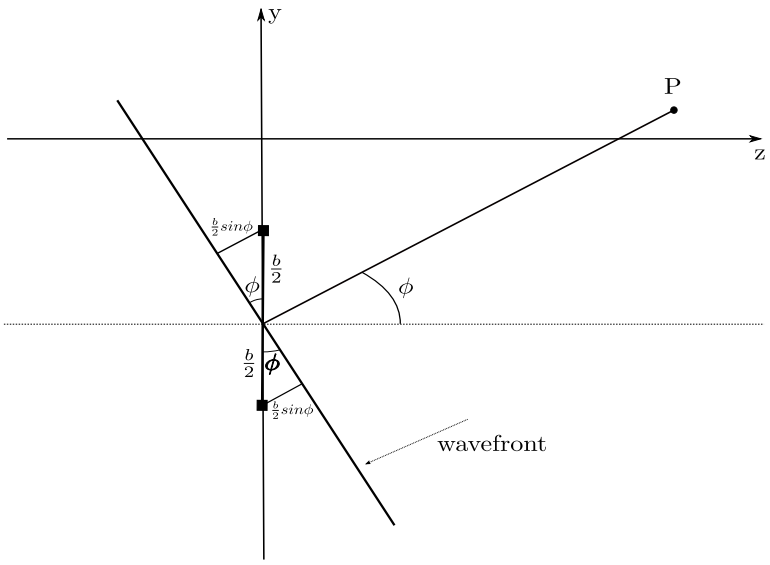

Figure 4.15: Angular reception in elevation

From further geometrical consideration using Fig 4.15:

$$\delta r = 2\left(\frac{b}{2}\right) sin\phi = bsin\phi \tag{4.57}$$

Hence, a change in angular elevation results in a change in phase difference. In other words, phase difference is a function of angular elevation.

$$\psi_{AB}(r,\theta) = -\frac{2\pi}{\lambda}\delta r = -\frac{2\pi}{\lambda}bsin\phi \tag{4.58}$$

Therefore, the elevation angle of arrival can be derived from Equation 4.58:

$$\phi = arcsin\left(\frac{-\psi_{AB}(r,\theta)\lambda}{2\pi b}\right) \tag{4.59}$$

Measuring interferometric phase difference

The interferometric phase difference is measured in the MATLAB package by computing the interferogram:

$$I_{AB}(r,\theta) = I_A(r,\theta)I_B^*(r,\theta) \tag{4.60}$$

Hence,

$$\begin{aligned} arg\{I_{AB}(r,\theta)\} &= \psi_A(r,\theta) - \psi_B(r,\theta) \\ &= \psi_{AB}(r,\theta) \end{aligned} \tag{4.61}$$

The phase of the pixels or cells in an image will, in general, be many radians since the range will be many multiples of the carrier wavelength. The phase is:

$$\psi_A = 2\pi k_A + \tilde{\psi_A} \tag{4.62}$$

where k_A is an integer and $\tilde{\psi_A}$ is the principal value of ψ_A and lies in the range $[-\pi, \pi]$. In fact, the coherent receiver measures the principal value as it calculates the argument of the phasor:

$$\tilde{\psi_A} = arctan(\frac{Q}{I}) \tag{4.63}$$

where Q and I are the in-phase and quadrature components of the phasor. Therefore, computing the interferogram and taking its argument is effectively the phase subtraction of the wrapped phases $\tilde{\psi_A} - \tilde{\psi_B}$ of the cells in the two images:

$$\begin{aligned} \tilde{\psi_A} - \tilde{\psi_B} &= \psi_A - 2\pi k_A - \psi_B + 2\pi k_B \\ &= \psi_A - \psi_B + 2\pi(k_B - k_A) \end{aligned} \tag{4.64}$$

A wrapping operator $W[]$ (Matlab) does this by:

$$\begin{aligned} W\left[\tilde{\psi_A} - \tilde{\psi_B}\right] &= W\left[\psi_A - \psi_B + 2\pi(k_B - k_A)\right] \\ &= W\left[\psi_A - \psi_B\right] \\ &= \tilde{\psi_{AB}} \end{aligned} \tag{4.65}$$

The Interferometric Phase Difference data obtained by phase subtraction of the two sonar images formed, for the two targets at (spherical) coordinates $\langle 17, 0.7°, 0° \rangle$ and $\langle 21, -1.4°, 0° \rangle$ is displayed in Figure 4.16.

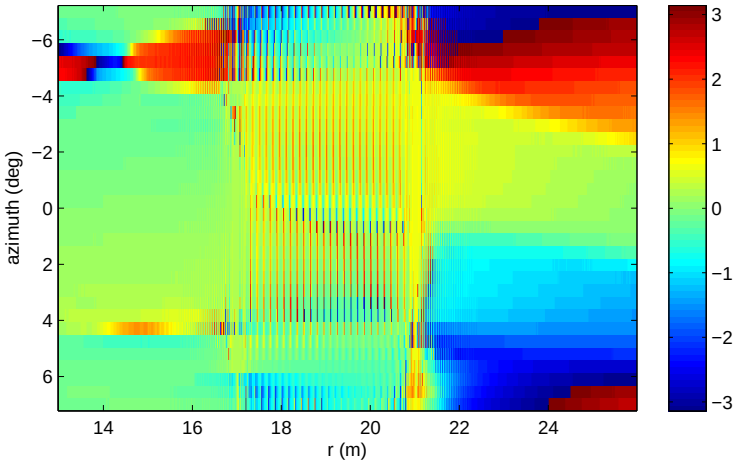

Figure 4.16: Wrapped interferometric phase data $\tilde{\psi_{AB}}$.

The problem of phase unwrapping (for ψ_{AB}) is not an issue in the ABACUS because for the phase to jump (wrap), the phase difference would have to be equal to π radians. This would imply that:

$$\begin{aligned} -\frac{2\pi}{\lambda} bsin\phi &= \pi \\ \phi &= arcsin\left(\frac{\lambda}{2b}\right) \end{aligned} \tag{4.66}$$

For ABACUS , this is the case when $\phi = arcsin\left(\frac{0.00364}{2\times 0.0241}\right) = 4.33°$. The 10 dB beamwidth of the transmitted beam of the ABACUS in elevation $\sim 1.47°$. This suggests that targets with elevation angles beyond the range $(-0.74, 0.74)$ will not appear in the sonar images formed, or will not produce bright peaks, thus mitigating the issue of phase wrapping.

Assumption

The discussion so far indicates that the elevation angle can be computed for a target declared present in the 2-dimensional image formed. This assumes that there is only one target in one azimuth-range cell, since the technique of interferometry is incapable of discriminating multiple targets from different elevation angle of arrivals, but with same azimuth and range positions.

Chapter 5

Target detection and counting

5.0.3 Problem statement

The signal processing steps in the previous sections have generated an image of the observed scene in the azimuth-range (horizontal) plane. The sonar image is comprised of azimuth-range cells with *sinc* functions peaks located at the positions of possible targets. The brightness of the peaks in the sonar image varies with parameters of the targets such as: the angular location of the target $\langle \theta, \phi \rangle$ in the volume insonified by the transmitted beam, the range r, and sonar target strength. The responses are characterised with more-or-less bright secondary maxima (sidelobes). The sonar images are also contaminated by noise. Moreover, there is also the possibility of weak ghost targets appearing in the sonar images.

The problem is to judge if the peaks are from targets or noise, and to estimate the number of targets in the sonar images. A algorithm to detect peaks in the sonar image was established. Next is a brief overview of detection theory, and a sensitivity analysis to estimate a threshold to ascribe peaks to targets and noise.

5.1 Peak detection using the zero crossing of the first derivative

Two-dimensional images of the scene in the azimuth-range plane depicts peaks located at the positions of possible targets. The peaks due to point targets are bright with secondary maxima. The aim is to find the peaks in the sonar image using the zero-crossing of the first derivative of the image [24]. For a positive peak, the first derivative changes from

positive to negative, crossing zero at the position of the peak. The gradient at each azimuth-range cell in the sonar image is given by:

$$\nabla I(r,\theta) = \frac{\partial I(r,\theta)}{\partial r}\hat{r} + \frac{\partial I(r,\theta)}{\partial \theta}\hat{\theta} \tag{5.1}$$

A peak is present at an azimuth-range cell if the gradient is zero:

$$\nabla I(r,\theta) = 0 \tag{5.2}$$

The peak detection algorithm is limited by the bright secondary maxima and noise in the sonar image. Those are rejected using a threshold. Target peaks exceed a set threshold.

5.2 Detection theory and threshold determination

Detection problem

As mentioned in Section 5.1, we need to set a threshold to determine whether the peaks detected resulted from the presence of targets (signal + noise) or from noise alone. The aim is to ensure that we correctly determine what causes the peak, as often as possible. In radar and sonar systems, the detection decision can be applied at any of the stages of signal or data processing. In ABACUS system, the 2-D sonar images $I(r,\theta)$ are tested for the presence of a target at each azimuth-range cell [18].

5.2.1 Statistical Hypothesis

Statistical signal models are used to characterise noise and the received signal echoes in radar and sonar systems. Therefore, the detection problem is a choice between two hypotheses based on the levels (brightnesses) of the peaks detected in the sonar image [18]:

H_1 : the peak is a result of signal + noise

H_0 : the peak is a result of noise only

In practice, the probability of the errors that can be made is the criterion to select one of the two hypotheses. The two errors are:

1. Deciding that there is a target (H_1) when only noise is present (H_0) (false alarm).

2. Deciding there is no target (H_0), when there actually is one (H_1) (non detection).

The hypotheses and errors are summarised in a binary decision table 5.1 indicating probabilities associated with each of the decisions.

	signal+noise (H_1)	*noise* (H_0)
signal	detection (P_d)	non detection ($1 - P_d$)
noise	false alarm (P_{fa})	miss ($1 - P_{fa}$)

Table 5.1: Binary decision table

The detection problem is based on a statistical description of the probability distribution functions of the noise, and signal plus noise. The false alarm probability is specified.[1] Then, according to the Neyman Pearson criterion, the detection probability is maximised:

$$\begin{cases} P_{fa} = & \alpha \\ Max & P_d \end{cases} \tag{5.3}$$

This leads to a likelihood ratio test, where a threshold T validates one of the two hypotheses.

The pdfs of the received signal and noise must be characterised to perform the likelihood ratio test to maximise the P_d for a set P_{fa}. For ABACUS, it is not possible to characterize the pdf of the signal prior to detection. The pdf of the received echo signals depends on the range, bearing, and sonar target strength of the targets [30]. Some of those parameters i.e., sonar target strength and elevation angle are unknown prior to detection . Moreover, the sonar target strength, modeled as a random variable, fluctuates.[2] Hence, we are unable to apply the maximum likelihood test to estimate a threshold that maximises the P_d for a specified P_{fa}. The noise statistics to restrict the false alarm probability to a set value, without maximising the probability of detection P_d [15].

5.2.2 Optimising the threshold

The detection problem in ABACUS is therefore solved by setting a reasonable false alarm probability that is not to be exceeded for a sonar image ($P_{fa} \leq 10^{-7}$). Since the thresholding decision is to be performed on each cell of the image, the P_{fa} is calculated for each azimuth-range cell of the sonar image under test. Using the noise statistics, a threshold is identified that satisfies the false alarm limit set.

The level of noise is assumed to be constant. In the case of the noise level varying over time (pings), an adaptive threshold detection must be be implemented (CFAR- Continuous

[1] A false alarm probability P_{fa}, acceptable for the specific situation, is set.
[2] We note that it is possible to do so for the ABACUS simulator.

False Alarm Rate detection) as suggested in [18, 29]. Varying noise precludes the use of a threshold estimated a priori.

5.2.3 Noise model (probabilistic model)

Estimate of noise level in ABACUS simulator

The noise was modelled as bandlimited (bandwidth of receivers), white, with normal distribution, as detailed in Section 2.4.2. The envelope of the sum of two quadrature components (in a coherent system such as ABACUS), with Gaussian distribution, obeys a Rayleigh distribution. Hence, the noise in the sonar images follows a Rayleigh distribution. This is verified in the ABACUS simulator by estimating the noise levels in the azimuth-range cells of an image in which there are no targets. The mean value of the noise levels is thus obtained.

Estimate of noise level in sonar images formed from real data

In the processing of real data, the noise level is estimated from regions in a sonar image where there are no targets present. It is postulated that the statistics of the noise estimated from the real data fits the noise model (i.e., Rayleigh pdf at the point of detection).

It is assumed that the noise level does not vary over pings.

5.2.4 P_{fa} for each azimuth-range cell

A reasonable false alarm probability is to be specified for a sonar image. From that, the false alarm probability for each azimuth-range cell is derived. The false alarm probability for each cell is calculated to be:

$$P_{fa_{cell}} = 1 - \left(P_{fa_{image}}\right)^{\frac{1}{N_{cells}}} \tag{5.4}$$

5.2.5 Threshold calculation

From Section 5.2.1, a false alarm is the error when deciding that there is a target (selecting hypothesis H_1) when only noise is present (H_0). Therefore, the false alarm probability can be defined as:

$$P_{fa} = \int_T^\infty P_{x/H_0}(x)\, dx \tag{5.5}$$

where T is the threshold and $P_{x/H_0}(x)$ is the probability density of x (where x represents noise) given that only noise is present (H_0).

Hence, from the definition of a cumulative distribution function $F_X(x)$:

$$F_X(T) = \int_{-\infty}^{T} P_{x/H_0}(x)dx \tag{5.6}$$

we deduce that:

$$P_{fa_{cell}} = 1 - F_X(T) \tag{5.7}$$

The above result allows the threshold to be estimated for a required false alarm probability, when the noise statistics are known.

For the case when the noise obeys a Rayleigh distribution (ABACUS):

$$P_{fa_{cell}} = e^{-T^2/2\sigma^2} \tag{5.8}$$

where σ is the standard deviation of the Rayleigh pdf.

Equation 5.8 indicates that the threshold T, not to exceed a specified $P_{fa_{cell}}$, is:

$$T \geq \sqrt{-2\mu^2 \left(\frac{\pi}{2}\right) \ln\left(P_{fa_{cell}}\right)} \tag{5.9}$$

where $\mu = \sigma\sqrt{\frac{\pi}{2}}$.

We compare the brightness level of each cell of the image where a peak is detected to the above threshold and declare a target present if the threshold is exceeded.

$$I(r, \theta) \gtrless T \tag{5.10}$$

5.3 Target Location in 3D

5.3.1 Problem definition

The aim of the project is to estimate the number of targets in a volume, the fish aggregations. We have treated the detection of targets in the sonar images which depict the azimuth-range (horizontal) plane of the scene. The 3-D locations of the detected targets indicate whether they are in the pre-defined counting volumes (For ABACUS, the counting volume's boundaries are defined by the 3-dB beamwidths of the transmitted beam). The estimated ranges and azimuths of the targets detected, and interferometric phases at those coordinates, indicate the 3-D locations of the targets detected.

The 3-D geometry of ABACUS is incorporated into a set of equations including the measured parameters. The solutions to the system of equations are the 3-D location of the targets detected [41].

5.3.2 Vector geometry of ABACUS

The geometry of ABACUS for the 3-D vector analysis is depicted in Figure 5.1.

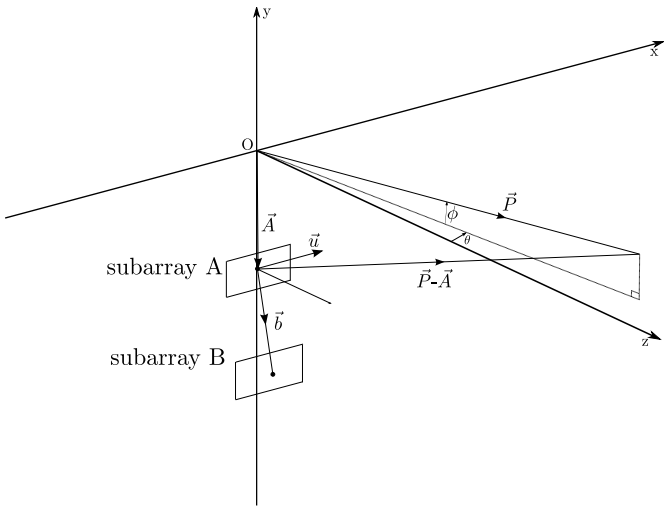

Figure 5.1: 3-D vector geometry of ABACUS

Figure 5.1 depicts a point target in the frame of ABACUS. The system components and the point target are defined by vectors in Cartesian coordinates, relative to the origin. Referring to the vector diagram:

$\vec{P} = \langle x, y, z \rangle$ defines the location of the point target scatterer;

$\vec{A}$ defines the location of the phase centre of receiver subarray A;

$\vec{P} - \vec{A}$ defines the vector from the phase centre of subarray A to the point target; and

the baseline vector $\vec{b}$ is the vector from the phase centre of receive subarray A to subarray B.

$\vec{u}$ is a unit vector along the x axis.

5.3.3 System of vector equations

Inspecting the geometry and considering the parameters measured (range r, azimuth angle θ, and IPD ψ_{AB}), the following set of equations are derived:

1. Performing a scalar projection (scalar product) of vector $\vec{P} - \vec{A}$ onto the x-z plane (horizontal plane) :

$$\left(\vec{P} - \vec{A}\right) \cdot \vec{u} = \left|\left(\vec{P} - \vec{A}\right)\right| |\vec{u}| \, cos(\frac{\pi}{2} - \theta) \tag{5.11}$$

where θ is the azimuth location. This is verified in the Figure 5.2.

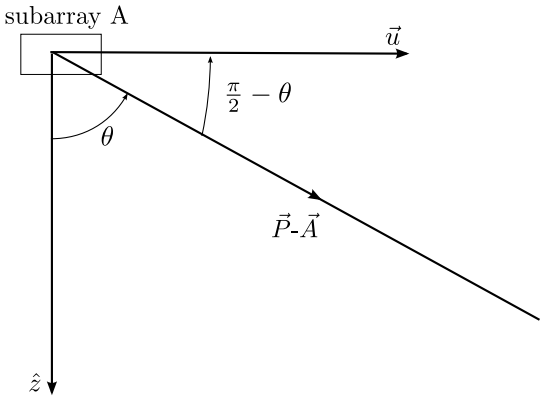

Figure 5.2: Scalar projection on horizontal plane

2. Similarly, a scalar product of the vector $\vec{P} - \vec{A}$ and the baseline vector $\vec{b}$ gives the equation:

$$\begin{aligned} \left(\vec{P} - \vec{A}\right) \cdot \vec{b} &= \left|\left(\vec{P} - \vec{A}\right)\right| \left|\vec{b}\right| cos(\frac{\pi}{2} - \phi) \\ &= \left|\left(\vec{P} - \vec{A}\right)\right| \left|\vec{b}\right| sin\phi \end{aligned} \tag{5.12}$$

where ϕ is the elevation angle of arrival. Referring to Figure 5.1, the baseline vector is -slightly offset as a result of the receive subarray B being offset in the horizontal direction- not exactly aligned with the (negative) y-axis. The offset is not significant, therefore the scalar product in Equation 5.12 is still valid. This is depicted in Figure 5.3

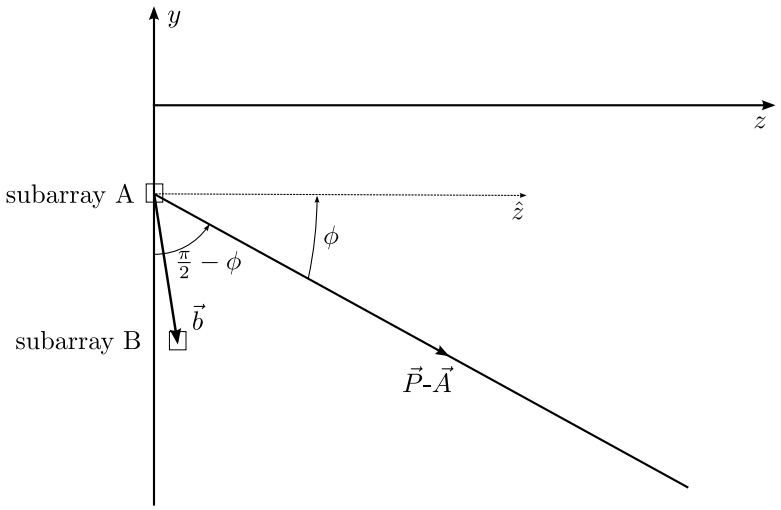

Figure 5.3: Scalar projection on vertical plane

From Section 4.7:

$$\psi_{AB} = -2\pi \frac{\left|\vec{b}\right| sin\phi}{\lambda}$$

Therefore, Equation 5.12 can be simplified to:

$$\left(\vec{P} - \vec{A}\right) \cdot \vec{b} = \left|\left(\vec{P} - \vec{A}\right)\right| \left|\vec{b}\right| \left(-\frac{\psi_{AB}\lambda}{2\pi}\right) \tag{5.13}$$

3. The vector diagram in Figure 5.1 shows that the two-way propagation delay (relative to subarray A) can be defined in terms of vectors as:

$$\tau = \frac{\left|\vec{P}\right| + \left|\left(\vec{P} - \vec{A}\right)\right|}{c} \tag{5.14}$$

5.3.4 Solutions of location of simultaneous equations

The system of three equations can be solved for the three unknowns $\langle x, y, z \rangle$, the Cartesian coordinates indicating the position of the point target scatterer (defined by vector $\vec{P}$). The solutions to the set of equations are computed by the *solve* function in the (Matlab,*Symbolic Maths Toolbox*), but could be solved by an analytical solution (beyond the scope of this dissertation).

5.3.5 Accuracy of solutions

The two-dimensional sonar images and interferograms are rectangular grids of pixels defined at discrete sampling intervals Δr in range and $\Delta\theta$ in azimuth. Hence, the accuracy

of the coordinates used to solve the system of equations is limited to the nearest Δr and $\Delta\theta$ intervals. This error can be reduced by interpolating (zero padding in frequency domain) the images, thus making the sampling intervals finer.

Chapter 6

System performance

The previous sections pertained to the detection of targets in the sonar images, formed from synthetic data obtained from the ABACUS simulator. Now assessed is the performance of the system in detecting, locating, and counting targets, in relation to parameters such as target position, sonar target strength and noise level in the underwater environment.

The system's performance systematically: first testing the performance of the counting algorithm; then assessing the counting system against each of the variables: target position, sonar target strength and noise level. Studied also are the limitations of the ABACUS system. The mainlobe to sidelobe ratio of the response from the point target in a sonar image is examined as high sidelobes levels of the response can be a potential source of false alarms. Further, the occurrence of ghost targets in the sonar images are examined.

The assessment of the system is then used to estimate target densities from pelagic survey data.

It is noted that a sequence of images obtained from simulated data are shown in Appendix B. Further, the targets detected in the sonar images are highlighted to illustrate how the counting system works. Moreover, the 3-D locations of the detected targets, along with the other targets simulated, are also depicted. Further, in Appendix C, fan beam images obtained from processing real data are shown. Along with those images, the location of the detected targets are shown from different perspectives to illustrate how target counts in a volume are obtained.

6.1 Limitations

6.1.1 Sidelobe levels

The secondary maxima of the response from a point target can be a cause of false alarms. The sidelobe characteristics of the ABACUS system (Figures 6.1) show the response from a point target located at $\langle 19.5, 0, 0 \rangle$.

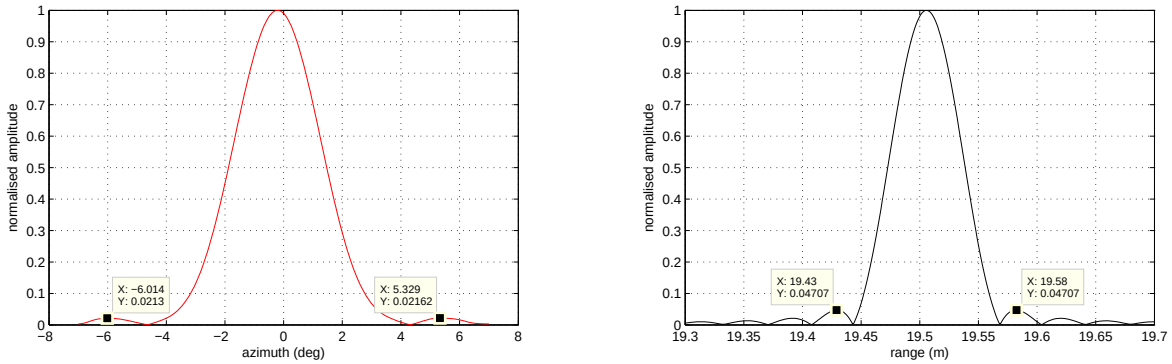

(a) Point target response in azimuth

(b) Point target response in elevation

Figure 6.1: Point target response of ABACUS

It is noted that the mainlobe to sidelobe ratio is $\simeq 0.02$ in azimuth and $\simeq 0.05$ in range.

6.1.2 Grating lobe ambiguities (ghost targets)

Additional ghost targets can be present in the sonar images because: the vertical staggering of the ABACUS receiver elements effectively causes a subarray to behave as two subarrays, with each element a horizontal distance $2d$ apart. Referring to Section 4.5.6, there are grating lobes at:

$$\theta'_{gl} = \arcsin\left(\frac{\lambda}{2d}\right) = 6.97^\circ \tag{6.1}$$

Thus, the target offset from boresight in elevation, causes a phase difference between the signal at the "two subarrays" resulting in ghost targets. This phenomenon was investigated in the study of the image formed for a target located at $\langle 24, 3.5^\circ, 1.0^\circ \rangle$.

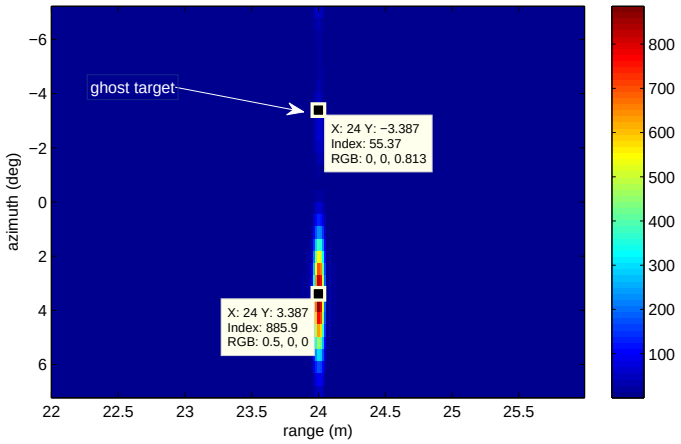

Figure 6.2: Ghost target produced at $\langle 24, -3.4° \rangle$

The claim is verified as a ghost target is present at $\langle 24, -3.4° \rangle$ in the sonar image. The brightness of the ghost target is relatively small compared to the brightness of the peak due to the actual target. Further, displacing a target off boresight in elevation moves it out of the transmitter beam, therefore mitigating the ghost target occurrence.

6.1.3 Noise level

6.2 Simulator parameters

An arbitrary number (100) of pings was simulated. The counting volume's boundaries were defined by the transmitter's 3 dB beamwidths in azimuth and elevation, as shown in Figure 6.3. Surrounding the counting volume is a cuboid representing a volume of the ocean in which targets are to be uniform randomly distributed.

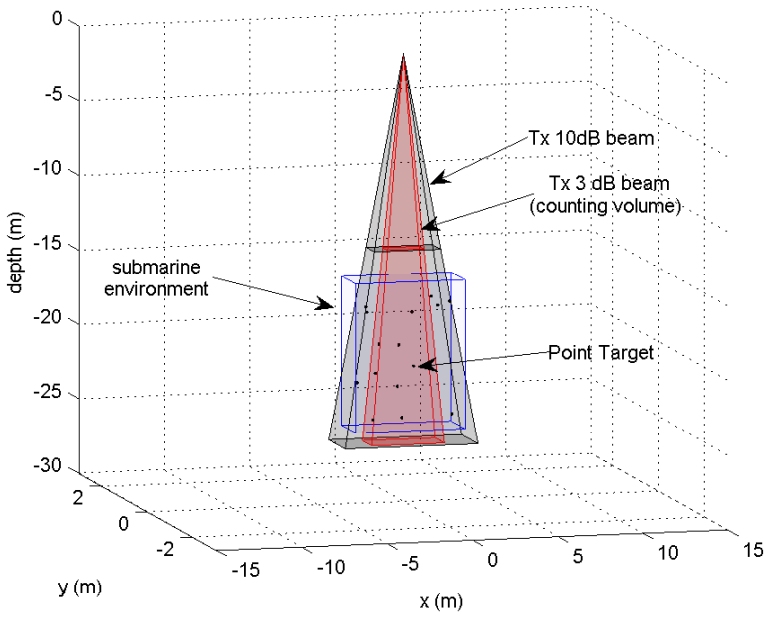

Figure 6.3: The insonified volume of the submarine environment

The simulator, signal processing, and detection parameters used for the development of results are detailed in Tables 6.1, 6.2, and 6.3.

Simulation parameters	
depth of targets/m	15 to 25
Number of targets	15
volume of cuboid (submarine environment)/m^3	40.984
density of targets / number of targets per m^3	0.37
sonar target strength model	on/off
Noise model	on/off
Noise level simulated σ	126.68
k	16384

Table 6.1: Simulation parameters

Signal Processing/digital beamforming parameters	
sonar image range dimensions/m	13 to 26
sonar image azimuth dimensions/°	-7 to 7
Number of beams	32
range sampling interval Δr	0.0168
azimuth sampling interval $\Delta\theta$	0.45
window function	Hamming window

Table 6.2: Signal Processing parameters

Detection parameters	
Probability of false alarm for image $P_{fa_{image}}$	$\leq 10^{-7}$
counting range in azimuth/°	-5.15 to 5.15 (3 dB beam)
counting volume[1]	13.8
Estimate of noise level μ	139.0
Probability of false alarm for cell $P_{fa_{cell}}$	$\leq 6.5 \times 10^{-4}$
T	680

Table 6.3: Detection parameters

6.3 Performance of the counting system

First assessed was the capacity and efficiency of the system and peak finding algorithm to count the number of targets in sonar images formed- evaluate the peak finding algorithm. Fifteen point like unit reflectors (sonar target strength=1) are randomly placed well inside the counting volume and it is assumed there is no noise in the system, as shown in Figure 6.4.

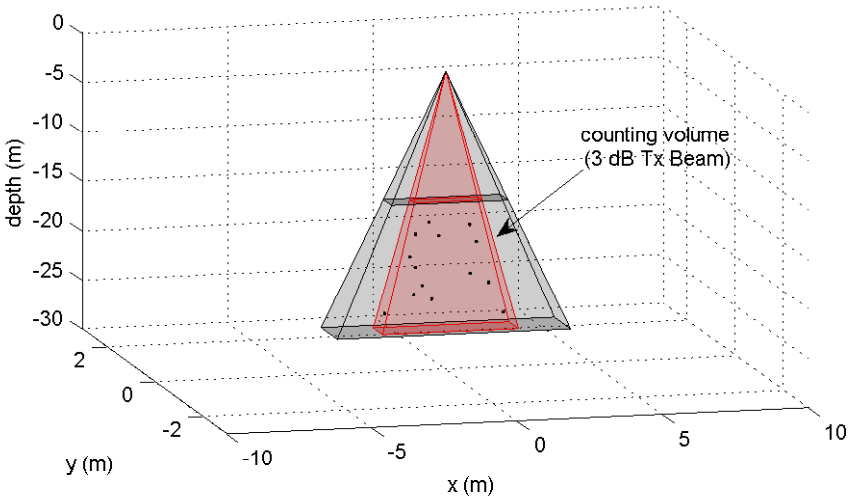

Figure 6.4: Simulation Scenario

For this simplistic evaluation (no noise), the threshold which was 15% [2] of the maximum peak in the image. The number of targets per ping is displayed in Figure 6.5 .

[2] A sonar image depicts the range from 13m to 26 m and counting is limited to the 3 dB beamwidth of the transmitted beam in azimuth. The attenuation factor of the level of the response due to two-way propagation and the directivity function at the extremity of a sonar image is approximately $\frac{1}{4} \times \frac{1}{\sqrt{2}} = 0.17$. Hence, the response due to a target in an image will drop at most by 17% . Further, the worst sidelobe level to mainlobe level ratio in the image is 5%. Therefore, a threshold 15 % of the brightest peak in the image is justified.

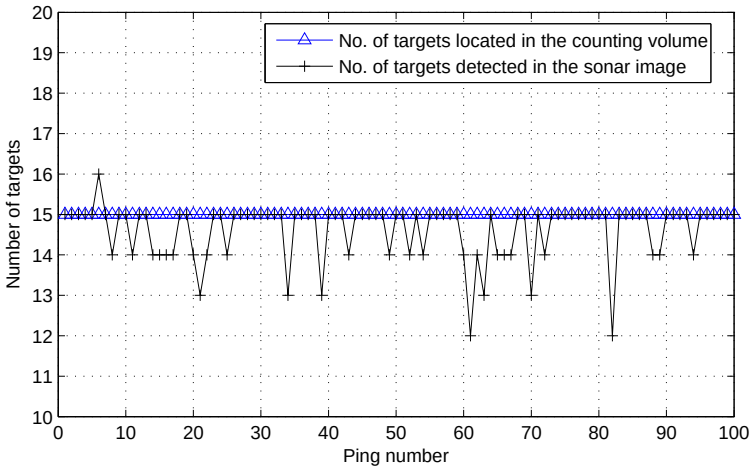

Figure 6.5: Graph showing the number of targets declared present in sonar image.

The error which is defined as the difference in the number of targets generated in the counting volume and the number of targets declared present in the sonar images formed is studied. The errors obtained from processing 100 pings are displayed in Figure 6.6

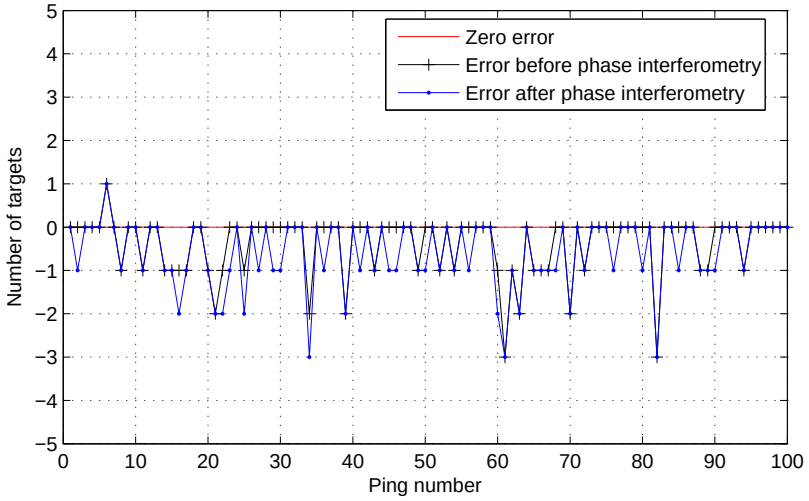

Figure 6.6: Graph indicating the difference between the number of targets generated in the counting volume and the number of targets counted in the sonar image.

6.3.1 Shortcomings

In the shallow regions, the inherently higher target density can lead to there being more than one target within the same resolution cell. Hence, as indicated in Figure 6.6, the system occasionally undercounts.

6.3.2 Effect of target location on the performance of counting system

Next assessed was the efficiency of the counting system when the point-like unit reflectors are randomly distributed in the ocean volume. Some parameters of the simulator were changed: the number of targets was increased to 100; and the volume of the submarine environment was enlarged to encompass the regions insonified by the sidelobes of the transmitted beam, as summarised in Table 6.4.

Number of targets	100
volume of cuboid (submarine environment)/m^3	215.6
density of targets / number of targets per m^3	0.46

Table 6.4: Simulation parameters changed

The scene is depicted in Figure 6.7.

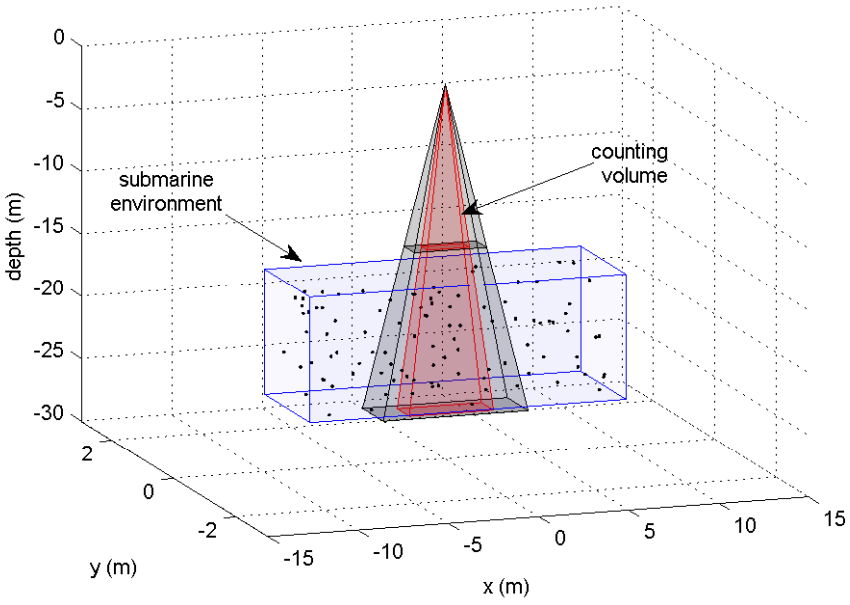

Figure 6.7: The underwater environment

A threshold which is 15% of the maximum peak in the image was used. The results from the imaging and counting system are displayed in Figures 6.8 and 6.9.

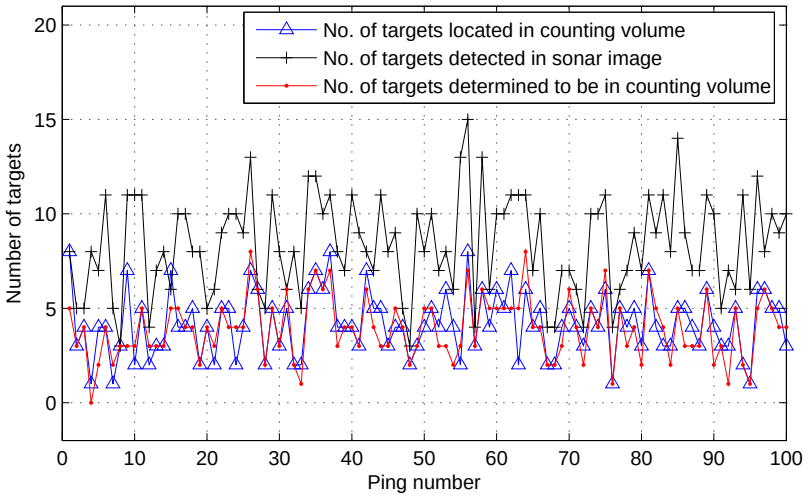

Figure 6.8: The number of targets versus ping number, as a function of target position.

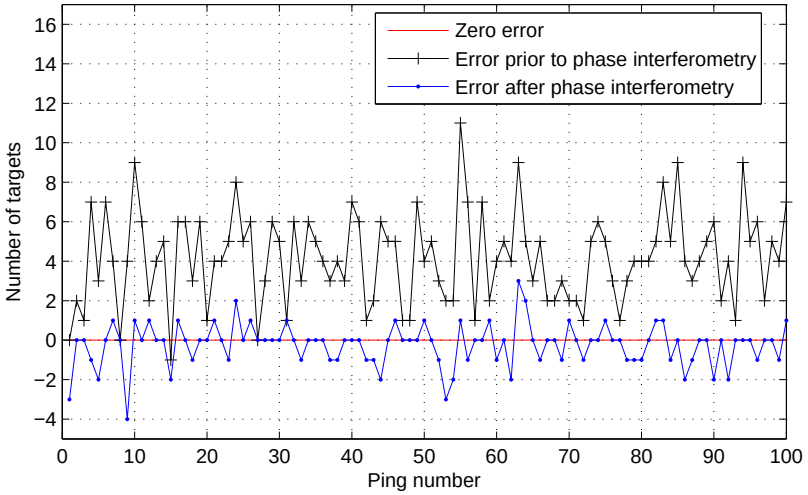

Figure 6.9: The error in the number of targets detected in the counting volume, before and after phase interferometry.

From Figure 6.9, the number of targets detected in the sonar images is an overestimate of the actual number of targets. This is because targets outside the 3-dB beam boundaries, in elevation, of the counting volume also appear in the image. The graph showing the error after phase interferometry indicates that phase interferometry enables those targets to be filtered, resulting in an accurate estimate of the number of targets in the counting volume.

6.3.3 Performance of the counting system versus sonar target strength

A stochastic sonar target strength model is incorporated into the simulator, instead of using unit target reflectivity. The sonar target strength is model has a Rayleigh pdf with an arbitrary mean and limits $[0.25, 1.25]$. There is no noise and the same basic threshold as before. The scene is similar to that displayed in Figure 6.4. The simulation results are displayed in Figure 6.10 and the errors shown in Figure 6.11.

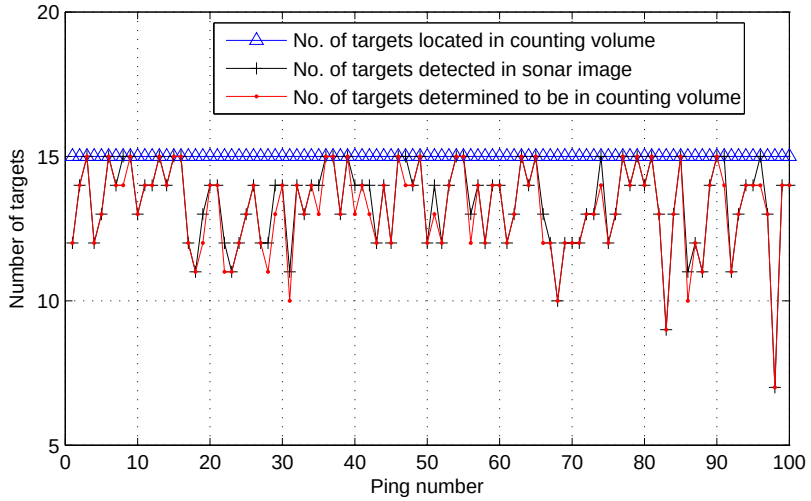

Figure 6.10: Number of targets versus ping number, as a function of stochastic sonar target strength model.

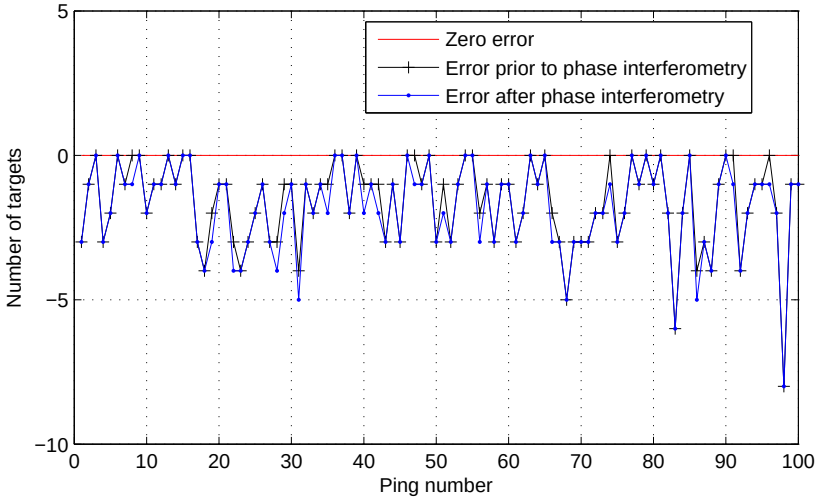

Figure 6.11: Error in the number of targets detected in the counting volume, before and after phase interferometry.

Figure 6.11 indicates that ABACUS undercounts for this simulation scenario. This is expected as the stochastic sonar target strength reduces the level of the echo signal strength. Therefore, lowering the threshold to T= 10 % of the maximum peak of a sonar image would negate the undercount. This is verified in Figure 6.12, similar to Figure 6.6 .

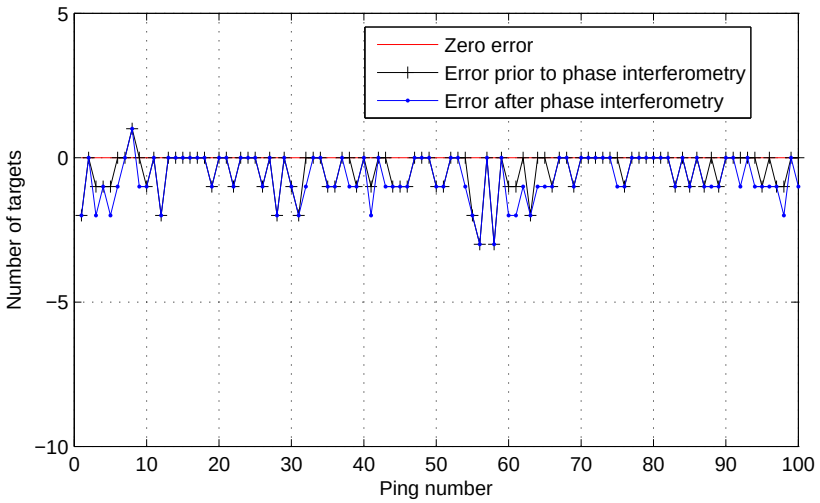

Figure 6.12: Errors after the threshold is lowered.

6.3.4 Performance of the counting system versus noise

To study the effect of noise on the system, the simulator was set for no targets, only band-limited white Gaussian noise. The data was then processed and the noise level μ in the sonar image was estimated. The PDF of the μ estimated in the image cells follows a Rayleigh distribution. This is confirmed in Figure 6.13.

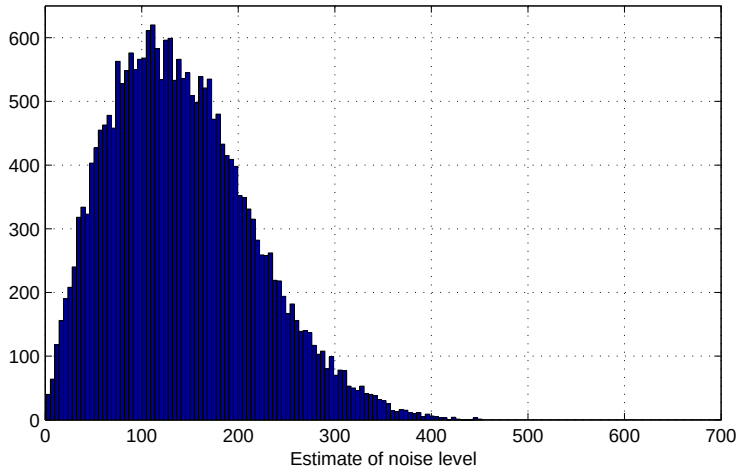

Figure 6.13: PDF of noise level estimated in sonar image

The probability of false alarm was set to $P_{fa} \leq 10^{-7}$ so that it would not be exceeded. From the parameters in Tables 6.1 and 6.2, the number of azimuth sampling intervals $= \frac{5.15--5.15}{\Delta\theta} \approx 23$. Number of range sampling intervals $= \frac{26-13}{\Delta r} \approx 774$. Therefore, the number of hypotheses (image cells) to be tested were $\approx 23 \times 774 = 17802$. Using Equation 5.4, the probability of false alarm for a cell of the image was $P_{fa_{cell}} = 9.05 \times 10^{-4}$.

The mean μ from a sonar image was estimated to be 139.8. The mean noise level was assumed to be constant over pings. The threshold was estimated according to Equation 5.9 to be ≈ 670. The parameters calculated for the detection of targets are summarised in Table 6.5 and the results from processing 100 pings are displayed in Figure 6.14.

Detection parameters	
Probability of false alarm for image $P_{fa_{image}}$	$\leq 10^{-7}$
counting range in azimuth/°	-5.15 to 5.15 (3 dB beam)
Estimate of noise level μ	139.8
Probability of false alarm for cell $P_{fa_{cell}}$	$\leq 9.05 \times 10^{-4}$
Threshold T	670

Table 6.5: Detection parameters

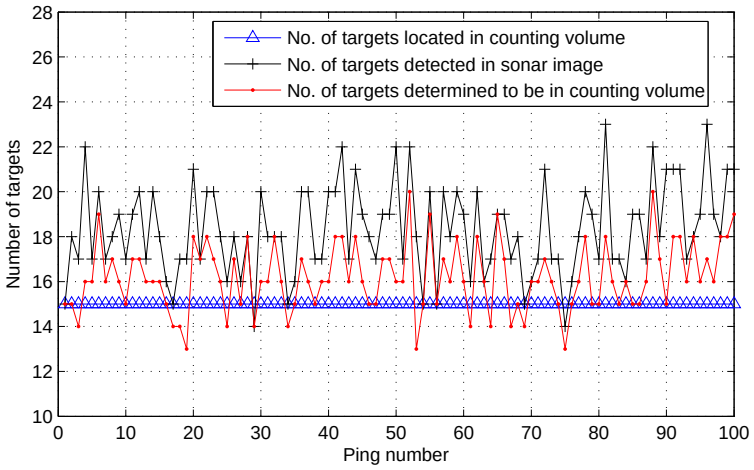

Figure 6.14: Number of targets versus ping number, as a function of noise.

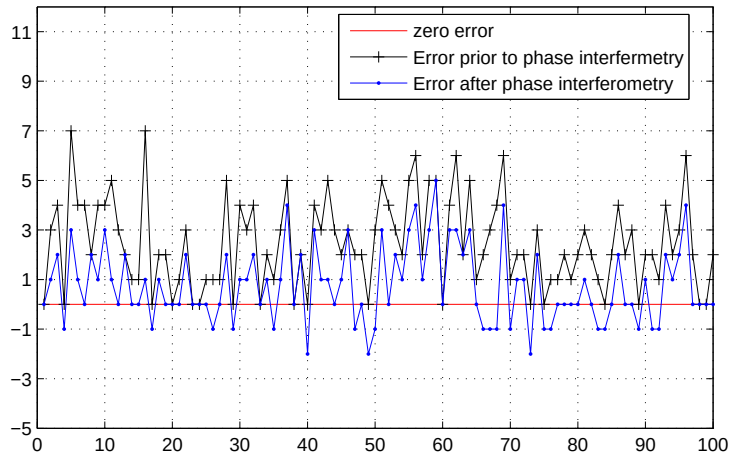

Figure 6.16: Error in the number of targets detected in counting volume, before and after phase interferometry (T=700)

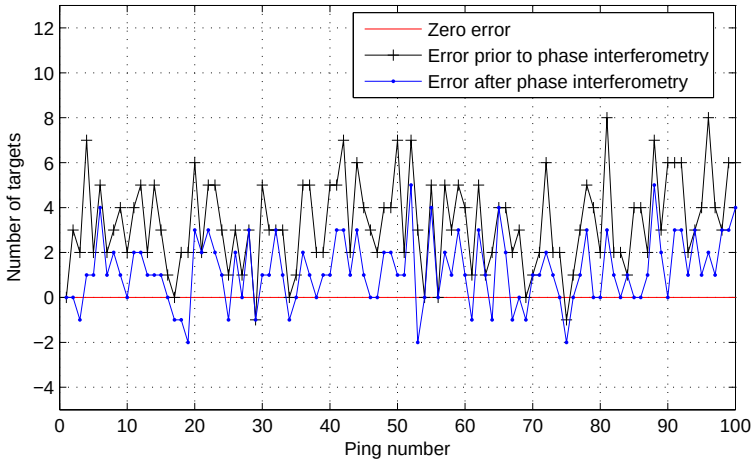

Figure 6.15: Error in the number of targets detected in the counting volume, before and after phase interferometry.

Figure 6.15 indicates an overestimate of the actual number of targets. In the shallow regions, the relatively high sidelobes of the response, to which noise is added, exceeds the threshold causing false alarms.

Phase interferometry rejects some of the false alarms.

Increasing the threshold, which was previously just clearing the minimum threshold calculated, should negate the over-estimation, and this is verified in Figure 6.16.

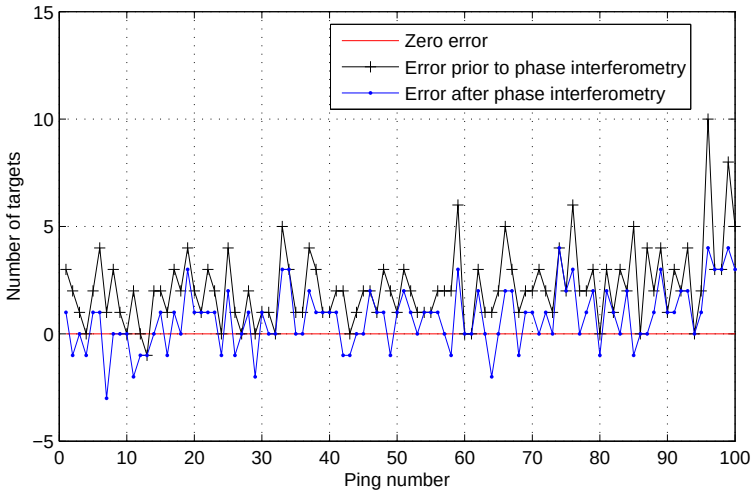

Figure 6.17: Error in the number of targets detected in counting volume, before and after phase interferometry (T=730)

6.3.5 Performance of ABACUS versus all simulation variables

The performance of the detection and counting system was evaluated for a simulated pelagic survey. All the variables (position, sonar target strength and noise) were as in Tables 6.6 and the scenario is depicted in Figure 6.7.

Simulation parameters	
depth of targets/m	15 to 25
Number of targets	100
volume of cuboid (submarine environment)/m^3	215.6
density of targets / number of targets per m^3	0.46
sonar target strength model	on
Noise model	on
Noise level simulated σ	126.68
k	16384

(a) Pelagic survey simulation parameters

Detection parameters	
Probability of false alarm for image $P_{fa_{image}}$	$\leq 10^{-7}$
counting range in azimuth/°	-5.15 to 5.15 (3 dB beam)
counting volume^3	13.8
Estimate of noise level μ	140.16
Probability of false alarm for cell $P_{fa_{cell}}$	$\leq 9.05 \times 10^{-4}$
T	670

(b) Detection parameters for pelagic survey simulation

Table 6.6: Simulation and detection parameters

The results for the number of detected and counted targets are displayed in Figure 6.18 and the errors are shown in Figures 6.19, 6.20 and 6.21.

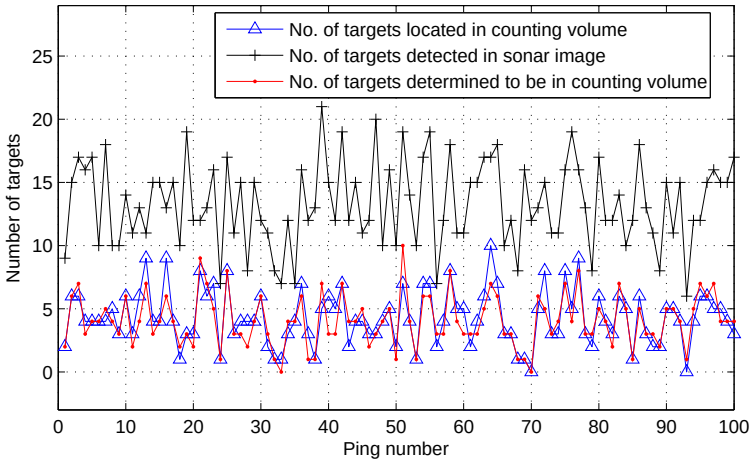

Figure 6.18: The number of detected and counted targets versus the number of pings (T=670)

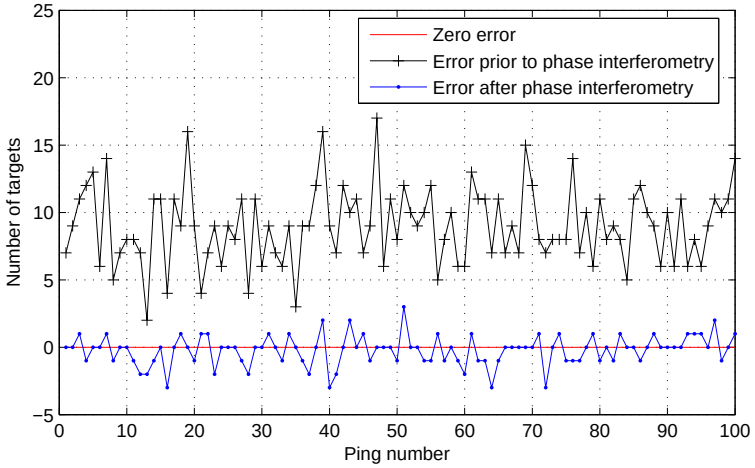

Figure 6.19: The error in the number of targets detected in the counting volume, before and after phase interferometry (T=670)

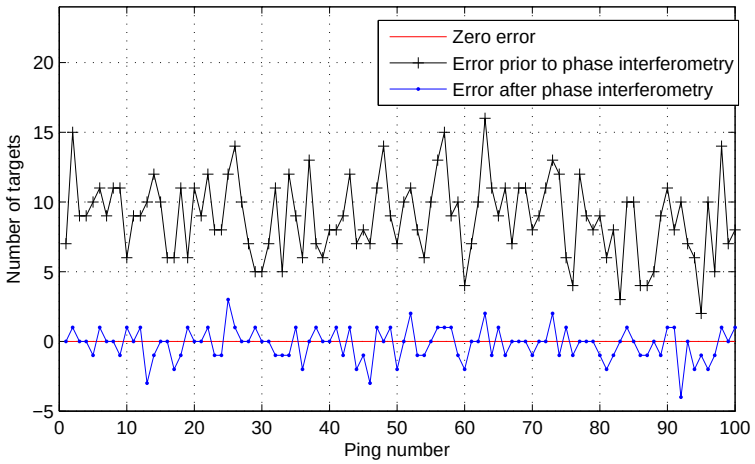

Figure 6.20: The error in the number of targets detected in the counting volume, before and after phase interferometry (T=700)

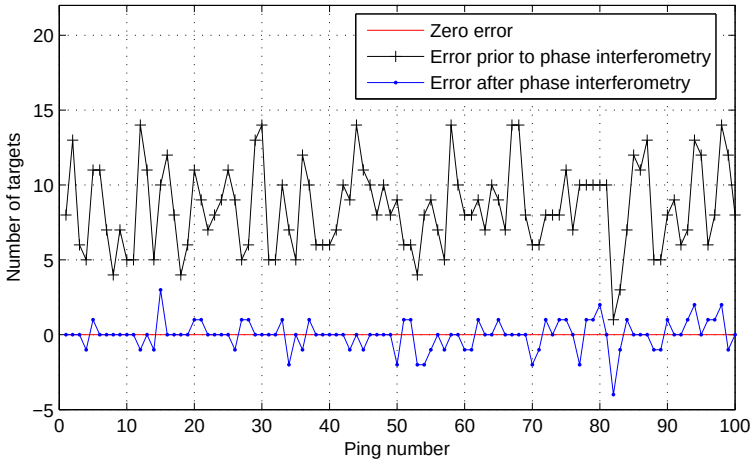

Figure 6.21: The error in the number of targets detected in the counting volume, before and after phase interferometry (T=730)

From the graphs displaying the errors for the various thresholds, the number of detected and counted targets follow the number of targets located in the counting volume, with no apparent bias. However, the system might be sensitive to the threshold.

6.3.6 Sensitivity of system to threshold

To explore the counting system's performance versus threshold, the average error was calculated for different thresholds. A graph plotting the average error against threshold is displayed in Figure 6.22.

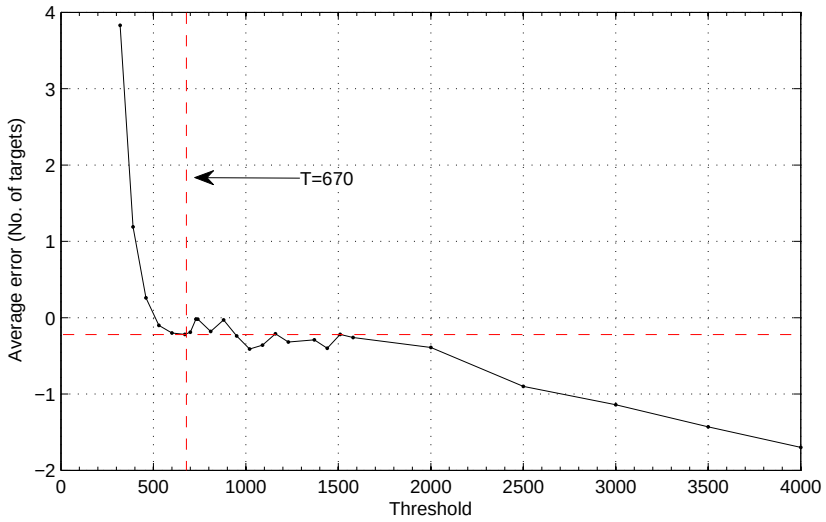

Figure 6.22: Average error of the system versus threshold

6.22indicates that there is a plateau of constant, near zero average errors for thresholds between 600 and 2000. Therefore, a slightly higher threshold than the one calculated (T=670) should improve the performance.

6.4 Estimate of target counts from real sonar data

Real ABACUS data were processed to confirm the simulator results. The noise statistics for the real data set were obtained, by a visual analysis of sonar images, from regions in the images where no targets were deemed to be present [4]. The noise probability density function is displayed in Figure 6.23.

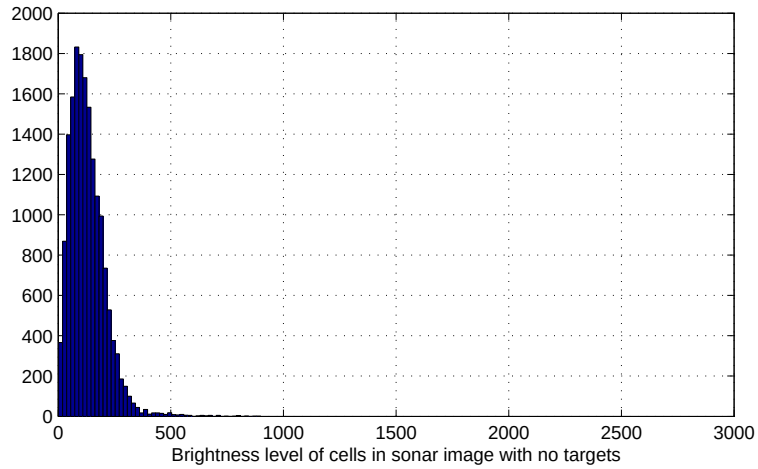

Figure 6.23: PDF of the estimate of the noise in a sonar image with no targets present.

It is observed that the distribution is Rayleigh, which agrees with theory. Therefore, the threshold was calculated in the same way as for the simulator. For this particular data set, the threshold was determined to be $T \backsimeq 610$. The estimate of the number of squid targets versus ping number is displayed in Figure 6.24.

[4] We point out that for the particular real data set processed, no recordings were taken with the transmitter off.

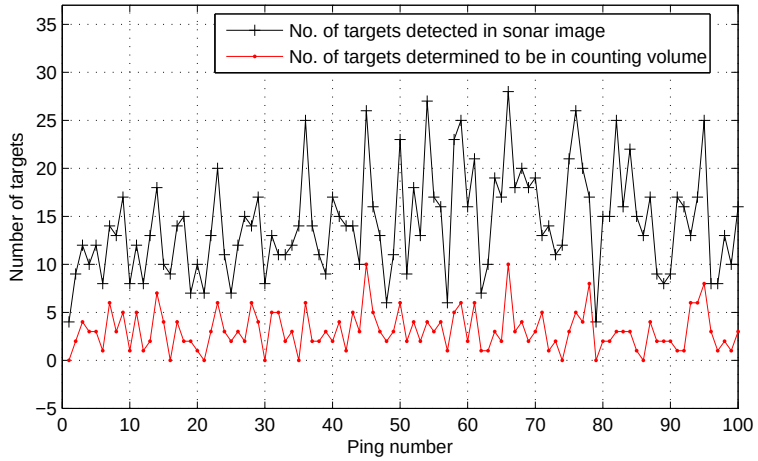

Figure 6.24: The number of targets versus ping number (T=610)

The estimate of the count for real data is a non stationary process.

6.5 Density of squid targets

One of the potential uses of ABACUS is the estimation of the sonar target strength of in-situ squid. ABACUS provides estimates of squid counts per unit volume (density), which can be used in conjunction with an echo-integrator to achieve the aim. Figure 6.25 displays the average density as a function of time, confirming that the ABACUS and the developed counting system can indeed be used to achieve the aim.

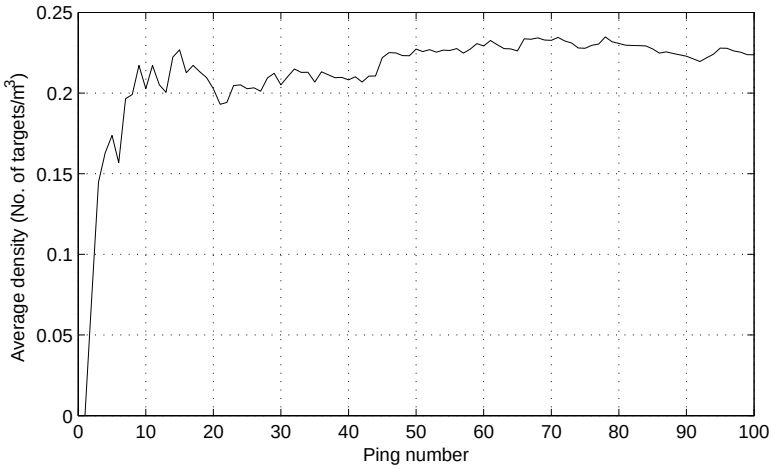

Figure 6.25: The estimated average density of targets versus ping number.

Chapter 7

Conclusion and Future Work

7.1 Conclusion

A mathematical model has been developed for the operation of ABACUS. The model is limited by simplifying assumptions regarding noise, sound attenuation, and sonar target strength models. The computational model was used to develop a simulator for ABACUS in MATLAB. The simulator provided synthetic data for various operating scenarios of the sonar. The effect ABACUS'S antenna arrangement has on the directivity functions and the performance of the system was studied. Most of the variants ABACUS's antennas relative to a linear array, did not yield measurable benefits. However, changing the orientation of the elements at the extremities of the transmitter improves the mainlobe to sidelobe ratio of the imaging resolution cell in elevation.

Further, the relevant signal processing needed to estimate the location of targets was studied. The range was estimated by pulse compression, using a matched filter. The azimuth location was obtained using beamforming. Simplifying assumptions about the propagation of sound in the submarine environment were made to simplify the signal processing. The received beam was steered in software to scan a volume of the scene, thus obtaining 2D images of the azimuth-range plane of the underwater environment. ABACUS is capable of high resolution imaging of targets. Sidelobe control was applied in range, and spatial windowing in azimuth, to reduce sidelobes and consequently to enhance the capacity of the system to image weak targets in proximity of strong ones. This improvement was made at the expense of resolution. The formation of ghost images in ABACUS was studied and their effect on the counting system is minimal. Phase interferometry was used in conjunction with the geometry of ABACUS to estimate the elevation angle of arrival of targets. Phase wrapping is not an issue, and it was assumed that there is only one target in an azimuth-range cell of the sonar image formed.

Some aspects of detection theory were reviewed to estimate the number of targets in the sonar images. The sonar images were contaminated by noise. The response of the targets in a sonar image is a sinc type function with more-or-less bright secondary maxima. Moreover, the brightness of the peaks varied as a function of range, bearing, and sonar target strength. The sonar target strength also varies. Therefore, a statistical hypothesis was formulated to optimise a threshold to discriminate targets from sidelobes and noise in the sonar images. A threshold was calculated by setting the probability of false alarm not to be exceeded for the images. Assuming that the noise level does not vary over time, the number of peaks above the threshold was estimated by an algorithm based on the zero crossing of the first derivative of the peaks in the image. Further, the parameters of the targets and the geometry of ABACUS were considered to solve a system of equations to resolve the locations of the targets in 3-D.

The performance of the imaging and counting system was then evaluated. The counting algorithm was quite efficient in counting the number of peaks in the images. However, there were some undercounts in regions of high target density. The performance of the imaging and counting system was then evaluated with respect to each of the following variables: target position, noise and sonar target strength. With position as the only variable, the system overcounted the number of targets in the counting volume prior to phase interferometry. After phase interferometry, the mean error of the number of targets estimated to be in the counting volume was close to zero. Therefore, phase interferometry and the target location determination worked well in discarding targets outside the counting volume. With noise as the only variable, the system overcounted, as expected. Evidently, increasing the threshold reduced the average error of the estimated counts. With sonar target strength ,modeled to follow a Rayleigh distribution, as the only variable, the system undercounted and this bias was mitigated by decreasing the threshold. Therefore the system could be sensitive to the chose threshold. All the variables were set in the simulator and the average errors were calculated for various thresholds.There is a range of thresholds that ensure minimum error, indicating that the system was quite robust. The ABACUS is capable of high resolution counting of targets at moderate to high densities. Processing of real data also indicated that ABACUS and the counting system developed can be used to obtain reliable estimates of counts of fish from pelagic surveys.

7.2 Future Work

ABACUS should be upgraded so that all the 32 receiver elements can be sampled, increasing the resolution by a factor of two in interferometric mode.

A more comprehensive model for the sonar target strength of squid should be implemented in the simulator. This should a more optimal threshold and thus more accurate estimate of counts.

For real data, noise should be measured with the transmitter off so as to obtain more accurate results.

The fish densities measured by ABACUS should be validated with independent observations. To do so, a known number of squid could be caged and imaged and counted by the ABACUS.

Appendix A

Appendix A

The layout of the imaging and counting system developed in the MATLAB package is given below.

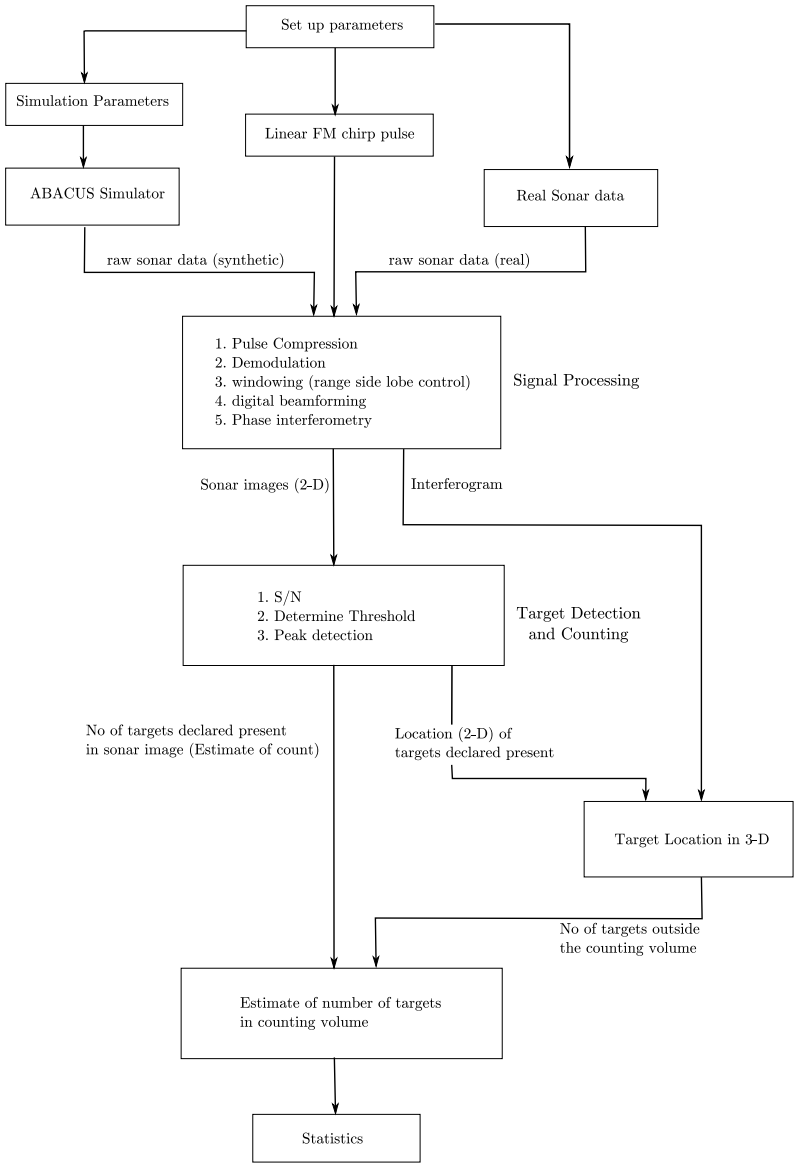

ABACUS System Block Diagram

Figure A.1: ABACUS System Block Diagram

Appendix B

In Appendix B, images obtained from processing simulated data from a number of pings with parameters Tables 6.6 and with threshold $T = 810$ are shown.

Ping 1.

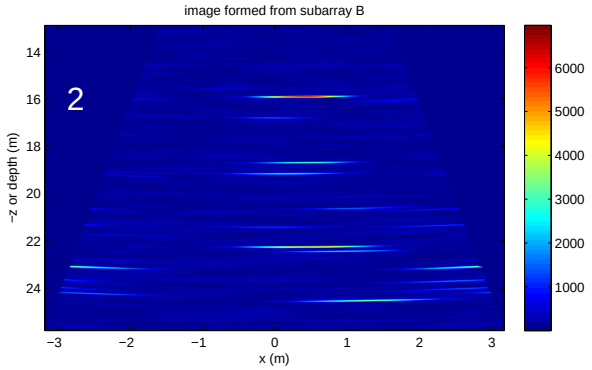

(a) Fan beam image of horizontal plane

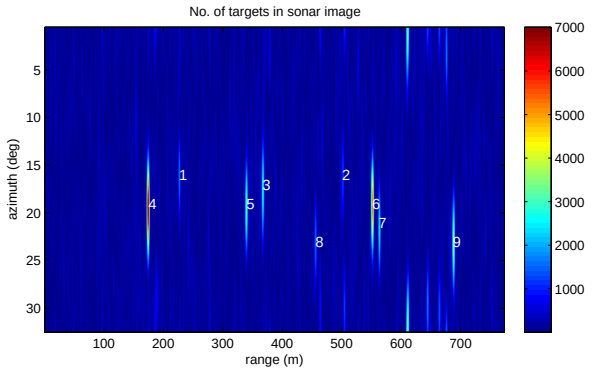

(b) No. of targets are counted in the sonar image = 9

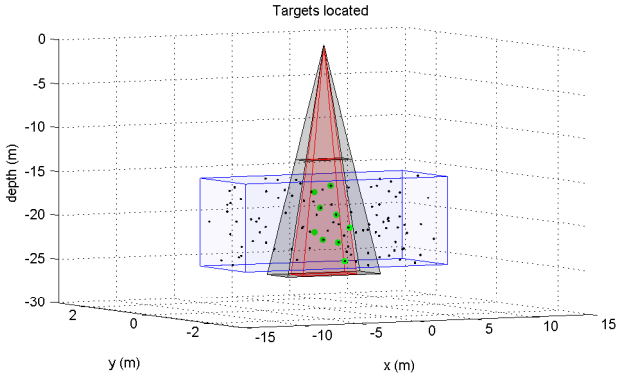

(c) Phase interferometry methods locate the targets detected as shown by dots in green. Number of targets in counting volume = 2.

Figure A.2: Results from ping 1

Ping 2

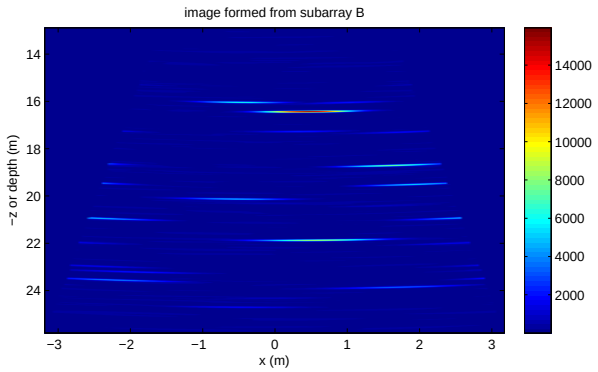

(a) Fan beam image of horizontal plane

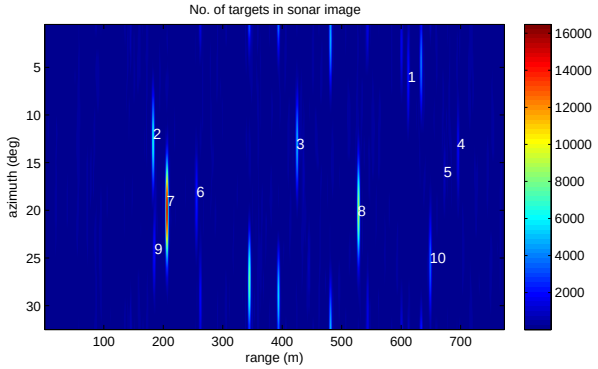

(b) No. of targets are counted in the sonar image = 10

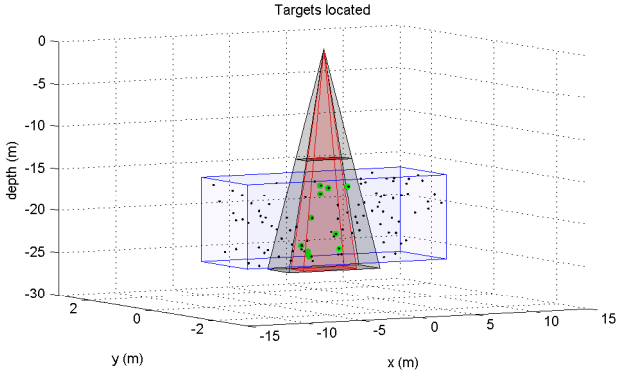

(c) Phase interferometry methods locate the targets detected as shown by dots in green. Number of targets in counting volume = 4.

Figure A.3: Results from ping 2

Ping 3

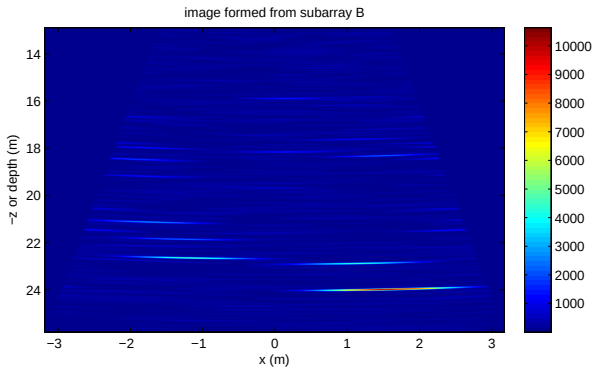

(a) Fan beam image of horizontal plane

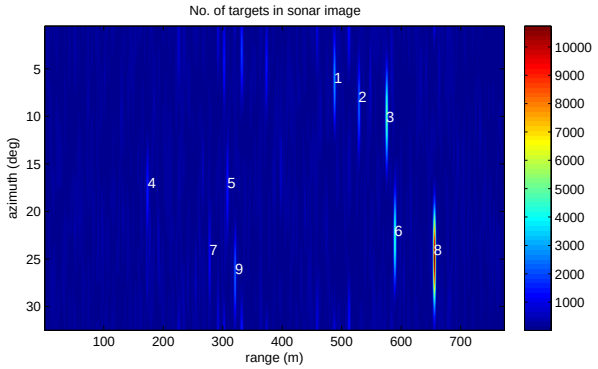

(b) No. of targets are counted in the sonar image = 9

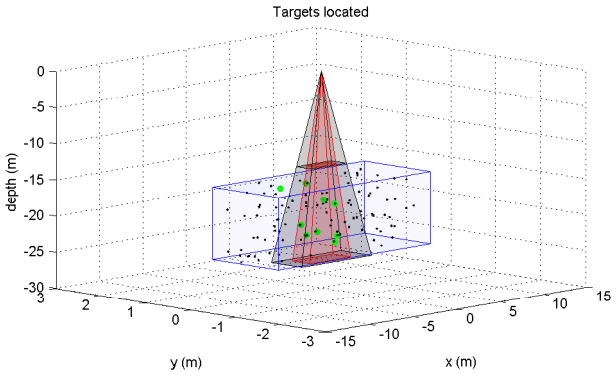

(c) Phase interferometry methods locate the targets detected as shown by dots in green. Number of targets in counting volume = 4.

Figure A.4: Results from ping 3

Ping 4

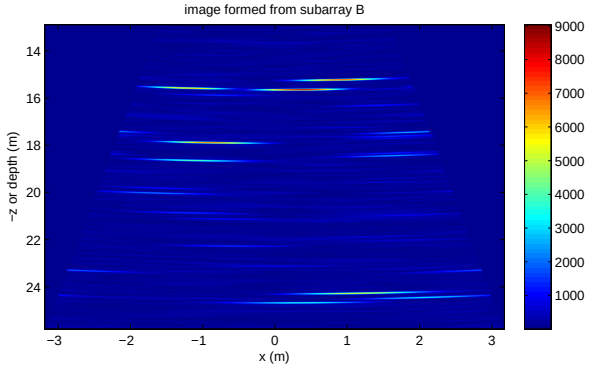

(a) Fan beam image of horizontal plane

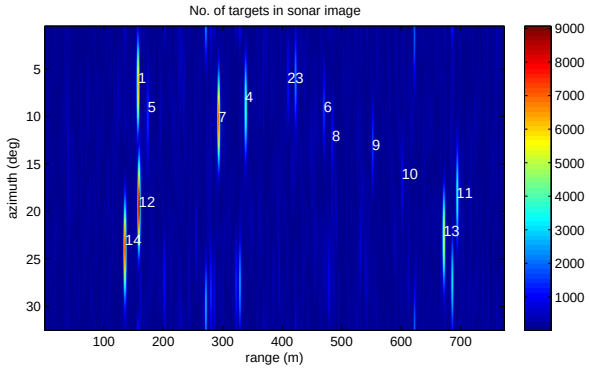

(b) No. of targets are counted in the sonar image = 14

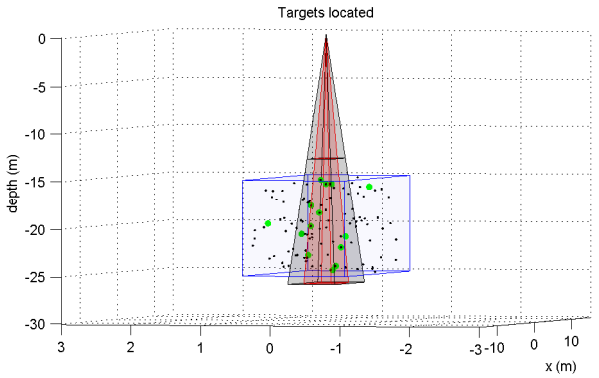

(c) Phase interferometry methods locate the targets detected as shown by dots in green. Number of targets in counting volume = 5.

Figure A.5: Results from ping 4

Ping 5

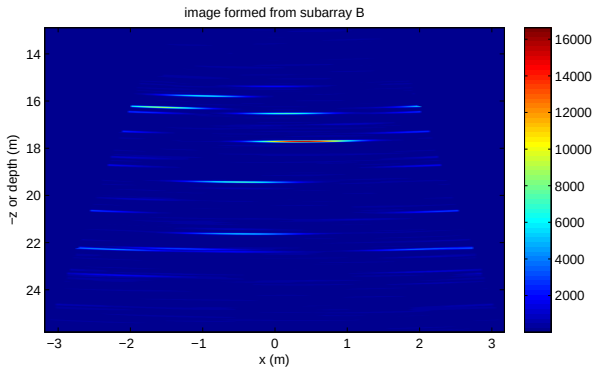

(a) Fan beam image of horizontal plane

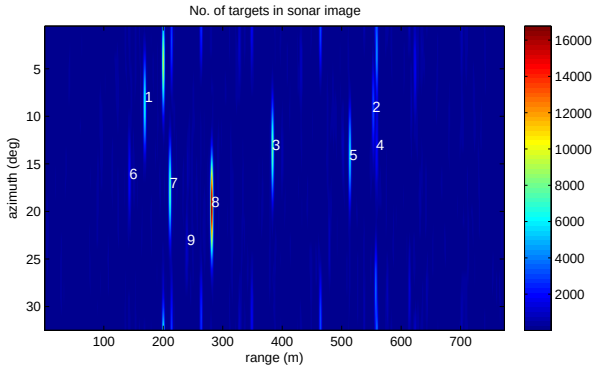

(b) No. of targets are counted in the sonar image = 9

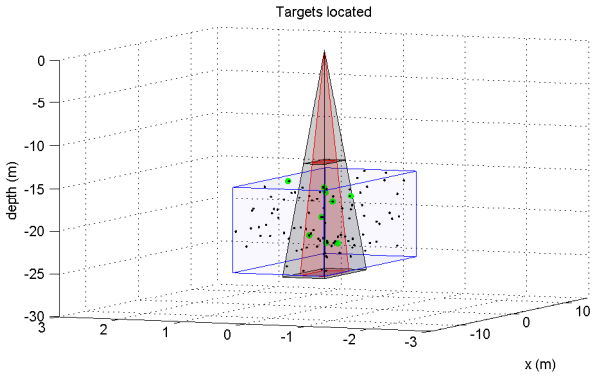

(c) Phase interferometry methods locate the targets detected as shown by dots in green. Number of targets in counting volume = 5.

Figure A.6: Results from ping 5

Appendix C

In Appendix C, images from processing a few pings of real ABACUS data out of the total 100 pings are displayed.

Ping 31.

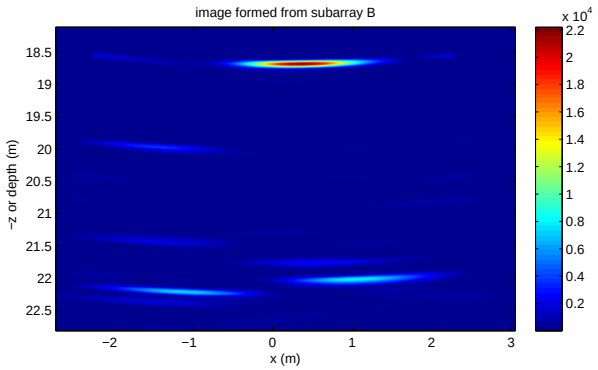

(a) Fan beam image of horizontal plane

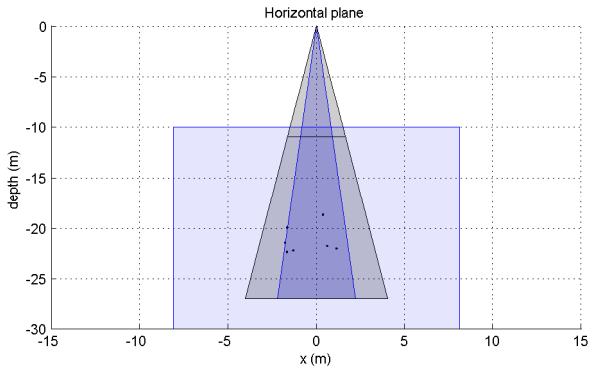

(b) Targets located in the horizontal plane of counting volume

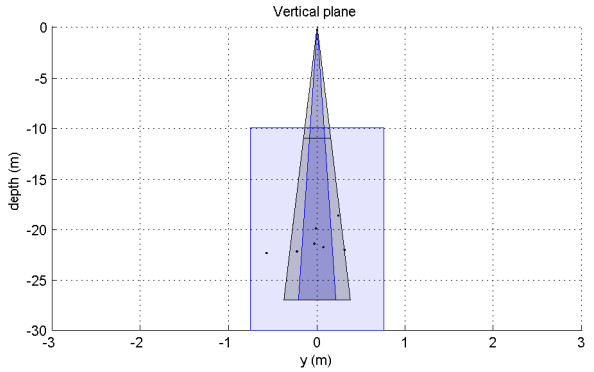

(c) Targets located in the horizontal plane of counting volume

Figure A.7: Results from ping 31

Ping 45

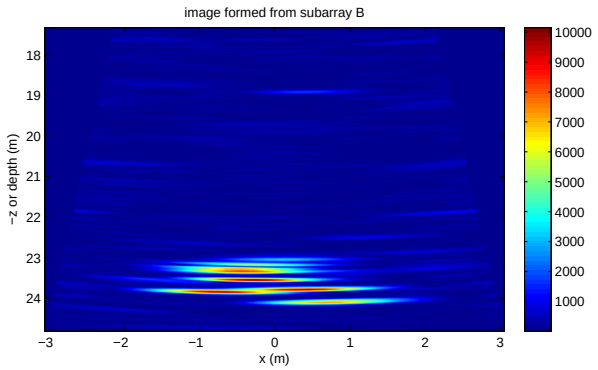

(a) Fan beam image of horizontal plane

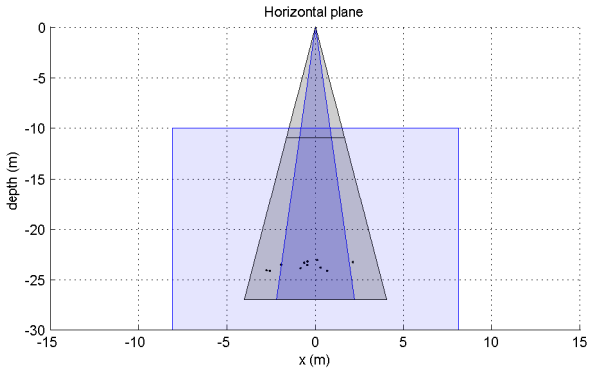

(b) Targets located in the horizontal plane of counting volume

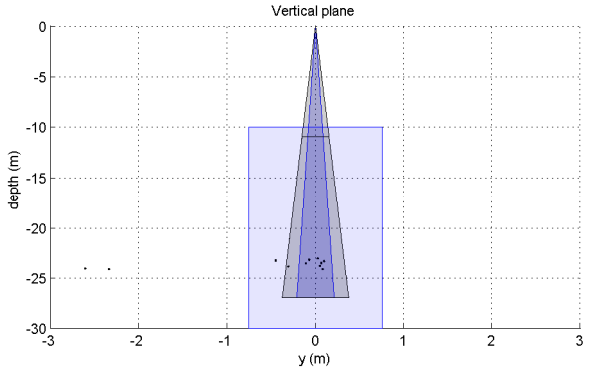

(c) Targets located in the horizontal plane of counting volume

Figure A.8: Results from ping 45

Ping 55

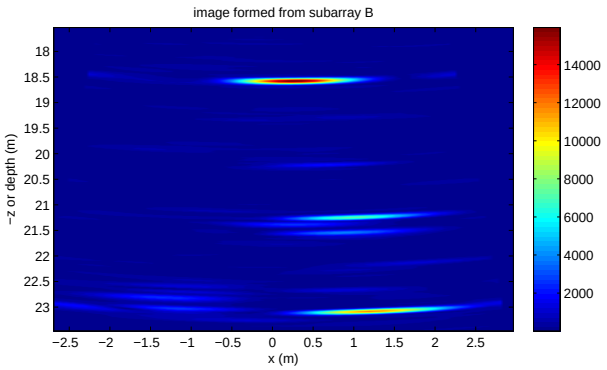

(a) Fan beam image of horizontal plane

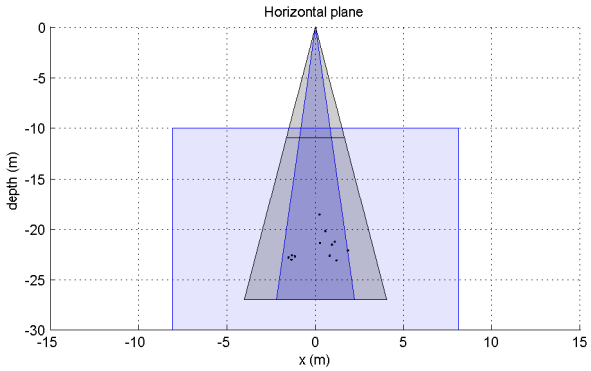

(b) Targets located in the horizontal plane of counting volume

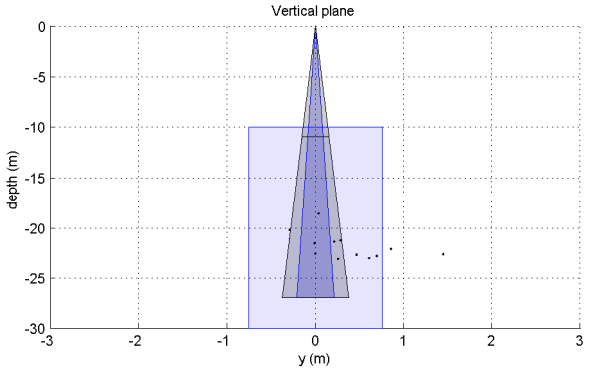

(c) Targets located in the horizontal plane of counting volume

Figure A.9: Results from ping 55

Ping 81

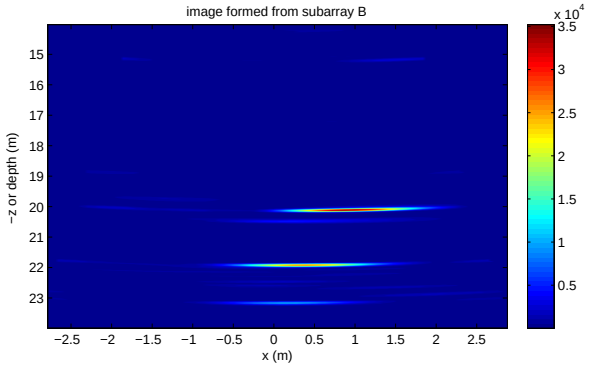

(a) Fan beam image of horizontal plane

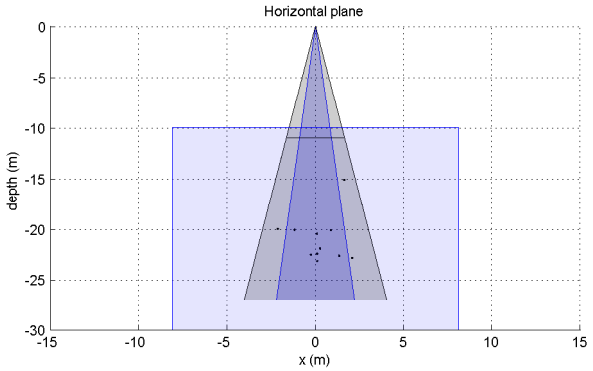

(b) Targets located in the horizontal plane of counting volume

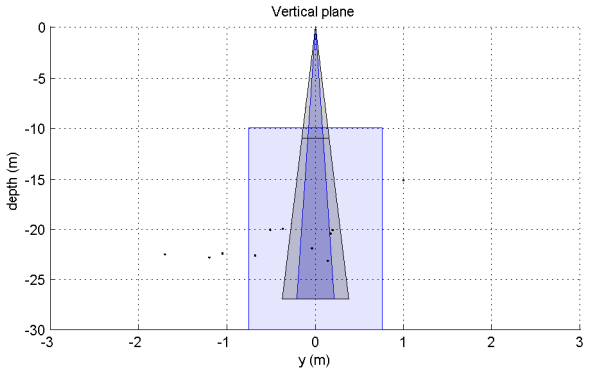

(c) Targets located in the horizontal plane of counting volume

Figure A.10: Results from ping 81

Bibliography

[1] Principles of sonar beamforming. In *IMA conference on parallel computing St Catherine's College, Oxford*, 13th July 1998.

[2] Multibeam sonar theory of operation. Technical report, L3 communications SeaBeam Instruments, 1999.

[3] Nyoman Arnaya and Noritatsu Sano. Studies on acoustic target strength of squid vi. simulation of squid target strength by prolate spheroidal model. *Bull. Fac. Fish. Hokkaido Univ.*, 41(1):32–42, 1990.

[4] Richard E. Blahut. *Theory of Remote Image Formation*. Cambridge University Press.

[5] Richard E. Blahut. Lecture notes in radar/sonar. Technical report, Institute for Mathematics and Its applications, University of Minnesota, 1990.

[6] Lake Kelk Calibration Centre. *ACOUSTIC TRANSDUCER CALIBRATION*. Neptune Sonar Limited.

[7] T.E. Curtis and R.J. Ward. Digital beam forming for sonar systems. In *IEE proceedings. Part P, Radar and signal processing*, 1980.

[8] Philip Denbigh, Quinton Smith, and Ian Hampton. Determination of fish number density by a statistical analysis of backscattered sound. *Acoustical Society of America*, 90:457–469, 1991.

[9] David N. MacLennan E. John Simmonds. *Fisheries Acoustics: Theory and Practice*. Blackwell Publishing, 2005.

[10] Etienne Frederick Eccles. Super-resolution phased array sonar imaging. Master's thesis, University of Cape Town, November 2005.

[11] Andrzej Elminowicz. Efficient wideband beamformer in the frequency domain for a linear array sonar. *Molecular and Quantum Acoustics*, 23, 2002.

[12] Peter K. Eriksen François Gerlotto, Stratis Georgakarakos. The application of multi-beam sonar technology for quantitative estimates of fish density in shallow water acoustic surveys. *Aquatic Living Resources*, 13:385–393, 2000.

[13] Norman A. Cochrane Gary D. Melvin and Yanchao Li. Extraction and comparison of acoustic backscatter from a calibrated multi- and single-beam sonar. *ICES Journal of Marine Science*, 60:669–677, 2003.

[14] W. Hunting Howell. Development of multi-beam sonar as a fisheries tool for stock assessment and essential fish habitat identification of groundfish in western gulf of maine. Technical report, Department of Zoology, University of New Hampshire, 2006.

[15] Simon Kingsley and Shaun Quegan. *Understanding Radar Systems.* SciTech Publishing, Inc, 1999.

[16] Hamid Krim and Mats Viberg. Two decades of array signal processing research. In *IEEE Signal Processing Magazine, pages 67-94*, 1996.

[17] E.Krömer L. Bernière, U. Hölscher-Höbing. Advanced sonar scene simulation tool for buried minehunting applications. Sebaldsbrücker Heerstraße 235, D-28305 Bremen. STN ATLAS Electonik GmbH. berniere@stn-atlas.de.

[18] François Le Chevalier. *Principles of Radar and Sonar Signal Processing.* Artech House, 2002.

[19] Ali Pezeshki Louis Scharf, Henry Cox Barry Van Veen. In collaboration with Olivier Besson, and Magnus Lundberg. Eigenvalue beamforming using a multi-rank mvdr beamformer and subspace selection (matched subspace & matched direction beamforming). Technical report, Colorado State University, Princeton University, and University of Wisconsin-Madison, 2006.

[20] Rick Lyons. How to interpolate in the time-domain by zero-padding in the frequency domain, 1999.

[21] Brian Maranda. Efficient digital beamforming in the frequency domain. *Acoustical Society of America*, 86 (5), 1989.

[22] Ferdinand Ng. The image formation and calibaration of the abacus sonar system. Master's thesis, University of Cape Town, 2005.

[23] Professor Emeritus Tom O'Haver.

[24] Professor Emeritus Tom O'Haver. Peak finding and measurement. Technical report, Department of Chemistry and Biochemistry The University of Maryland at College Park, 2009.

[25] Janet Coetzee Ole Arve Misund. Recording fish schools by multi-beam sonar: potential for validating and supplementing echo integration recordings of schooling fish. *Fisheries Research*, 47:149–159, 2000.

[26] Alan V. Oppenheim and W. Schafer. *Discrete - Time Signal Processing.* Prentice Hall of India, 1998.

[27] Paul Padley. Diffraction from a rectangular aperture. *Connexions Web site. http://cnx.org/content/m13096/1.2/, Nov 14, 2005.*

[28] Yoann PAICHARD. *Camera hyperfréquence pour la mesure et l'analyse de la SER des cibles scintillantes.* PhD thesis, Université Paris-sud XI Faculté des Sciences d'Orsay, 2007.

[29] Mark A. Richards. *Fundamentals of Radar Signal Processing.* McGraw-Hill Book Company, 2005.

[30] Mark A. Richards. A beginner's guide to interferometric sar concepts and signal processing. *IEEE A&E SYSTEMS MAGAZINE*, 22, No.9, 2007.

[31] Are Rønhovde. High resolution beamforming of simrad em3000 bathymetric multibeam sonar data. Master's thesis, UNIVERSITY OF OSLO Department of Informatics, 1999.

[32] Clarence S.Clay and Herman Medwin. *ACOUSTICAL OCEANOGRAPHY: PRINCIPLES AND APPLICATIONS.* Wiley-Interscience, 1977.

[33] J.O. Smith. *Mathematics of the Discrete Fourier Transform (DFT).* accessed (7/01/2009). online book.

[34] M.A Soule and I.Hampton. Advanced beamformer for acoustic counting of underwater scatterers (abacus) - potential for in-situ strength estimation. Fisheries Resource Surveys cc, Cape Town, South Africa, 2002.

[35] Ferrel G. Stremler. *Introduction to Communication Systems.* Addison - Wesley, 1990.

[36] Murat Torlak. Spatial array processing. Technical report, Telecommunications and Information Systems Engineering The University of Texas at Austin.

[37] D. Kraus U. Hölscher-Höbing, E. Krömer. Sonar simulation program for minehunting application. Technical report, STN ATLAS Elektronik GmbH.

[38] Robert J. Urick. *Principles of underwater sound / 3rd edition.* McGraw-Hill Book Company, 1983.

[39] A.J. Wilkinson. Signal processing and system design considerations for a broadband imaging sonar. Technical report, Department of Electrical Engineering Univeristy of Cape Town, 2007.

[40] Andrew Wilkinson. Radar / sonar notes. Technical report, University of Cape Town, 2008.

[41] Andrew John Wilkinson. *Techniques for 3-D Surface Reconstruction using Synthetic Aperture Radar Interferometry.* PhD thesis, University College London, 1997.

[42] Shi-Chang Wooh and Yijun Shi. A simulation study of the beam steering characteristics for linear phased arrays. *Nondestructive Evaluation*, 19(No. 2), 1999.

[43] Shi-Chang Wooh and Yijun Shi. Three-dimensional beam directivity of phase-steered ultrasound. *Acoustical Society of America*, 105(6):3275–3282, 1999.